Dynamic characterization of micro-particle systems

Thesis by

Wei-Hsun Lin

In Partial Fulfillment of the Requirements for the degree

of

Doctor of Philosophy

CALIFORNIA INSTITUTE OF TECHNOLOGY

Pasadena, California

2016

(Defended June 22, 2015)

Acknowledgements

I would first like to acknowledge and thank my advisor and mentor, Professor Chiara Daraio. I appreciate all of her contributions of time, ideas, and funding to make my Ph.D. a truly positive experience. Her passion and enthusiasm for and immense knowledge of science and research provided an excellent example of a successful scientist and professor. I also appreciate her extremely motivating attitude during my thesis work. Without her enormous amount of support for and patience regarding this project, I would not have been able to complete it.

Besides my advisor, I would also like to thank the other members of my thesis committee: Professor Michael Cross, Professor Melany Hunt, and Professor Kenneth Libbrecht.

I also thank my family for the unconditional support and understanding that they provided me.

I additionally need to express my appreciation to the people who have contributed to this work. My sincere thanks go to the following individuals: Gladia Hotan, a Caltech undergraduate, for her contribution to most of the dry particle experiments and the development of the experimental protocol; Jinwoong Cha, an ETH Ph.D. student, for his work on modeling and the numerical simulation of the colloidal experiments; Dr. Ivo Buttinoni, Professor Isa Lucio, and Dr. Stephane Job, who are our collaborators in the project on micro-colloidal system; Dr. Alexandre Charles, for his help in the optimization of the numerical fitting; Professor Nesterenko and Professor Molinari, for their helpful discussions; Melissa Melendes, for her help in the fabrication of the micro-structure; and Petros Arakelian, Joe Haggerty, and Jean-Claude Tomasina, who all contributed to a large part of the experimental setup's construction.

I would also like to thank the entire Daraio group, which is made up of the most friendly, helpful, and supportive people I have ever known. And to my roommates in Zurich, Luca Bonanomi and Marc Serra Garcia: your heartwarming friendship and understanding made my life in Europe an enjoyable experience

Finally, I would like to express special thanks to the following funding agencies: AFOSR, ARO MURI, Sloan Fellowship, ONR YIP, and NSF MRSEC.

Abstract

Ordered granular systems have been a subject of active research for decades, due to their rich dynamic response and nonlinearity. For example, their extraordinary wave propagation properties, shock absorption ability, and tunability are of interest for different scientific communities that range from condensed matter physics to applied mathematics to engineering. Thanks to their unique nonlinear properties, ordered granular systems have been suggested for several applications, such as solitary wave focusing, acoustic signals manipulation, and vibration absorption. Most of the fundamental research performed on ordered granular systems has focused on macro-scale examples. However, most engineering applications require these systems to operate at much smaller scales (for example, to affect acoustic signals in the ultrasound regime within acoustic imaging applications). Very little is known about the response of micro-scale granular systems, primarily because of the difficulties in realizing reliable and quantitative experiments. These experimental difficulties originate from the discrete nature of granular materials and their highly nonlinear inter-particle contact forces. The discreteness and accompanying micro-scale sizes require efficient means to assemble the particles precisely, to excite them, and to measure their dynamic response. The high nonlinearity in these systems requires particularly high precision, and imperfections can be extremely important in controlling the dynamic response of the entire system.

In order to characterize micro-scale, ordered, granular systems, it is necessary to understand the fundamental physical mechanisms that govern their response. For example, do the same physical laws that govern the macro-scale granular response apply? Does the Hertzian elastic contact theory hold? What is the role of the particle/substrate interactions? How does stress propagate through micro-scale particle systems and what are the main defects that affect these systems?

In this work, we address these questions by designing an innovative experimental platform that allows us to assemble, excite, and characterize ordered micro-granular systems. This new experimental platform employs a laser system to deliver impulses with controlled momentum and incorporates non-contact measurement apparatuses (including high-speed optical microscopy and laser interferometry) to detect the particles' displacement and velocity. We first built and programed a computer-controlled micro-manipulator that can position and assemble steel micro-particles in

configurations that are desired for testing. We then fabricated microstructures to guide and confine the micro-particle assembly. Next we tested and demonstrated the capability of the laser excitation system to deliver controlled momentums to systems of dry (stainless steel particles of radius 150 μm) and wet (SiO_2 particles of radius 3.69 μm, immersed in fluid) micro-particles, after which we analyzed the stress propagation through these systems.

To describe the fundamental dynamic mechanisms governing the response of dry and wet micro-particle systems, we derived the equations of motion governing the dynamic response of dry and wet particles on a substrate, which we then validated in experiments. We then measured the losses in these systems and characterized the collision and friction between two micro-particles. We next assembled one-dimensional dry chains of micro-particles and investigated the mechanical wave propagation properties as well as the influence of defects in these systems. We also studied wave propagation in two-dimensional colloidal systems immersed in fluid. Finally, we experimentally characterized the wave-attenuation and its relation to the viscosity of the surrounding fluid and performed computer simulations to establish a model that captures the observed response.

The findings of the study offer the first systematic experimental and numerical analysis of wave propagation through ordered systems of micro-particles. The experimental system designed in this work provides the necessary tools for further fundamental studies of wave propagation in both granular and colloidal systems. The findings also offer fundamental insights for the miniaturization of highly nonlinear granular devices.

Table of Contents

List of Figures

List of Tables

Chapter 1

Introduction

1.1. Motivation and significance

Granular materials are collections of discrete, solid particles in ordered or disordered configurations, and are present in many natural and man-made systems. Understanding the fundamental dynamical principles that govern the propagation of stress waves in micro-scale granular systems has implications in many fields of physics and engineering: for example, micro-granular dynamics encompass problems of relevance in powder mixing, acoustics, mining, semiconductor manufacturing, and the pharmaceutical and food industries [1].

Along the broad spectrum of different micro-granular systems, we are especially interested in the characterization of ordered micro-granular systems, and most particularly in micro-granular crystals (which are discrete, ordered arrays of solid micro-particles that are arranged in different lattice geometries). Macroscopic granular crystals, which have been the subject of active research [2-4], have been proposed for use in many engineering applications, such as shock mitigation [5-7], acoustic rectification [8], sound scrambling [9], actuators [10], and acoustic lenses [11, 12]. However, the macro-scale size of the particles tested and modeled in initial studies imposes important limitations to these studies' direct applicability. For example, Donahue et al. [12] demonstrated experimentally the possibility to use properly engineered granular crystals to produce focused, compact pressure pulses in water. Their work directly suggested the use of granular crystals for biomedical imaging and underwater sensing and mapping applications. In these systems, however, the spatial resolution of the propagating pressure pulses, and consequently the size of the focal area, is determined by the size of the particles that compose the granular system. In the experimental setup described by Donahue et al. [9], the particles tested were in the centimeter-scale. This macro-scale dimension limits the spatial resolution of the acoustic pulses traveling through the granular crystals to a few centimeters (and thus necessarily limits the size of the adjacent focal areas to similar dimensions). For acoustic medical imaging or non-destructive evaluation applications, the spatial wavelengths of interest are in the order of a few micrometers. To target these applications it is necessary to miniaturize the granular crystals and to scale the particle size to the micrometer range.

In order to miniaturize granular crystals and explore their functionality at the micro-scale, it is necessary to first understand their underlying physics: Are the assumptions made to model the dynamic response of micro-particles correct? Is the elastic contact interaction still the dominant effect in the contact collisions between two micro-scale particles? How do waves propagate through such miniaturized systems? What are the effective roles of defects/disorder/surface properties and environmental conditions in the dynamics of micro-particles? What role do the particle-substrate interactions play? How do micro-scale granular crystals respond in water? These are some of the fundamental questions we will address in this thesis. Many of these findings extend beyond the limited realm of ordered granular lattices and provide general and fundamental insights into the physical response of micro-scale granular systems.

Despite the fundamental importance of understanding the physics of micro-granular systems, very little experimental work has been conducted at these scales. The lack of experimental investigation results from two major difficulties: first, the absence of reliable methods to assemble micro-particles in controlled configurations (as well as of methods to characterize their precise positions); second, the lack of a systematical way to measure the interaction between micro-granular particles and of the stress propagation through large particle arrays.

Granular crystals are highly nonlinear and discrete. These characteristics are reflected in enhanced practical difficulties in fabricating and mechanically exciting ordered lattices of small-size particles. Conventional experimental techniques, which are widely used in the study of macro-scale granular systems, cannot be directly employed or scaled down to test systems of micro-granules. To provide fundamental insights into the dynamics of micro-particles, it was therefore first necessary to develop a new experimental platform that allowed for repeatable fabrication methods, as well as for mechanical excitation and measurement of micro-granular systems.

We focused on the study of two micro-granular systems: (i) dry, one-dimensional granular systems that consisted of stainless steel micro-particles with a radius of 150 μm, and (ii) wet, two-dimensional granular systems that consisted of SiO_2 particles with a radius of 3.69 μm. In the dry micro-granular systems, we characterized the role of the substrate, the presence of friction, and the mechanics of collisions between two particles. We excited and measured propagation of nonlinear waves along one-dimensional micro-granular chains and studied the influence of inter-particle gaps on the system's group velocity. We further applied this experimental framework to study wave propagation

within a self-assembled colloidal system of SiO_2 particles, using both numerical and experimental approaches. We excited the wave propagation within the two-dimensional hexagonal lattice and characterized the role of hydrodynamic interactions within this system.

1.2. Background concerning granular materials

Because of its inhomogeneity, nonlinearity, disorder, and anisotropy, granular material is one of the most challenging subjects in solid mechanics [13, 14]. The experimental difficulties originate from the discrete nature of granular material; the irregularity of sizes, shapes, and materials compositions; and highly nonlinear inter-particle contact forces. The discreteness and the varying particle dimensions together impose difficulty in describing, characterizing, and reproducing granular system configurations. The high nonlinearity in these systems [15] further increases the experimental precision requirement, in which imperfection of the granular system does not even out as the system size grows and sometimes dominates the dynamics response of the system [16].

Due to the experimental difficulties, there are two major trends in the research of granular mechanics. One focuses on the collective and statistical behavior of unstructured granular systems [17-20] without seeking to reproduce exactly the same configuration of samples; it includes the study of granular gas [21-23], granular flow [24-28], particle segregation [29-31], avalanche [32-34], and compression and force in a granular medium [35]. The other approach is to focus on the subsets of granular material, in which the variation in size, shape, and material are limited and particle packing is simplified. One of these subsets is the granular crystal, which refers to highly ordered granular systems.

1.2.1. Ordered granular systems

Research on granular crystals has attracted great attention since the pioneering work done by Nesterenko [2]. He predicted the existence of highly nonlinear soliton-like waves in uncompressed one-dimensional homogeneous granular crystals, specifically an array of spherical particles, where neighboring spheres interact through the Hertzian force. Within the elastic limit of this system, if two neighboring spherical particles have center coordinate x_m, radius R_m, elastic modulus E_m, and poisson ratio ν_m, then the contact force between two particles locating at x_m and x_n is

$$f_{mn}(x_m, x_n) = \frac{4}{3}\frac{E_m E_n}{E_m(1-\nu_n^2)+E_n(1-\nu_m^2)}\sqrt{\frac{2R_m R_n}{R_m+R_n}}(R_m + R_n - |x_m - x_n|)_+^{\frac{3}{2}}, \qquad (1.1)$$

where $(R_m + R_n - |x_m - x_n|)_+ = \max(R_m + R_n - |x_m - x_n|, 0)$ is the positive overlap distance of the spheres (if they are not deformed). The equations of motion of the granular chain system are

$$m\,\ddot{x_n} = -\frac{2}{3}\frac{\mathrm{E}}{1-\nu^2}\sqrt{\mathrm{R}}((2\mathrm{R} - x_{n+1} - x_n)_+^{\frac{3}{2}} - (2\mathrm{R} - x_n + x_{n-1})_+^{\frac{3}{2}}). \tag{1.2}$$

Nesterenko solved these equations with long wavelength approximation [2, 3], in which the discrete coordinates of the nth particles, x_n is now redefined as the value of a continuous function of displacement x at position $2Rn$ in a continuous medium, $x_n \equiv x(2Rn)$. He obtained a solution,

$$v(z,t) = \frac{25}{16}\frac{{v_g}^5}{c^4}\cos^4\left(\frac{1}{\sqrt{10}}\frac{z - v_g t}{R}\right), \tag{1.3}$$

where $v(z,t)$ is the particle velocity at $z = 2Rn$, v_g is group velocity, and $c = \sqrt{8ER^3/3(1-\nu^2)m}$ is the wave velocity in the material. The results show a highly nonlinear dependency between the group velocity and the maximal amplitude of the particle velocity (maximum velocity),

$$v_g = \sqrt[5]{\frac{16}{25}}c^{4/5}{v_{max}}^{1/5}. \tag{1.4}$$

Once the existence of the predicted compact solitary wave was confirmed experimentally [36], numerous numerical [37-39] and experimental [9, 40-43] studies of this system were carried out.

The excellent properties originate from the highly nonlinear interaction, $f \propto \delta^{3/2}$, and it was proven in later years in rigorous mathematics that solitary waves exist in granular chains with arbitrary power-law ($f \propto \delta^n$) nearest-neighbor contact interaction [44-46]. This discovery indicates that the solitary wave is a universal phenomenon in granular medium and that it should exist in a large variety of systems that are made of granular particles with different shapes and types of contact force. It also means that the study of solitary waves in granular materials has fundamental importance in understanding the mechanics of granular materials.

Propagation of soliton waves in one-dimensional granular crystal has since been observed experimentally on several different granular particles, including ellipsoidal particles [47, 48], cylindrical particles [49], hollow particles [50], and heterogeneous media [51-53]. The roles of

dissipation [54], plasticity [9, 55] of the granular particles, and velocity tunability under pre-compression [42] have been characterized.

Research interests have advanced to understanding the interaction between two solitary waves [56-60] and between a solitary wave and the interface, boundaries [61], and defects [62, 63] of the granular material. The transmission of solitary waves through the interface between two granular crystals [64] and interface between a granular crystal and elastic medium [10] has also been studied. Yang et al. demonstrated that by sending solitary waves through the interfacing between a known granular chain and an elastic medium, site-specific material properties of the elastic medium can be obtained by measuring the time-delay and reflectivity of the solitary wave [65].

Significant attention has also given to the study of vibration modes and the band structure of granular chains [66]. Despite the highly nonlinear nature of the contact force, a sinusoidal driving can be considered as weakly nonlinear if the background pre-compression force along the chain is big in comparison to the amplitude of the driving force. Experimental and numerical investigations of highly compressed granular chain reveal the existence of band gaps and indicate the possibility of tuning the band gap by tuning pre-compression [67-71]. A particularly interesting case happens when defects (i.e., granular particles with different sizes, masses, or elastic moduli) are placed inside the chain. Boechler et al. conducted numerical and experimental research to reveal the existence of intrinsic localized modes, also known as breathers, in granular chains with defects [72, 73]. An intrinsic localized mode is a localized vibration centered at the defect and amplitude decay exponentially along the lattice. The localized mode has been shown to be universal phenomena in granular chains [16] and can be used for both acoustic switching and rectification [74].

The dynamics of two- and three-dimensional ordered granular systems are relatively poorly understood. While it is suggested that a squared lattice granular system should behave similarly to a one-dimensional granular chain when the solitary wave is propagating along the lattice vectors, a direct generalization of a solitary wave solution to two- and three-dimensional systems has yet been derived. As an intermediate step between one- and two-dimensional granular crystals, Daraio et al. investigated pulse branching and recombination in a y-shaped granular network [75], using the quasi-particle description of a solitary wave to derive transmission coefficients for y-shaped pulse splitting [76, 77]. Leonard et al. further developed an energy mitigation granular network that consists of a three-dimensional network of granular chains [78].

In the early experimental efforts on real two-dimensional granular systems, Shukla et al. used photoelasticity techniques to image wave propagation in various two-dimensional granular crystals, including cubic and hexagonal packing [47, 79-84]. Their experiments show that within higher dimensional granular crystals, the force load path is influenced by the contact angle between lattice elements and wave propagating is altered by the vector connecting the centers of mass of the neighboring particles. The new dimensionality not only introduces more interaction between particles, but also brings new degrees of freedom for designing and engineering the lattice to achieve the desired wave propagating properties. Leonard et al., who studied the wave propagation in two-dimensional square lattices of spherical particles [85], showed that inserting cylindered intruders into these lattices makes it possible to alternate both the wave direction and the energy flux [86].

Despite the good agreement between the average experimental results and wave propagation simulations, the results of experiments involving these two-dimensional granular lattices generally show low repeatability. The difficulty stems from the inability to construct "perfect crystals" in a repeatable fashion. Failing to reproduce perfect crystals has various causes, including the differences of granular particles in size, surface roughness, and shape. The small differences in size and shape do not only change the magnitude of contact force in neighboring particles [87], but they also cause the deformation of the lattice structure and create local compressive areas and gaps [88-90]. Small misalignments that are created by these defects divert force to neighboring particles and therefore scatter the wave propagation [89]. Another mechanism of disorder is through the presence of friction, in which tangential force diverts the wave propagation when the vector connecting the centers of the contacting particles is not parallel to their relative motion [91-93].

Numerical and experimental efforts are devoted to the randomness of granular chains and the influence of this randomness on wave propagation. Manjunath et al. studied random granular chains in which randomness results in the divergence of the magnitude of contact force in relation to neighboring granular particles [94]. They found that the peak amplitudes of propagating waves in random granular chains decay to the degree of randomness with an exponential law, and that the dependency later becomes a power law as randomness further increases. Ponson et al. studied experimentally the effect of randomness on the array of particles. Particles of two different material properties were selected to construct random arrays of diatomic granular crystals. The ratio between two particles defines the randomness of the system, and the researchers observed behavior that was similar to that of the exponential to power law transition [90].

To understand the influence of the polydispersity in higher dimensional systems, load transfer paths are studied numerically in compressed granular crystals [95-98] with different particle sizes. Larger imperfections such as point defects [99, 100] and size deviations [101, 102] of the granular systems have been found to alter the wave propagation more significantly than granular crystals.

1.2.2. Micro-scale granular systems

For particles with diameters of only a few micrometers, the Van der Waals interaction between the particles becomes relatively important. The most famous models describing the influence due to Van der Waals interaction are the Johnson-Kendall-Roberts (JKR) and the Derjaguin-Muller-Toporov (DMT) models [103-105]. In these models, the Hertzian elastic contact potentials are modified to include the electric dipole-dipole energy between particles. The inclusion of these adhesive forces changes the mechanical response of granular systems not only by changing the inter-particle interaction, but also by changing the interaction of the granules with the structures that support the granular assembly [106].

In the 1970s, P. A. Cundall developed a numerical method, namely the distinct element method (DEM), for computing the motion of large numbers of small objects [107, 108]. The DEM, which has since become one of the standard tools for numerical studies of system response in granular materials, enables researchers to predict the mechanical response of micro-granular systems of large numbers of particles through computer simulation.

On the other hand, scaling down the particles means that the traditional means of observing and identifying the configuration of a granular system does not apply to micro-granular systems. These experimental difficulties originate from the discrete nature of granular materials and their highly nonlinear inter-particle contact forces. This discreteness and the micro-scale sizes require efficient means to assemble the particles precisely, to excite them, and to measure their dynamic response. The high nonlinearity of these systems requires particularly high precision, and imperfections can be extremely important in controlling the dynamic response of the entire system.

Because of the difficulty of constructing repeatable micro-granular systems, the experimental study of micro-granular systems has been focused on unstructured granular systems, in which the exact configurations of micro-particles are unknown. The experimental studies on micro-granular systems are largely focused on the collective behavior of granular systems [109-111].

A special subset of ordered micro-granular systems is the micro-colloidal system, which consists of ordered two-/three-dimensional granular crystals that are created in water with self-assembly technology. Using photon correlation spectroscopy, Alan J. Hurd et al. measured the phonon dispersion curves and wavelength dependent friction factors [112]. More experimental studies using dynamic light scattering have also been performed to understand the over-damped collective behaviors; they have discussed both wall effects due to finite sample thickness (or confinement effects) and the role of ion behaviors in liquids [113, 114]. In 2004, P. Keim et al. first used video microscopy to study lattice dynamics, which allowed them to observe the harmonic lattice behavior of two-dimensional colloidal crystals with phonon dispersion curves [115, 116]. In later studies, lattice dynamics in one- and two-dimensional colloidal systems under various local substrate potentials produced by light have also been studied with video microscopy [117-120] and Brownian dynamics simulations [120, 121] to investigate the effects of local potential on the collective behaviors and phononic band structures.

Furthermore, the existence of fluid environments enriches the interaction forces by adding non-conservative hydrodynamic forces (such as viscous friction and many-body hydrodynamic forces) that arise from the relative motion of colloids [122-124]. Brownian dynamics simulation studies, where the motions are driven by entropic thermal fluctuations and the inertia of colloids is negligible due to their over-damped nature, have generally been performed to understand colloidal aggregation, phase transitions, and crystallization.

1.3. Contributions of this thesis

In this work, we study the fundamental dynamic response of micro-scale granular systems and design an innovative experimental platform that allows us to assemble, excite, and characterize ordered micro-granular lattices. This new experimental platform employs a laser system to deliver impulses with controlled momentum and non-contact measurements, including high-speed optical microscopy and laser interferometry, to detect the particles' displacement and velocity. We build and program a computer-controlled micro-manipulator that can position and assemble steel micro-particles in desired configurations for testing. We fabricate micro-structures to guide and confine the micro-particle assembly to allow interested dynamics to be tested. We test and demonstrate the capability of the laser excitation system to deliver controlled momentums to systems of dry (stainless steel particles of radius 150 μm) and wet (SiO_2 particles of radius 3.69 μm, immersed in fluid) micro-particles.

We first derive the governing equations of motion describing the dynamic response of dry and wet particles on a substrate, which we validate in experiments. To investigate the influence of micro-structure support on the dynamics of micro-particles loaded on the structure, we study the loss in our micro-particle configuration analytically and experimentally. We then measure the Stoke and Coulomb friction of the micro-particles by tracking particle-trajectories at varying initial momentum. Thereafter we study the collisions of rolling micro-particles in a groove to investigate the translational and angular momentum during collision. In observing inelastic collisions when the particles are rolling in the groove, we discover a linear dependency between the contact force and the tangential frictional force between the colliding particles. We also observe serious inelastic collisions when the spheres are rolling. Next we obtain an empirical equation of motions that describes the dynamics of the micro-granular system. We assemble one-dimensional dry chains of micro-particles and investigate the mechanical wave propagation properties as well as the influence of defects in these systems. Upon measuring the time of fly of wave that is propagating inside the chain at different initial input momentums, we show that measured group velocity depends on the initial velocity (which is a feature of wave traveling in granular systems with highly nonlinear interaction). We then examine the deviation of the measured group velocity with the Hertzian system and numerically show that the deviation can result from the presence of defects (which in this case are gaps between micro-particles). To prove this, we perform time of fly measurement for systems with a known maximum gap using the microscopic system and show that the measured group velocity agrees with numerical simulation.

We also study wave propagation in two-dimensional colloidal systems that are immersed in fluid. We employ self-assembling technology to create a two-dimensional hexagonal lattice in a micro-fluidic cell and apply the laser-based excitation to the system. We perform the experimental examination by sending laser energy into the system to excite the initial velocity of the six centermost particles in the lattice. The resulting high velocity (which is higher than what could be achieved using traditional means) allows us to explore the system while the particles have enough velocity to break through the hydrodynamic barriers and to study wave propagation in the system with different viscosities. We construct a model that includes the contact, hydrodynamic, electrostatic, and Stokes' drag forces and perform numerical simulation to study wave propagation at a time resolution higher than our experimental system. The simulation that results characterizes the roles of the hydrodynamic force and the contact within wave propagation and explains the origins of the isotropic wave propagation within the system.

Our finding represents the first systematic experimental and numerical analysis of wave propagation in ordered micro-granular systems. This work establishes the basis for further advancing studies of granular and colloidal systems and sheds light on the miniaturization of highly nonlinear granular devices.

1.4. Conceptual organization of this thesis

The remainder of the thesis is structured as follows:

In Chapter 2, we describe the design of the experimental platform that is used to carry out the micro-granular system.

In Chapter 3, we show the feasibility of utilizing pulsed laser ablation as a tool for delivering mechanical excitation to micro-particles. We experimentally calibrate the material response of the laser on different materials, as well as control the direction of transferred momentum.

In Chapter 4, we study the equation of motion of particles that are moving, rolling, sliding, and colliding in a groove. We also analyze the collisions between particles in a groove and provide empirical descriptions of the equation of motion for particles.

In Chapter 5, we construct one-dimensional micro-granular chains and study the wave-propagation within those chains. We measure the group velocity and attenuation of wave propagation. Via experiments and numerical simulation, we study the relationship between wave propagation and defects (the gap between micro-particles).

In Chapter 6, we apply the experimental setup to a micro-colloidal system and study the system's response to laser-generated impact. We also study the relation between striker velocity, viscosity, and decay length of the wave displacement of the particles in each force chain.

Chapter 2

Instrumentation

All experimental setups used to test the dynamic behavior of granular systems are composed of three basic elements that are used to assemble, excite, and measure the response of the granular system of interest. Conventional experimental techniques employed for macroscopic granular systems include piezo transducers for applying excitation [16, 66], sensor particles embedded with accelerometer [9, 42, 63, 125, 126] for force measurements, and laser vibrometers [16, 127] for measurement of selected particles' displacement and velocity. Most of these methods cannot be directly applied or adapted to micro-granular systems. For example, force measurement based on sensors that are embedded in selected particles is not possible in micro-granular systems due to difficulties in fabricating micro-particles with embedded accelerometers. Also, piezo transducers cannot be easily used to drive micro-particles, because of the high-precision requirements related to controlling the nano-scale contact surface conditions and stiffness.

Assembling ordered granular systems is another challenge that emerges when the size of the systems is scaled down. Experimental studies of ordered granular materials require repeatable and regular means to assemble the particles in selected geometries/lattices. High accuracy in packing the particles is particularly necessary given the nonlinear nature of the contact interaction between each pair of particles. Increasing the number of particles in a lattice then creates increasing challenges in assembling a reproducible sample for testing. One-dimensional granular chains are easier to assemble, because the presence of a small pre-compressive force can compensate for small irregularities between particles. However, for two-dimensional systems, creating a "perfect" lattice is difficult even at the macro-scale [128], and disorder and misalignment between the particles can significantly alter wave propagation.

At the micro-scale, the precise control of the physical contact between particles is more difficult. The accuracy required to ensure repeatable tests increases rapidly as the particle size is reduced. At the same time, the physical contact between micro-particles is no longer exclusively governed by elastic interactions; particles exchange forces also through other potentials (such as Van der Waals), which

can be significantly altered by surface quality, geometry of the contact, and a variety of other factors that are difficult to monitor in real time. All of these issues that arise at the micro-scale call for the design of an ad-hoc experimental setup that reduces uncertainties that are related to the driving and measurement systems and that allows for a repeatable and controllable assembly of one- and two-dimensional samples. The rest of this chapter details the design of our new experimental system.

In our experimental setup (Fig. 2.1), we introduce non-contact excitation and measurement methods to avoid influencing the response of the system with intrusive driving and detection systems. We also design a computer-controlled robotic micro-manipulator to assemble the micro-particles automatically in selected lattice geometries, thus ensuring high-packing repeatability. The experimental setup designed for this thesis consists of three major components: (i) The sample holders and the micro-manipulator system, which confine and assemble the micro-particles in precise locations; (ii) the excitation system, which delivers controlled momentum to a target particle using a Q-switched, nanosecond pulsed laser that is operating in single-shot mode; and (iii) the measurement system, which consists of laser vibrometry and high-speed microphotography. In this chapter, we discuss the sample preparation and the measurement systems. The excitation of the micro-particles is discussed in more detail in the next chapter.

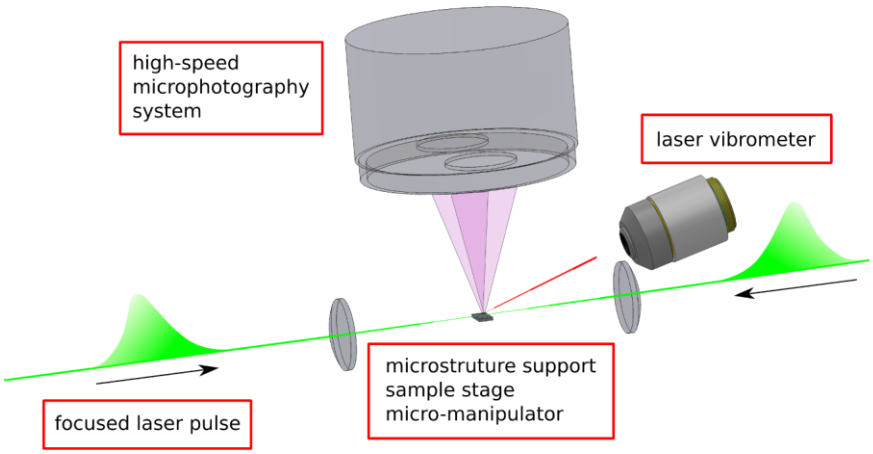

Figure 2.1: Overview of the experiment scheme. The apparatus consists of three major parts, including the excitation system (focused laser pulse), the measurement system (high-speed microphotography and laser vibrometry), and the sample assembly and manipulating system.

2.1. Particle confinement and sample stage

In this thesis, we focus on micro-particle systems that are assembled in one- and two-dimensional configurations. Two specific types of systems are investigated: (1) dry, one-dimensional granular chains that consist of stainless steel particles with a radius of 150μm, and (2) wet, two-dimensional systems that consist of silica spheres with a radius of 3.69 μm that are immersed in a water-glycerol solution with variable viscosity. For testing these two systems in the selected configurations, it is necessary to design specific supporting structures that guide and confine the movement of micro-particles. For the experiments on dry particles, we fabricate appropriate v-shaped supports using photolithography on a silicon wafer. To assemble two-dimensional, close-packed arrays of colloids in fluids, we use commercially available micro-fluidic cells as supports.

Once the micro-particles are loaded on the desired support structures, the experimental apparatus needs to (i) record the initial particle-configuration by identifying and locating all of the particles and (ii) modify the initial configuration to the particle-configuration of interest, which entails moving, positioning, and pre-compressing the micro-particles to ensure physical contact between them. As described in detail later, we perform this operation using a microscopic imaging system and a micro-manipulator.

We then mount the samples on a computer-controlled sample stage that consists of a pitch and roll platform (Thorlabs APR001) that is installed on a three-dimensional motorized stage (zaber T-LSM025A). The sample stage is leveled with an inclinometer (Level Developments IS-2-30) with an accuracy of 0.1°, which allows us to induce particle movement by tilting the stage. This sample stage reduces the difficulty of handling and manipulating the systems of micro-particles. In the following subsections, we explain the experimental construction of the two micro-granular systems (i.e., the dry and wet micro-granular systems) that are analyzed in this work.

2.1.1. One-dimensional micro-granular systems

The one-dimensional micro-granular systems considered in this thesis consist of micro-particles that are made of two different stainless steel materials, namely grade 316 and grade 440c. We list the dimensions and properties of these materials in Table 2.1. The two particles being studied both have a 300 μm diameter; their other similar physical properties include density, elastic modulus, and Poisson ratio. The most significant difference between them is surface roughness, which is an important source of imperfections in micro-granular chains. According to the specifications provided

by their manufacturers, the stainless steel 316 particles have a nominal surface roughness of 3 μm, while the 440c particles have a smaller surface roughness of 0.1 μm. The difference in surface quality can be seen in the scanning electron microscope (SEM) images of the two particles in Fig. 2.2. As we show in the following chapters, systems made of the higher surface quality particles of stainless steel 440c have a mechanical response that better agrees with the theoretical and numerical predictions of granular systems that are composed of ideal particles. Another noticeable difference between the two types of particles is their thermal conductivity; stainless steel 440c has a nominal thermal conductivity (24.2 W/mK) that is about 50% higher than that of stainless steel 316 (16.3 W/mK) [129]. This affects the efficiency of the laser excitation we used to drive the system, which is discussed in Chapter 3.

Due to the small size and mass of the individual micro-particles, configurations of micro-granular systems are vulnerable to static charges and external magnetic fields. Electrically charged particles strongly repel each other and cannot be arranged in an ordered lattice. To avoid these issues, all particles are rested on a conducting metal disk to remove unwanted static charges before they are assembled into specific configurations. Magnetic fields, even those generated by magnetic objects such as metal tools, attract the stainless steel 440c particles. To avoid magnetic interferences during assembly, we transport the particles to the supporting structures with either a very light blow of compressed air or tweezers made of non-magnetic materials.

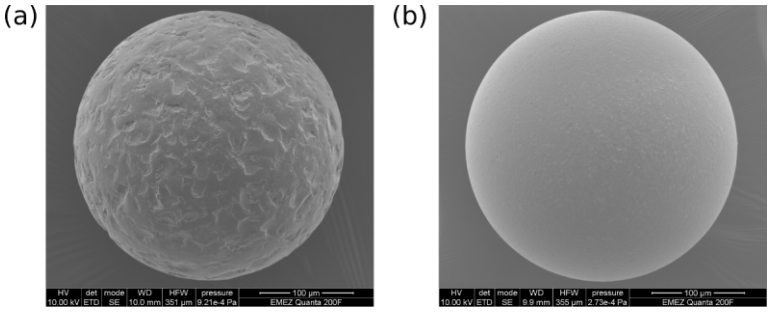

Figure 2.2: An SEM image of micro-particles used in this experiment. (a) Stainless steel 316 particle with a radius of 150 μm and surface roughness of 3 μm. (b) Stainless steel 440c particle with a radius of 150 μm and surface roughness of 0.1 μm.

Material properties	Stainless steel 316 particle	Stainless steel 440c particle
Radius (μm)	150	150
Radius variation (±μm)	2	1
Surface roughness (μm)	3	0.1
Density (kg/m^3)	7990	7650

Elastic modulus (GPA)	193	200
Melting point (K)	1660	1760
Thermal conductivity at 100C (W/mK)	16.3	24.2
Specific heat (J/kg/K)	510	460

Table 2.1: Dimensions and material properties of our stainless steel micro-particles [129, 130]. Particles made of stainless steel 316 and 440c are used in this work. These two particles have similar physical properties except for the significant differences in surface roughness and thermal conductivity.

To create a one-dimensional micro-granular system, we deposit the particles on v-shaped grooves that are fabricated on silicon wafers. The grooves constrain the particles from moving along the axis of the groove. The fabrication procedures are shown in Fig. 2.3a. Starting with a [100] silicon wafer with a thickness of 1 mm, we deposit a 1 μm thick layer of silicon nitride (Si_3N_4) on the surface via chemical vapor deposition. The wafer is then patterned with 1.6 μm of AZ5214 positive photo-resist, before the silicon nitride layer is opened up with reactive-ion etching (RIE) techniques. The wafer is subsequently treated with a 50% potassium hydroxide (KOH) solution at 85ºC to perform anisotropic chemical etching. This etching process removes unmasked silicon, reveals the [111] crystal planes, and forms v-shaped grooves (Fig. 2.3b). The grooves we use in the experiments have a width of 240 μm and we estimate the surface roughness to be 0.1 μm according to the fabrication process [131]. The angle between two inclined [111] planes is 70.6º.

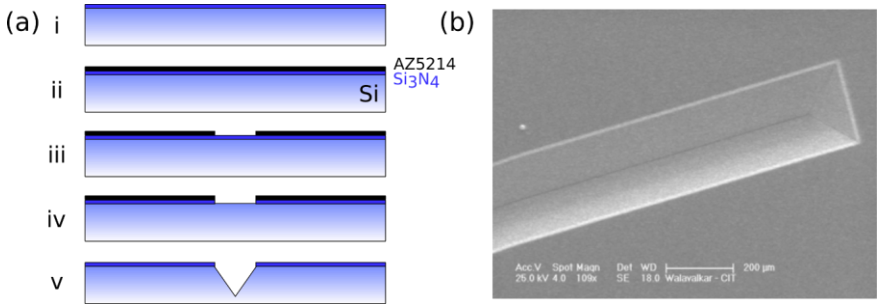

Figure 2.3: Micro-fabrication process of one-dimensional v-shaped grooves with a width of 240 μm and an inclined angle of 70.6º. (a) Overview of the fabrication process: i) Chemical vapor deposition of a 1μm thick layer of silicon nitride (Si3N4) on the surface of a 1mm thick silicon wafer [100]. ii) Spin coating with 1.6 μm of AZ5214 positive photo-resist. iii) Exposing and developing the photo-resist. iv) Patterning the silicon nitride layer with reactive-ion etching (RIE). v) Anisotropic chemical etching with a 50% potassium hydroxide (KOH) solution at 85ºC. (b) An SEM image of the resultant v-shaped grooves.

Once the particles are placed in the v-shaped groove, we manipulate them with a computer-controlled micro-manipulator to align them and secure contact between them. The micro-manipulator consists of a sharp tip (a stainless steel micro-wire with a tip size of 100 μm) that is installed on a three-dimensional motorized stage (zaber T-LSM025A). The micro-manipulator moves the micro-particles by physically pushing them from one side. The position of the micro-particles is determined by image processing, using a microscopic photography system. The sequences of the micro-manipulator movements are determined by a control program. The motion is determined based on the difference between the current configuration (as detected by the imaging system) and the desired configuration (which is preset in each experimental run). More details concerning the particle manipulation procedures are given in Section 2.5.

To construct a micro-granular chain, we use our computer-controlled sample stage and the micro-manipulator system to assemble close-packed micro-particles in a v-shaped groove. We start by loading the particles randomly into the v-shaped groove, after which we blow along the groove with compressed air to form a loose chain of particles. To minimize the gap between particles and create a close-packed chain of micro-particles, we tilt the computer-controlled sample holder by 10° from horizontal place while simultaneously positioning the micro-manipulator to the lower end of the groove to block the free-moving particles from rolling out (see Fig. 2.4). After particles form a close-packed granular chain, we slowly tilt the sample stage back to a horizontal position and withdraw the micro-manipulator carefully so as not to disturb the chain.

To characterize the assembled chain before each measurement, we acquire microscopic digital images to record the initial position of each particle. Using photographs taken by our imaging system (Fig. 2.4b), we determine the location of the particles at a 2 μm accuracy with an image-processing algorithm similar to what was mentioned in Chapter 2. Since gaps between particles can be as small as tens of nanometers, which is far below the diffraction limit of our imaging system, the image-processing algorithm cannot resolve the presence of individual gaps. However, by measuring the total length of the micro-particle chain, we can estimate an upper bound of the average gaps that are present within the chain. According to the specifications provided by the manufacturer [130], the stainless steel 440c micro-particles used in our experiments have a variation in radius of $\pm$1 micrometer. In a chain that is composed of 15 particles, the resulting uncertainty in the total length of the chain is $\sigma_{total\ length} = 2\sqrt{15-1}\sigma_{radius}$ micrometer. After the construction of micro-chains, if we opt to

test only the chains that have a total measured length that is below average, we can estimate that the upper bound of the average gap is not larger than $2\sqrt{14}\sigma_{radius}\,/14 = 500\,nm$.

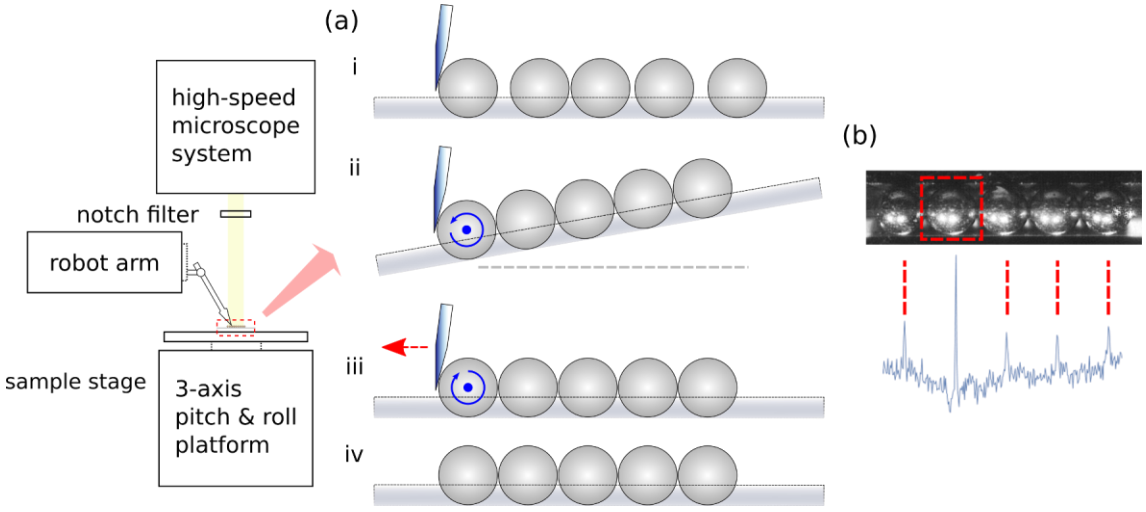

Figure 2.4: Procedures for assembling a micro-granular chain. (a) i) Micro-particles are positioned loosely in a v-shaped groove. ii) The sample stage is tilted to create a close-packed granular chain, blocked at one end by a robotic tip. iii) The sample stage is tilted back horizontally and the tip is withdrawn. (b) Optical imaging system to determine the locations of the particles using an image-processing algorithm. The image of the particle in the red box is used as the kernel of the image deconvolution, to reveal the position of other particles. The blue curves below show the results of the deconvolution algorithm, through which the other four particles are detected. A particle's position can be obtained with 2μm accuracy.

2.1.2. Two-dimensional micro-colloidal systems

Another type of micro-granular system that we investigated in this thesis is the two-dimensional system of colloidal particles immersed in fluid. The micro-particles (MicroParticles GmbH) are SiO_2 particles with two different radiuses (Table 2.2) of 3.69 and 3.14 μm. These two types of particles differ slightly in size and mass but have the same material properties.

Material properties	SiO_2 particles 1	SiO_2 particles 2
Radius (μm)	3.69	3.14
Radius variation (μm)	0.12	0.12
Refractive index	1.42	1.42
Density (kg/m3)	1850	1850
Elastic modulus (GPA)	73	73

Table 2.2: Dimensions and material properties of the colloidal particles used in the wet, two-dimensional experiments.

The supporting structures used to confine the two-dimensional motion of the SiO_2 particles is a commercially available micro-fluid cell (Hellma Analytics, Fig. 2.5a) that has a high quality quartz interior flat surface. Two-dimensional ordered granular systems are created within the cell using self-assembling techniques: after the particles are first injected into the cell with water, we tilt the cell to 5° along the long axis of the horizontal plane (Fig. 2.5b). After the particles cumulate on one side (Fig. 2.5c), the cell is tilted back to a horizontal position, which allows the piled up particles to relax and slowly move back toward the other side of the cell. In this relaxation process, micro-particles can form a hexagonal lattice after the system is stabilized. In Fig. 2.5d, we show the hexagonal lattice that is created. The dark particle in the center is a particle that is coated with a metal layer to enhance its interaction with the laser excitation system, which we explain in Chapter 3.

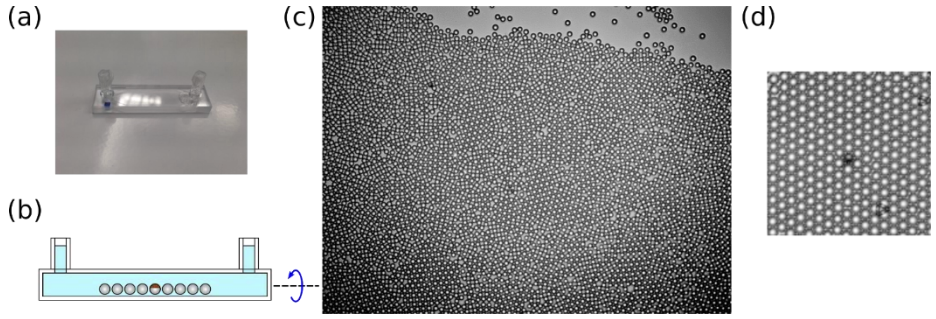

Figure 2.5: Preparation of two-dimensional micro-colloidal systems of SiO_2 particles. Hexagonal lattices are created by self-assembling techniques. (a) The micro-fluid cell used in this experiment. (b) A schematic diagram of the cell tilting process. (c) A digital image of dense, disordered micro-particles in the cell at the beginning of the relaxation process. (d) The final hexagonal lattice with a coated particle in the center.

2.2. Laser power controlling and beam conditioning

The mechanical excitation of the micro-particles is obtained with a focused, high-power laser beam that targets the surface of selected particles. The temperature rise that is induced by the focused pulsed energy results in the vaporization and removal of the particles' surface materials. This phenomenon is known as pulsed laser ablation (PLA). When ablation is induced on the surface of a micro-particle, the reaction force from the ablated material pushes the particle forward. The momentum transferred to the targeted particles is proportional to the velocity of the ablated materials, as well as to the mass

of the vaporized surface materials. With this technique, we can deliver controlled impulses to selected particles that result in the motion of these particles with a controlled initial velocity. We look into the details of the ablation process in Chapter 3; here we just focus on the optical systems that guide the laser beam to the sample.

The laser system is responsible for producing accurate, repeatable mechanical excitations to the system of micro-particles. The requirements for performing reproducible experiments are proper conditioning of the beam profile, control of the laser power, and focusing. The laser system in use is a 532 nm wavelength, Q-switched Nd:YAG nanosecond laser (Quantel Brilliant) with a maximum power of 3.2 W. The laser beam has a linear polarization and energy stability of 2% and the pulse duration is 4 ns. To improve beam quality and focusability, we install a spatial filter (Thorlabs KT310) at the output of the laser beam to create a clean Gaussian beam profile.

The total laser beam output can be controlled manually by an internal attenuator that is located inside the laser body. Since the maximum laser power achievable by our system is too high for the optimal range of operation of our experiments, to prevent excessive damage to the sample we limit the actual output of the laser to 5 mW. The beam is then passed through a combination of a half-wave plate and a polarized beam splitter to further control the laser power that will be delivered to excite the sample. The beam is split into two by a polarized beam splitter. In one arm the beam is sent to the sample holder, while in the other arm it is monitored by a power meter. The ratio of the power of the input beam, I, to the power of the output beam, I_1, is determined by the angle between the axis of the half-wave plate. The polarized angle of the beam, θ. I_1 can be expressed as: $I_1 = I(\frac{1}{1+v} + \frac{v}{1+v}\sin(4\theta - 4\theta_0))$. Here v is visibility and θ_0 is a constant offset that depends on the polarization angle of the laser beam and on the angle of the polarized beam splitter.

Before experiments are conducted, the laser power is calibrated at different θ to retrieve accurate values of v, I, and θ_0. This process allows us to accurately control the output power. The control of the laser power is also enhanced by the computer-controlled motorized rotational stage (Thorlabs PRM1Z8, PRM1Z8E) that supports the half-wave plate. The motorized stage has an angular resolution of 0.03º, which corresponds to a power resolution of 0.1% of the maximum power. A computer-controlled optical shutter (Thorlabs SH05, SC10) is also installed to block and prevent the beam from damaging the samples when the laser is operating.

2.3. Measurement system

The dynamic response of the micro-particles on the sample stage is measured by two independent methods: a laser vibrometer and a high-speed microscopic imaging system. We use a laser vibrometer to measure the velocity of the micro-particles and use the high-speed imaging system to measure the trajectory of the micro-particles.

2.3.1. Laser vibrometry

Laser vibrometers measure the velocity of the targeted surface via Doppler effects of reflected laser beam from the target. Considering the surface curvature of our micro-particles, it is necessary to focus the beam to a size much smaller than the particle's radius. For focusing the laser beam to a 3μm spot size, we install an objective lens (Mitutoyo PLAN APO 10x) on the vibrometer.

The laser vibrometer (Polytec OFV-534, OFV-5000) can achieve a resolution of < 1 pm and has a maximum sampling frequency of 2.5 MHz in DC mode and 24 MHz in AC mode. The output of the vibrometer is recorded by a high-speed data acquisition system (AlazarTech ATS9462) at a maximum acquisition rate of 180 MS/s, which is higher than the upper limit of the frequency band of the vibrometer.

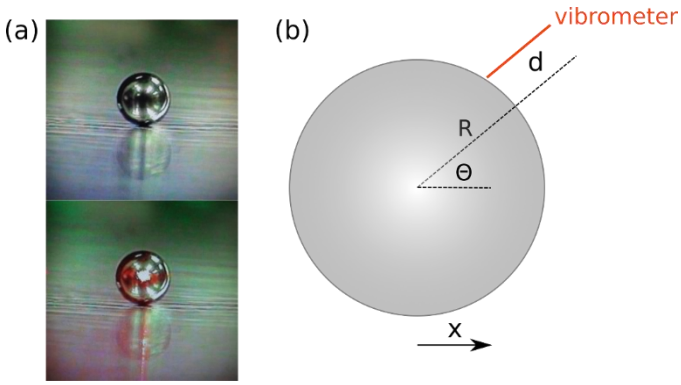

Figure 2.6: (a) Photograph of a laser vibrometer shining on the surface of particles with a radius of 150μm; the beam waist of the vibrometer beam is 3μm. (b) Schematic diagram of a realistic use case of a vibrometer being used on micro-particles. The red line indicates the beam of vibrometer, while d is the offset of the beam to the center of the particle and θ is the angle between the particle displacement, x, and the laser beam.

The requirements of laser focus on the particles impose many restrictions on the experiments that can be conducted. The vibrometer can only be focused on particles that are lying within the laser's focal

plane. This limits the ability to use the vibrometer to track moving particles, as these particles move rapidly out of the field of view. As a result, the range of displacement acquisitions is limited to only the first few μm of the micro-particle's motion.

The size and surface curvature of the micro-particles also introduce additional complexity to the measurements (Fig. 2.6b). Because of the limitations dictated by the physical geometry of the experimental system, the laser vibrometer is usually pointed at the particles with an inclined angle that is between 10º and 40º with the horizontal place. Since Doppler effects only account for the motion of the particle parallel to the axis of the vibrometer's beam, we expect the measured velocity to be different from the real particle velocity (which is along the horizontal plane).

This problem can be accounted for by measuring experimentally the ratio between the measured velocity and the actual velocity. In our measurements, we obtain a correction factor by measuring the displacement of the particle on the sample stage while moving the stage by computer in a known direction and distance (Fig. 2.7). The ratio between the two can be used to correct the velocity data obtained by the vibrometer. Typically, the correction factor for a given system configuration is calculated between 0.6 and 0.9; it is mostly affected by the inclined angle of the vibrometer. Using the symbols defined in Fig. 2.6b, it is not difficult to derive the following formula for the displacement $d^{(m)}(d)$ as measured by the vibrometer:

$$d^{(m)}(d) = \sin(\theta)^2\sqrt{1+\tan(\theta)^2}\,(x\cot(\theta)^2 - \sqrt{(-d^2+R^2)\,\cot(\theta)^2\,\csc(\theta)^2} + \sqrt{\cot(\theta)^2\left(R^2\cot(\theta)^2 + \big(R-x-d\,\csc(\theta)\big)\big(R+x+d\,\csc(\theta)\big)\right)}), \quad (2.1)$$

where x is the displacement of the particles, θ is the angle between the beam direction and the particle displacement, d is the offset of the laser beams to the particle center, and R is the particle radius. This formula also indicates that the measured velocity is linearly proportional to the actual particle velocity and that the inclined angle dominates the correcting factor.

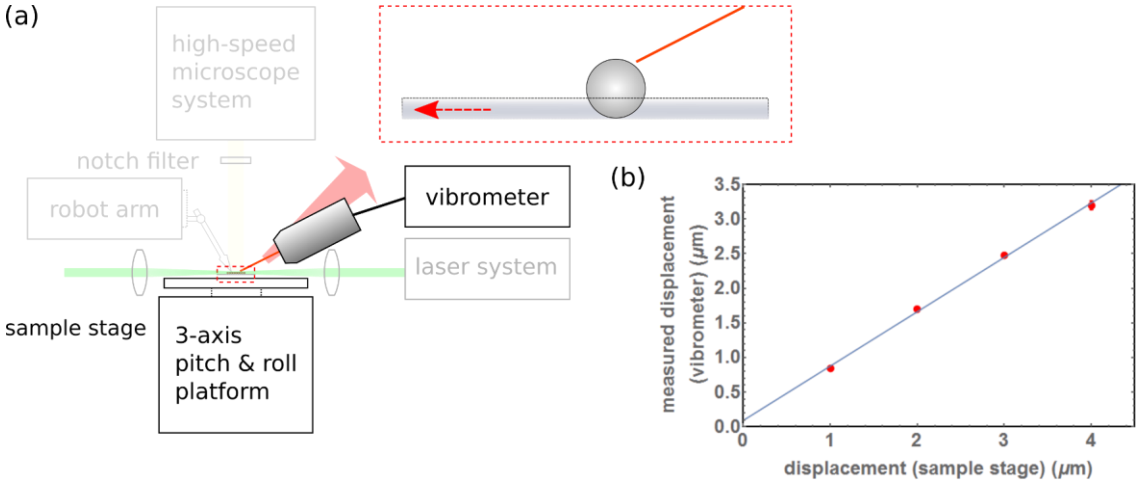

Figure 2.7: Calibration of vibrometer output. (a) Calibrations are performed by focusing a laser beam on the surface of a micro-particle and then using the computer-controlled sample stage to move it along its expected direction of motion in experiments (i.e., along the axis of the v-shaped groove). (a) The measured displacement (red dots) compared with the displacement of the sample stage (and the particle). The slope of the (blue) fitting line shows that there is a factor of 1.24 between the output velocities of the vibrometer and the real velocities in the horizontal plane.

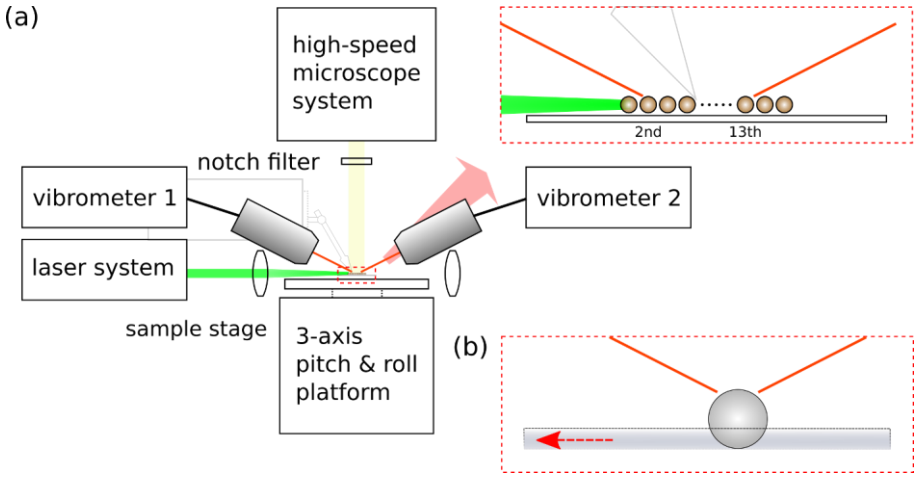

Figure 2.8: Schematic diagram of the experimental setup. (a) Two laser vibrometers are pointed on the micro-granular chain that is constructed with the procedures shown in Fig. 2.4. The granular chain consists of 15 particles and the vibrometers are pointed at the 2nd and 13th particles. (b) Calibration of vibrometer output. Two vibrometers are focused on the same particle. To calibrate vibrometer measurements, we point two vibrometers on the same particles and measure the relative time delay in output signals.

In Chapter 5, we measure the wave speed of the pulses traveling through the chain. Two vibrometers are used to measure the motions of two separate particles in the chain, and we measure the difference in arrival time (Δt) of the traveling wave at these two locations, as shown in Fig. 2.8. Due to the constraints on the available workspace, the two vibrometers need to point at the particles in the chain at different angles and in opposite directions along the groove (Fig. 2.8a). Besides the different output amplitudes caused by the different angles of the laser beams, processing the signal introduces an additional time delay of a few microseconds to the output signals of each vibrometer. In order to ensure meaningful comparison of the output signals of the two vibrometers, calibration must be used to determine both the time delay between the two output signals on the same event and the output voltage level for both vibrometers of the same particle velocities along the axis of the chain. The calibration process is similar to what we describe in the case of one vibrometer, except in this case two vibrometers need to be calibrated using the same object (Fig. 2.8b). To do this, the two vibrometers are moved to focus on the same particle (while maintaining the same angle to the chain); and the target particle is then moved with the computer-controlled sample stage. From reading the voltage output of both vibrometers, we know the scaling of the output signals, as well as the time delay between the outputs of the two vibrometers

2.3.2. High-speed micro-photography

We use high-speed cameras (Vision Research Phatom v12.1 and v1622) to record the trajectories of micro-particles that are excited by a controlled impact. After acquisition, the images are analyzed with an image-processing program to extract the displacement and velocity of the particles in the system. In this work, we deal with two micro-granular systems at two very different length scales (stainless steel particles of radius 150 μm and SiO_2 particles of radius 3.69 μm); different optical lens systems are therefore used for the best results in both cases.

Imaging the dry micro-particles requires a large field of view in order to capture sharp images of all of the stainless steel micro-particles that contribute to the dynamics. To accomplish this, the high-speed camera is equipped with a microscope (Leica S6D) with a large depth of field and achromatic lens pairs (Thorlabs MAP1050100-A) and is aligned and mounted vertically on top of the sample stage. A notch filter with a 532 nm central wavelength is installed to protect the CMOS sensor of the camera from the focused laser beam. The imaging system provides a spatial resolution of 4.3 μm per pixel and the field of view is 5.5 x 3.4 mm^2. The acquisition rate is limited by the shortest feasible

exposure time (39 µs in our system), which depends on the available illumination (we use a Fiber Optic Illuminator, 250 W). In our setup we achieve a maximum acquisition rate of 25,000 fps.

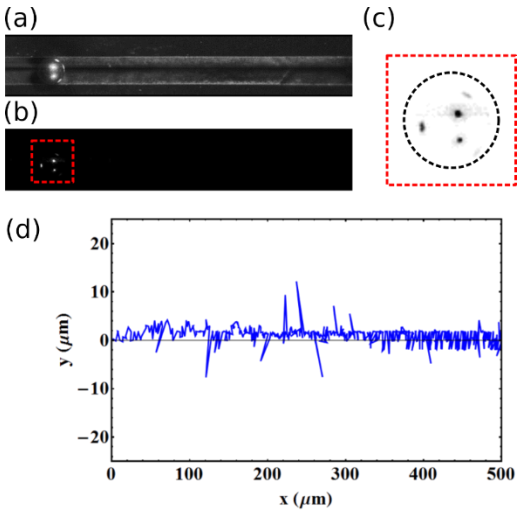

Figure 2.9: Image processing of the high-speed image sequence of a micro-particle moving on a groove. (a) Image of a micro-particle in a microstructure with an exposure time of 990 µs. (b) Image of the same particle with an exposure time of 39µs. (c) A portion of (b) is manually selected for use as the kernel of the deconvolution algorithm. (d) Resultant trajectory of the micro-particle moving under the camera.

To extract quantitative information from the high-speed images, we write an image-processing program to automatically detect a particle's position and measure its velocity. Each frame in the high-speed image sequence is deconvoluted to identify relevant tracking features and record the particle's position. Figure 2.3a shows typical high-speed images obtained when a single particle positioned in the v-shaped groove is moving. In this acquisition, the high-speed camera was operated at 1,000 fps with an exposure time of 990 µs. By decreasing the exposure time to 39 µs (25,000 fps), a higher time resolution can be obtained (Fig. 2.9ab). In this case the illumination is not sufficient to provide a clear view of the particle's edges and the particle's position is tracked following reflected light spots on the particle's surface. The image of the particles that is shown in the red box of Fig. 2.9b,is selected manually and used as a reference point for the particles in low light conditions.

Starting from the first frame, our program searches the next frame in the movie for areas that are similar to the image of the particles in the previous frame. We use image deconvolution to resolve the location of such areas and therefore the location of the particles. The particles' positions are then updated at each time step by searching for the trackers within a small window of their previous

position. Typical particle tracking results are shown in Fig. 2.9d. Because the deconvolution algorithm utilizes 50 x 50 pixels of information for each particle, the location of the particles can be determined with a sub-pixel accuracy. The observation can be confirmed in Fig. 2.9d, where the fluctuation of particle location is about 2 μm (which is less than the image resolution of 4.2 μm). A particle's velocity can be calculated by dividing its travel distance by the exposure time.

For the wet particles, we use a commercial available lens tube (Infinity) with a microscope lens (NIKON LU Plan Fluor EPI P 20x) to achieve micro-scale image resolution. We obtain a spatial resolution of 0.90 μm per pixel and a depth of field of a few μm. With the illuminating light now focusing on a much smaller area, we are able to acquire clear images at an exposure time of 2.7 μs and a maximum of 311111 frames per second, with a resolution of 128 x 128 during typical data acquisitions.

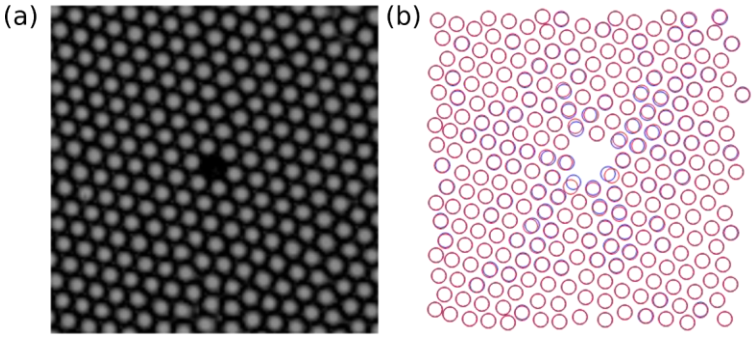

Figure 2.10: A typical high-speed image of the wet two-dimensional micro-granular system and the results of image processing. (a) Image of a micro-particle in a microstructure with an exposure time of 2.7 μs. (b) Resolved positions of colloids with image processing algorithm. The blue circles are the initial positions at t=0, while the red circles are the positions after 3.3 μs.

The particles are tracked with an image processing software following a working principle that is similar to the one used in the case of dry particles. In Fig. 2.10, we show the images obtained by the high-speed imaging system (Fig. 2.10a) and the resolved particle positions in the frame before (blue circles) and after (red circles) the system is excited by the laser. Notice that the resolved particle positions (Fig. 2.10b) do not contain all of the particles in the original photography (Fig. 2.10a). This can occur when some particles move out of the focal plane of the camera, or when some particles move too fast for the program to capture.

2.4. Configuration of the laser focusing system

The high-power laser beam is used to deliver controlled momentum to the micro-particles in different configurations. Since the samples tested vary significantly in their requirements and geometric assemblies, the laser beam configuration is also different in each case. The following subsections provide more details of each sample's design and utilization.

2.4.1. One-dimensional micro-granular systems

In Fig. 2.11, we plot the laser configuration used to excite the dry micro-particle chains. Before the laser beam reaches the micro-particles, it is focused with a lens that has a 60 mm focal length and a beam waist of 15 μm at the focal point. In order to ensure that the particles gain their momentum along the groove, the beam needs to be aligned to shine into the v-shaped groove in order to reach the outer-most particle.

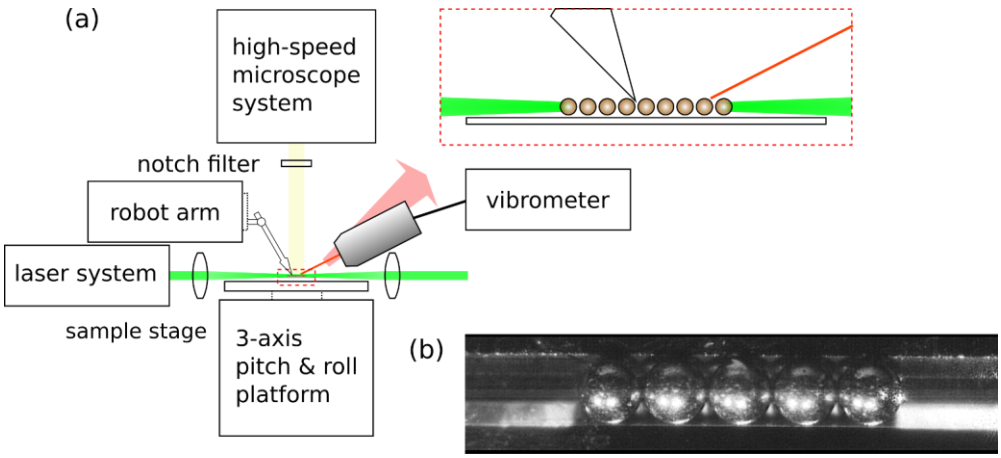

Figure 2.11: Experiment configuration for one-dimension micro-granular systems. (a) Micro-particles loaded on the supporting structure are assembled to the desired configuration by the computer-controlled micro-manipulator. The samples are monitored with a high-speed imaging system above the sample holder and a vibrometer that is pointed at the surface of a micro-particle. The focused laser beam with 15 μm is aligned to shine at the outer-most surface of the particle to excite the sample. (b) One-dimension micro-granular chain assembled in a v-shaped groove.

2.4.2. Two-dimensional colloidal hexagonal lattices

In Fig. 2.12, we show the laser configuration we used to excite the wet micro-particle systems. The SiO_2 micro-particles are arranged in hexagonal lattices in a micro-fluidic cell made of transparent material (quartz). The transparent material used for the cell allows the laser beam to transmit through

the cell from below. The laser beam is merged with the illumination and passes through an objective lens (Mitutoyo 20X) to focus at the same focal plane of the high-speed imaging system (which is also the location of the micro-particles). The laser is targeted at the dark particle in the center of Fig. 2.12b, which is an SiO_2 particle coated with a metal layer (non-transparent). The resulting dynamic response is monitored by the high-speed imaging system above the sample stage, which is protected by a notch filter that is blocking the pulsed laser from the sensor of the high-speed camera.

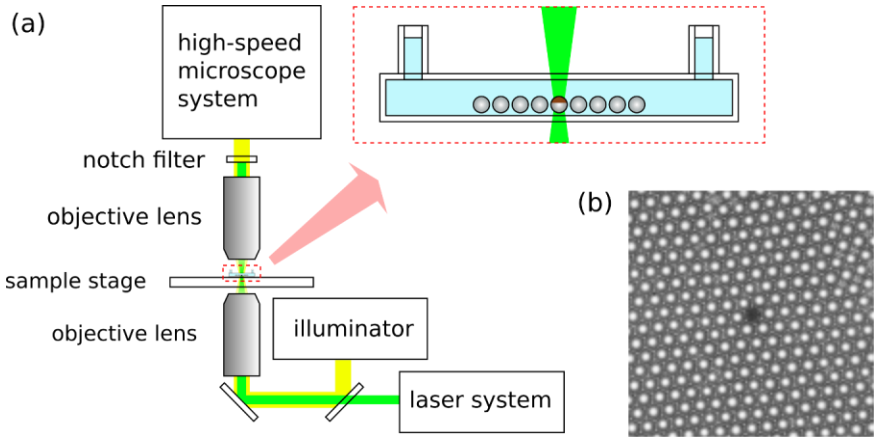

Figure 2.12: Experiment configuration for colloidal systems. (a) SiO_2 particles are injected into micro-fluid cells made of transparent material, in which self-assembled hexagonal lattices are created. The laser beam is merged with the illumination and focused at the same focal plane of the high-speed imaging system. The laser is targeted at the coated SiO_2 particles at the center of the lattice. The resultant response is measured by the high-speed imaging system above the sample. (b) Hexagonal lattice of SiO_2 micro-colloids.

2.5. Software system and lattice construction

To take full advantage of the ability of the experimental system, we used LabVIEW to create a united software interface to communicate with all of the instruments built within the apparatus. Each instrument is controlled by individual LabVIEW blocks that reproduce the physical user interfaces. These blocks are written following the programming architecture of queued state machines. To increase the flexibility of operation, each device can be detached or installed independently in experiments. When hardware failures (such as a loose cable) are detected, the control program automatically disables the corresponding LabVIEW block(s) to prevent damage to the instruments.

A central controlling block communicates with all blocks, as well as with pre-written queue commands in each LabVIEW block. The device blocks communicate with each other through the central controlling block. All steps of the experiments are decomposed into lists of sequential commands. The controlling block ensures that each step of an experiment is being successfully performed in the correct order. This automated control system minimizes experimental errors.

On top of the software system, we developed a sophisticated particle assembling and positioning subroutine that controls the micro-manipulator in order to create the desired configuration of micro-particles on the micro-structure support. Before the process begins, the location of all particles is detected by processing all images of the microscope sequence. The program then automatically generates a sequence of micro-manipulator operations, which is then sent to the LabVIEW controlling blocks. An example of particle assembly and positioning is given in Fig. 2.13, in which the goal is to relocate the two particles to the targeted position marked by the red crosses. The micro-manipulator moves micro-particles by physically pushing them from one side. Figure 2.13a-d shows four basic manipulations of micro-particles along a v-groove, including pushing the particles to the left (or right) and separating particles that are in contact. The positioning of the particles is completed using the following steps: (i-iii) open a small gap between the two particles in contact by lightly brushing on one of the particles from the top; (iv-v) after enough space is available, separate the two particles; and (vi-viii) push the micro-particles to the target position. The central controlling block monitors the progress and completion of each step. If one of the steps fails, our algorithm re-sends the same step to the micro-manipulator or re-generates the entire procedure, if necessary.

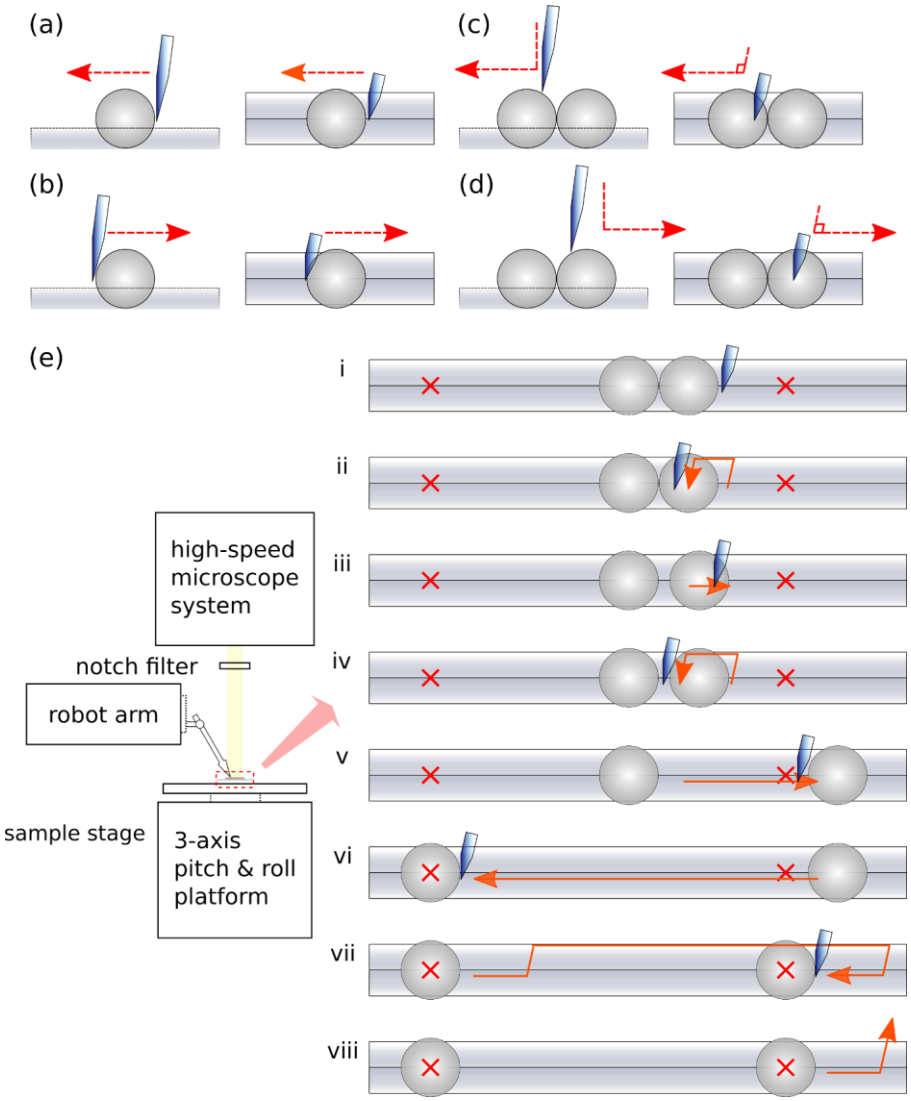

Figure 2.13: An example of the procedure for positioning and assembling micro-particles. (a-d) Schematic of four basic manipulations of a micro-particle, including pushing the particles to the left (right) and gently touching the particle from the top to open up gaps. (e) Procedures of relocating micro-particles to the two targeted positions that are marked by the red crosses. i-iii) open a small gap between the two particles in contact by lightly brushing on one of the particles from the top; iv-v) after enough space is available, separate the two particles; vi-viii) push the micro-particles to the target position.

Chapter 3

Mechanical Excitation via Pulsed Laser Ablation

The mechanical excitation of a granular system can be achieved by applying a controlled force or momentum vector to one or more parts of the granular system. Knowing and controlling the applied force, or initial velocity, are the starting points for numerical, theoretical, and experimental investigation of the system. Conventional means to mechanically excite a macroscopic granular system include using collision with a particle at controlled momentum [125] or actuating the system with a piezo transducer [16]. However, both of these methods rely on making physical contact with individual particles in the system. For example, experimentalists use collisions of freely moving particles to deliver momentum on target particles in granular systems. The freely moving particles (i.e., the strikers) need to be accelerated under a given potential before interacting with the granular system in order to reach a predetermined initial velocity. Fine aiming and precise control of the trajectory requires the accurate holding and releasing of the strikers in the potential field. For macroscopic particles, holding and releasing strikers from their initial position can be achieved by solenoids [132] or electromagnets [133]. In these cases, after being released the striker particles move along a predesigned path and apply initial conditions to the granular systems via collisions.

Achieving such controlled initial conditions at the micro-scale, however, is experimentally challenging, especially when adhesion forces can exceed the weight of the micro-particles. Adhesion forces (such as Van der Waals) and capillary forces both alter the trajectory of the strikers and therefore affect the collisions between the strikers and the target particles. The interaction between particles depends heavily on the particles' surface quality, which can degrade over time and must be monitored in real time. Therefore, a real-time verification of surface qualities, contact points, and particles' geometries is essential for the mechanical excitation of micro-granular systems. To create an experimental setup that can impart repeatable and controllable initial conditions to a micro-scale granular system, it is important to monitor the particles' geometries, the surface conditions of the contact area, and the adhesion properties of the particles with their substrate.

Pulsed laser ablation (PLA) is a process that is used widely in industry for material removal [134]. Ni et al. recently showed that PLA can be applied to generate solitary waves within macro-scale granular chains [135]. By vaporizing a controlled amount of water deposit on the surface of macro-scale particles, mechanical stress is created at one end of granular chains, which in turn generates traveling solitary waves within the chain.

In our work, we use PLA as a tool to deliver controlled momentum to a micro-scale granular system. By shining a focused laser radiation on the surface of a selected micro-particle in the system, we deliver momentum to that micro-particle, which then accelerates and acquires a controlled velocity before striking other target particles. In order to use PLA as a reliable tool for exciting micro-scale granular systems, we need to be able to predict the magnitude, as well as the direction and the variation of the striker's velocity. In the first section of this chapter, we review the history and background theory of pulsed laser ablation. In the second section, we examine the ablation process on micro-particles that are made of two different materials. We investigate the energy and directional stability of the ablation process as a tool for exciting dry micro-particles in air. In the third section, we investigate PLA as a means to excite colloidal particles in fluid. We summarize the advantages of the PLA method in the fourth section. The knowledge gained in this chapter lays the groundwork for the mechanical excitation and experimental study of dry and wet micro-particle systems in one- and two-dimensional configurations.

3.1. Theory of laser ablation for nanosecond lasers

When laser radiation is shined onto a metal's surface, the laser interacts with the electrons in the metal via inverse Bremsstrahlung scattering. The heated electrons couple with the lattice and raise the temperature locally. If the temperature exceeds the melting or boiling point of the material, the lattice is destroyed and material is ejected from the surface. If the attenuation of radiation is much slower than the electron relaxation time, we can describe the heating of the metal surface with a diffusion equation [136],

$$\mathrm{C}\frac{\partial T(z,t)}{\partial t} - \mathrm{k}\frac{\partial^2 \mathrm{T}(z,t)}{\partial z^2} = I(z,t). \tag{3.1}$$

Here, $I(z,t) = I_0(t)\,\mathrm{A}\exp(-\alpha z)$ is the laser radiation at depth z and time t that propagates within the material. Furthermore, $I_0(t)$ is the intensity of free space laser pulse input, A is the transmission of the metal surface, and α is the skin depth of the electromagnetic field in the material. In this

equation, the radiation impinges on the surface of the material ($z = 0$) and results in a temperature rise near the surface.

When the radiation is a pulsed laser, we set $I_0(t) \propto \exp(-t^2/{\tau_L}^2)$, where τ_L is the pulse width of the laser. For a sufficiently short pulse width, the temperature field can accumulate near the material surface to form a high temperature layer before there is enough time for the temperature to diffuse. Two competing factors determine the thickness of the high temperature layer on the surface, namely the heat diffusion length, $\sqrt{k\tau_L/C}$, and the skin depth of the laser within the metal, $1/\alpha$.

The energy density per unit mass within the surface is $I\ \tau_l/\rho l$, where $l = \max(\sqrt{k\tau_L/C}, 1/\alpha)$ is the thickness of the high temperature layer and ρ is the material density. In our system, the skin depth of the Nd:Yag laser radiation on stainless steel is expected to be ~2 nm, while the heat diffusion length is ~150 nm; the thickness of the high temperature layer is hence determined by heat diffusion. Ablation of material occurs when the energy density within this layer is higher than the enthalpy of evaporation, Ω. Therefore the threshold for the laser energy of ablation is

$$\frac{I\tau_L}{\rho l} > \Omega. \tag{3.2}$$

This simple model [137] explains the origins of the surface vaporization.

Now let us return to our original goal of delivering momentum to micro-particles. When ablation occurs at the surface of the material, the vaporized mass can eject at a ballistic speed of 10^4 to 10^5 m/s and the reaction force shall push the particle in the opposite direction of the momentum of the vaporized mass. In reality, the ablation process is a very complicated thermal dynamic possibility of using PLA as a reliable tool for exciting mechanical motion in micro-granular systems. To simplify this discussion, we estimate the momentum gained by a particle from the local ablation of its surface to be:

$$p_{gain} = m_{removed} v_{vapor} \propto \frac{I\tau_L}{\rho l \Omega} A_L \sqrt{\frac{T_{vapor}}{m}} \propto \frac{E_L}{\rho l \Omega} \sqrt{\frac{T_{vapor}}{m}} \propto \frac{E_L}{\rho \Omega} \sqrt{\frac{C}{k\tau_L}} \sqrt{\frac{T_{vapor}}{m}}, \tag{3.3}$$

where E_L and A_L are respectively the pulse energy and beam area of the laser. The above equation says that the momentum gained by the illuminated particle is affected by the thermal conductivity k of the material. Large thermal conductivity implies a fast heat removal from the surface layer into the

bulk material of the particle and reduces the amount of the vaporized surface materials. The momentum gained by the striker particle using PLA is proportional to the pulse energy of the laser. This is shown experimentally in the next section. It is worth mentioning that the momentum of the laser photons plays no role in this scenario.

3.2. Pulsed laser ablation on stainless steel micro-particles

In this section, we experimentally describe PLA effects on steel micro-particles in air. We placed a steel micro-particle on top of a v-shaped groove (see Fig. 2.3 above) and excited it with the laser. Figure 3.1 shows high-speed images obtained when a single particle positioned in the v-shaped groove is excited by the laser pulse. In this acquisition, the high-speed camera was operated at 1,000 fps with an exposure time of 990 µs. The first image was taken before the laser pulse was fired, and the second image (0 ms) was taken less than one microsecond after the laser pulse interacted with the particle. The presence of material ejected from the particle's surface is evident from the plume trailing the particle. Damage to the surface of the particle, which is identifiable by changes in the particle's surface texture, can be seen 1 ms after triggering the laser and then again after 8 ms. The disappearance and reappearance of the damaged surface indicates that the particle was rolling in the groove after being excited. These results indicate that PLA can excite mechanical motion of the micro-particles. Following this preliminary confirmation, we studied the fundamental mechanisms to control the momentum of the target particle and identified the essential controlling factors that influence this process.

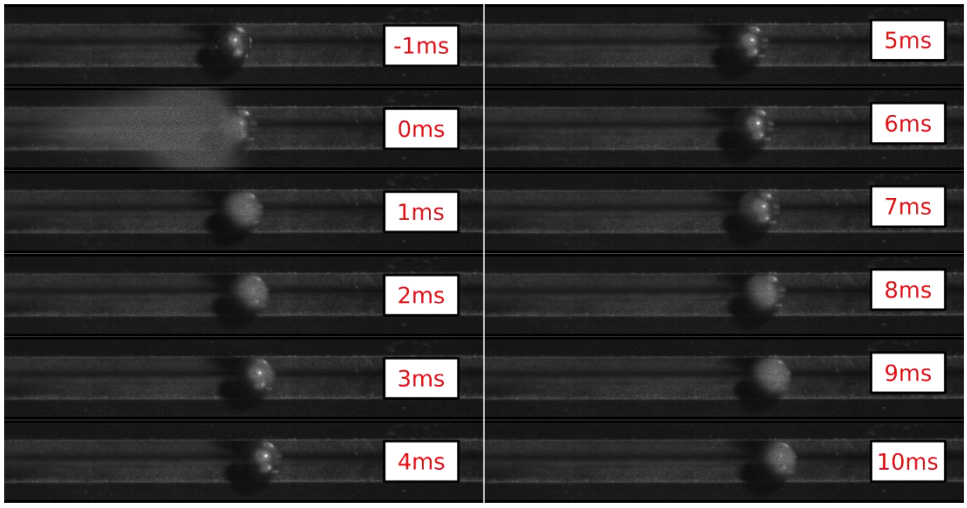

Figure 3.1: High-speed images of a micro-particle (114 µm radius, stainless steel 440c) on a v-shaped groove being illuminated by a pulsed laser at t=0 ms. Ejected materials can be seen at t=0 ms and

the damage on the particle's surface can be seen at t=1 ms and 9 ms. The sequential reappearance of the damaged surface indicates that the particle is rolling after being excited.

We performed experiments to determine the relation between the laser energy input and the momentum gained by the targeted particle. We placed target particles at a fixed location on top of the v-shaped groove and illuminated them with the pulsed laser, using pulse energy that varied between 0 to 0.8 mJ (Fig. 3.2a). The particle motion that resulted was recorded using the high-speed camera system. The speed of the particle was then obtained using image processing techniques, as described in detail in Chapter 2. The results obtained (Fig. 3.2b) show that the momentum transferred to the particles is proportional to the pulse energy, which agrees with the simple estimation derived in Eq. (3.3). We further compared the response of target micro-particles made with two different steel materials (stainless steel 316 and 440c) that do not have the same nominal thermal conductivity values. In Fig. 3.2b, it can be seen that the 316 particles gain almost twice the momentum that the 440c particles do, at the same laser energy input.

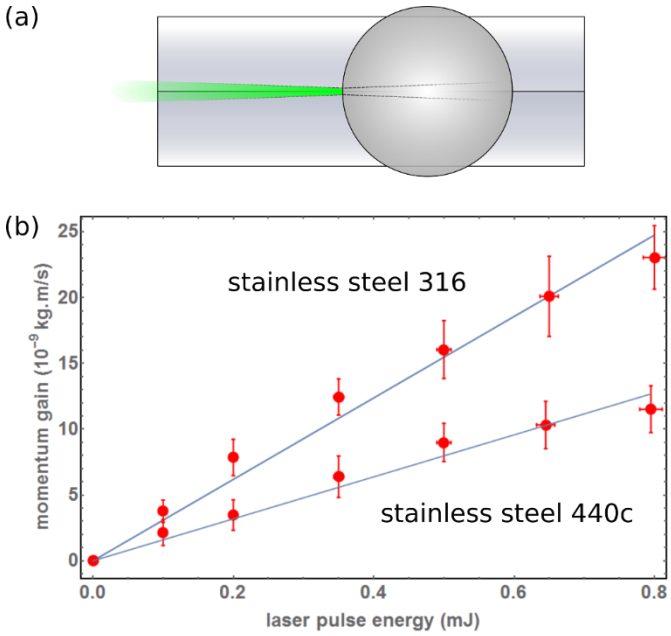

Figure 3.2: (a) Experimental scheme of calibrating the dependency of the transferred momentum to the laser pulse energy. (b) Momentum obtained by particles of two different materials (stainless steel 316 and 440c) at different laser inputs.

This difference in momentum gain indicates that the stainless steel 316 particles are more easily excited by laser ablation than the 440c particles. This result is not surprising; considering that stainless steel 316 has a smaller thermal conductivity (16.3 W/mK) than the 440c (24.2 W/mK), we expect the PLA efficiency to be higher in relation to stainless steel 440c (see the discussion in the previous section). However, experimental calibration is still required to ascertain if PLA excitation would be effective on particles of different materials, since an accurate theoretical estimation of the PLA efficiency remains difficult.

In the above experiments, when the striker particles were illuminated with the highest laser energy (0.8 mJ), the depth of the ablated mass was estimated to be ~150 nm using the data in [138]. This corresponds to only 0.01% of the mass of the test particles. As such, we considered the total mass of the excited particles as a constant. The total kinetic energy of the ejected mass and the particle was estimated to be 0.07 mJ; this is reasonable compared to the energy of the input laser pulse (0.8 mJ), if we consider that a large portion of laser is lost due to the reflection of metal surface.

3.2.1. Accuracy and repeatability

Before we can apply PLA as a tool of mechanical excitation in our micro-particles, we need to answer two main questions: (i) How repeatable is the PLA method for accelerating micro-particles?; and (ii) How accurately do we have to align the laser in order to obtain reproducible results? We conducted two tests to investigate the stability of a particle's excitation as a function of the laser's direction (Fig. 3.3a) and the position of the laser beam on the particle's surface (Fig. 3.3b). We first excited the particle with the laser beam intentionally shifted away from the center of the particle's mass by a distance x and measured the direction θ of the particle's displacement and velocity. Since the light wave front arrives simultaneously at every point of the illuminated area of the target particle (compared to the time scale of heat diffusion), we expect that the direction of the momentum gain does not depend on the direction of the beam, but only on the location of the laser beam on the surface of the particle. An offset of x should therefore lead to $\theta = \sin^{-1}(x/R)$, where R is the radius of the particle. We performed experiments to verify this assumption. We placed target particles on a clean, flat silicon wafer (instead of a groove) to allow them to move freely on a plane. Then we fixed the laser power to a specific value, to accelerate the particle to a velocity of 0.05 m/s (a relatively high speed at these scales was chosen in order to minimize the influence of the substrate's adhesion on the particle's motion). We used the micro-scope imaging system and the computer-controlled stage to locate the particles and aim the laser beam on their surfaces. In Fig. 3.3c, we plot the measured

particles' directions (red dots with error bars) and the theoretical predictions as obtained with $\theta = \sin^{-1}(x/R)$ (blue line). From the data we can see that when $x < 0.1R$, the maximum deviation is about 5°. We expect that an angular accuracy of 3° is possible when aiming the laser beam at the particles with a spatial accuracy of 10 μm (as in our experimental setup).

We performed experiments to determine the role of particle position with respect to the laser focal plane (Fig. 3.3b). The simpler estimation of the PLA efficiency in transferring momentum to target particles only depends on the laser energy. However, if the laser beam intensity diverges when it reaches the particle's surface, more energy is needed to raise the local temperature to the vaporization point. This effect is expected to lower the efficiency of the PLA process. We performed experiments to monitor variations of the target particle velocity as a function of its distance from the laser focal point. For these experiments, we used steel 440c particles positioned in a v-groove. To perform the experiments, we first used a micro-manipulator to position the target particles at the laser's focal point and then illuminated the particles and measured their velocity. We then repeated these measurements, using a computer-controlled sample stage to move the particle systematically away from the focal point by shifting its position along the reference axis (z). The results are shown in Fig. 3.3d. We can see that the momentum gain is quite stable when the laser beam is focused within $1R$ from the surface of the particles. This agrees well with our laser beam waist of 15 μm (the corresponding Rayleigh length is 1.3 mm).

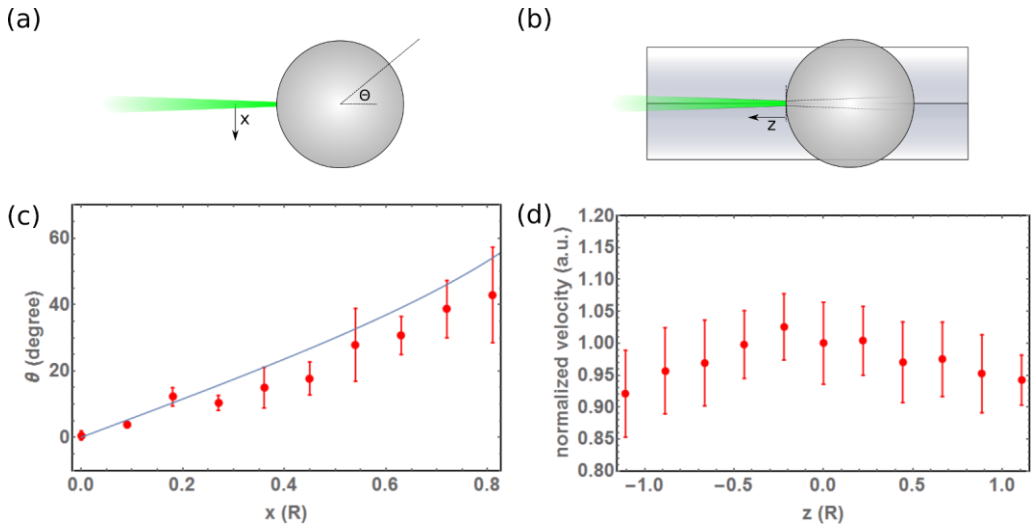

Figure 3.3: Repeatability of the laser ablation method to excite particles on a substrate. (a,b) Experimental diagrams. (a,c) Schematic diagram and results of the experiment measuring the angular dependency of the momentum to the off axis distance. (b,d)

Schematic diagram and results of the experiment measuring the accuracy requirement for particles along the optical axis of the laser. A 15% variation of output velocity is observed.

However, a closer examination of Figs. 3.2 and 3.3 reveals a velocity variation of ~15% in all data, which is a limitation of our experimental system. Such velocity variation can arise from imperfections in the stainless steel particles, from the energy stability of the laser (about 1% in our system), from the angular stability of the laser beam, or other systematic errors. We conclude that under realistic operation conditions, our laser system can deliver momentum to our stainless steel micro-particles with 15% accuracy in magnitude and 3% angular stability. In the next section, we investigate the laser energy transfer to silica colloids that are immersed in water, which are used in the dynamic testing of two-dimensional colloidal systems (as described in Chapter 6).

3.3. Pulsed laser ablation on silicon dioxide colloids

In this section, we describe the laser ablation process acting on micro-scale SiO_2 particles in fluid. As SiO_2 is a transparent dielectric material with a refractive index of 1.42, when the particles are immersed in water (refractive index of 1.33), a focused laser beam passing through the particles will be slightly diffracted by the spheres and not absorbed. In order to increase the efficiency of laser interaction, some particles are coated first with 5 nm of Cr as an adhesion layer and then with 50 nm of Au before being mixed with the uncoated particles. As the skin depth of our Nd:Yag laser beam on Au is 3 nm, we expect a very strong absorption of the laser beam in the gold layer.

We inject the coated and uncoated particles with DI water to the micro-fluidic cell. We focus the laser beam within the water on the particles, especially those that are coated. In Fig. 3.4abc, we show images of the excitation process of micro-particles in water that are taken at 45553 frames per second. The coated target particle, which is initially at rest on the micro-fluid cell, is marked by the white arrow. The laser radiation that results when we shine a laser pulse on this particle can be seen in the photo (Fig. 3.4b). After the particle is shot, we observe that the particle is relocated in the next frame and that the material ejected from the particle is left at the original location (as marked by a hollow arrow in Fig. 3.4c). This is because the high-speed camera does not directly resolve the velocity of the particle due to insufficient acquisition speed. To estimate the momentum gain of the particle at different laser power, we consider the particles are experiencing a Stokes' drag force in the background liquid, $f = -6\pi\mu Rv$, where μ is the viscosity of the liquid and R and v are respectively the radius and velocity of the particle. We can solve the relationship between the initial velocity of

the motion, v_0, and the final displacement using $\Delta x = v_0/6\pi\mu R$. By measuring the final displacement of micro-particles in a liquid with known viscosity, we can therefore calculate the initial velocity at a given laser energy. In our system, the laser beam is focused with an objective lens and expected to have a beam diameter of 10 μm. Since the laser spot is bigger than our micro-particles, the absorbed laser energy is estimated by the product of laser intensity and the area of particles.

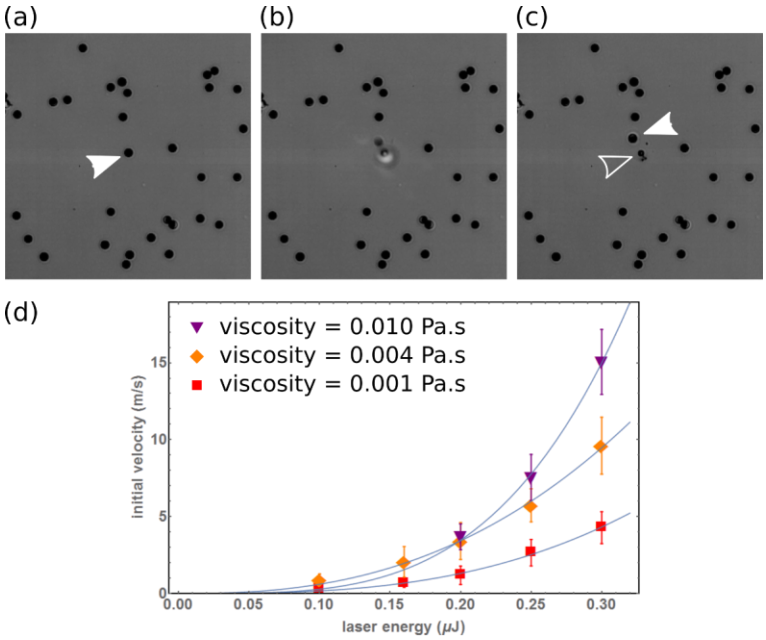

Figure 3.4: Excitation of micro-colloids' motion in water. We focus the laser on the micro-colloids in liquid. (a) The target particle (marked with a white arrow) before the laser is shone on it. (b) During the laser excitation, the laser radiation can be seen at the original position of the target particle. (c) The target particle is relocated to a new position (again marked with a white arrow). A residue of ejected dark metal flake is left at this particle's original position (marked by a hollow arrow). (d) The measured initial velocity at different laser energy and different viscosity of the background fluid.

We measure particle velocity gain due to the PLA process at varying laser energy and varying viscosity. To change the viscosity of the background fluid, we mix the water-glycerol ratio to adjust the dynamic viscosity of the background fluid from 0.001 to 0.01 Pl [139, 140]. The resultant velocity is shown in Fig. 3.4d. Here we also see the dependency of the particle velocity at different laser energy and the viscosity of background fluid, which interestingly suggests that a thicker background fluid can enhance the momentum that is gained through the PLA process. The higher the viscosity, the greater the velocity gain. We fit these data with power law $v \propto E^n$ and obtain n equals to 2.23, 2.10,

and 5.83 for dynamic viscosity equals to 0.001, 0.004, 0.01 Pl, respectively. This behavior deviates from the prediction given by Eq. (3.3), which indicates that the working principle of this wet particle excitation is very different from that of the dry particle case. The efficiency of this process (i.e., the ratio between the kinetic energy that is obtained by the micro-particle and the laser pulse energy) is about 0.001%, which is significantly lower than the efficiency in dry particle cases. With this calibration results, we can predict the momentum gain of the target particle at controlled laser energy in the background fluid that was tested.

Finally, it should be clearly stated that the particle manipulation we performed in this section is unrelated to optical tweezing [141, 142], which is a technique for manipulating micro-particles in liquid. The optical tweezer manipulates micro-particles by creating an attractive potential well to the electric dipole of the target particles by properly tuning the laser intensity and frequency. However, the process is four orders of magnitude weaker than laser ablation in our system and is omitted throughout our discussion.

3.4. Summary

In this chapter we investigated the use of pulse laser ablation as a tool for mechanically exciting dry (stainless steel particles of a radius 150 μm) and wet (SiO_2 colloids with a radius of 3.69 μm) micro-particles. For the dry particles, we measured variations of the magnitude and direction of the momentum gain as a function of the laser position and alignment. We showed that our system can deliver momentum to target stainless steel micro-particles with 15% accuracy in magnitude and 3% angular stability under realistic operation conditions. For the wet particles, we measured the velocity gains of micro-particles in fluid due to PLA at varying laser energy and at varying viscosity. The velocity gains are shown to be dependent on the viscosity of the background fluid, which indicates the interplay of the hydrodynamic system within the PLA process.

We obtained the calibration relationship between the laser energy and the momentum gained during the PLA process for both the dry and wet particles. The ability to predict the magnitude and direction of the delivered momentum is especially useful in our experiments, where direct measurements of the applied stress by direct physical contact are difficult to obtain. The laser system can deliver fast, repeatable, and automatic mechanical excitations to any point of the system that can be reached by the laser radiation. The non-contact nature of the PLA excitation system makes our experimental

apparatus also ideal for testing different micro-particle types and geometries, because the assembly and excitation of the system constitute independent parts of the setup.

Chapter 4

Micro-particles in One-dimensional Confinement

In the previous chapter, we described the phenomena that are associated with using pulsed laser ablation as a tool to mechanically excite spherical, metallic micro-particles. This approach provides the basis for transferring a controlled momentum to a system of micro-particles. However, before we proceed to study the wave propagation in micro-granular systems, we need to know how the particles behave on the substrate (i.e., we need to identify the governing equations of motion). The basic motion of a macroscopic sphere on a support structure has been studied earlier, for example in [143, 144]. In the simplest models, a sphere moving in one direction is considered as a rigid body and is subjected to Coulomb friction that acts between the surface of the sphere and the supporting structure [4]. However, the complexity of the models increases significantly if the spheres are no longer assumed as rigid bodies, and if the elastic contact force, the hysteretic losses in rolling [145], the lubricated sliding friction, the deformation of the surfaces, and the shear adhesive force are also included [145]. For example, for particles moving in an asymmetric v-shaped groove, governed by gravitation and static friction, the uneven shear force exerted on the spheres by both walls can cause the spheres to rotate. As a result, models that describe the particles' motion must account for such rotation.

In most studies of macroscopic granular systems, for example [125], the granular chains are considered as a classical system of spheres moving on a guiding rail, where only the elastic contact forces between particles are included. In these cases, the interactions between particles and their supports are usually considered negligible or are only seen as contributing to dissipation in the system.

It is questionable whether the description of macro-granular systems still applies to the micro-granular system of interest for this thesis. In the rest of this chapter, we analyze the relevant types of interactions that arise when particle size is reduced. The next chapter builds on these findings, to analyze the dynamic response of a multi-particle chain and verify if the same phenomena found in macroscopic particles (e.g., solitary wave propagation) are also present at the micro-scale.

It is well known that when particle size is reduced to the micro-scale, adhesive forces such as hydrodynamic and Van der Waals interactions become more dominant [34, 103, 146]. The particles considered in our dry systems have diameters of ~300 μm, which are much larger than the diameters of 1 to 10 μm that are usually assumed in the DMT and JKR models; however, they are also not properly "macro-scale." No theoretical approaches are available to describe these contact regimes. However, this intermediate size range indicates that the modeling of the system should be modified to account for the presence of the support system and air drag in the system's dynamics.

A complete first-principle model of the dynamics of micro-particles is difficult, as not enough information is available about these particles' physical characteristics. In this chapter, we address this issue by extracting experimental parameters from the study of the motion of individual particles on their substrate (in this case a v-shaped groove). We also derive an empirical model to describe the observed particle motion. We extract the dissipation terms, including Coulomb friction, Stokes' viscous drag force, and quadratic drag force, and analyze the trajectories of the particles moving in the groove. In addition, we also study the interaction between two particles by extracting from experiments the coefficient of restitution upon impact and the frictional constant between two particles. The goal of our initial set of experiments is to construct an empirical description of the dynamical system that can pave the way for a complete study of wave propagation in micro-granular chains and that can serve as the foundation for the analysis that is presented in the next chapters. With the experiments described in this chapter, however, it is not possible to study either the particle contact interaction potential or specific interaction/adhesion between the particles and their support in detail.

4.1. Modeling the motion of a sphere in a groove

In this section, we model the rolling and sliding motion of a spherical particle in a groove. Let the particle have a radius R, mass m, and moment of inertia I. Frictional forces between a particle and the surface of a groove are proportional to the normal force between the contact with a proportional constant, μ_{pg}. The inclined angle between the two surfaces of the v-shaped groove is θ, where $\theta = 70.6°$ in our system.

Let the v-grooves lie in the x-z plane, with its long axis (i.e., the direction of motion of the particle) parallel to the z-direction (Fig. 4.1). Assuming the particles do not move in the x- and y-directions, we can describe the motion of the particles with four parameters, namely z, v_z, θ_x, and ω_x, where z is the z-component of the particle displacement, v_z is the velocity in the z-direction, θ_x is the x-

component of the particle angular displacement, and ω_x is the x-component of the angular velocity. If there is a relative motion between the surface of the particles and the groove (i.e., $v_z - R\omega_x \sin(\frac{\theta}{2}) \neq 0$), the total force and torque resulting from the frictional forces between the particles and the two surfaces of the v-groove are respectively $f_z = -mg\mu_{pg}/\sin(\frac{\theta}{2})$ and $\tau_x = Rmg\mu_{pg}$. For convenience, we define $v_a \equiv R\omega_x$, and $s \equiv \sin(\frac{\theta}{2})$ as a geometric factor that depends on the inclined angle of the groove. In our system s is 0.5779.

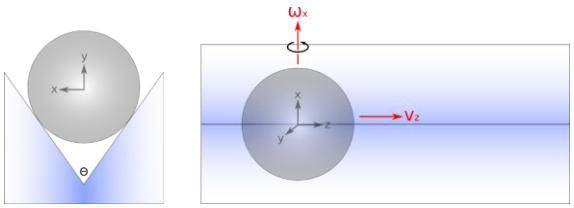

Figure 4.1: A particle in a v-shaped groove. The direction in which the particle is moving is defined as the z-direction. The particle is supported by the groove's two inclined surfaces. In comparison to when particles are placed on a flat surface, the geometry of the v-groove enhances the frictional force by a factor of $1/\sin(\theta/2)$, where θ is the angle between the two surfaces of the v-groove. For the particles to roll without sliding on the groove, the groove's translational and angular velocities need to satisfy $v_z = R\omega_x \sin(\frac{\theta}{2})$.

We can see that when a particle is moving on the groove, the frictional force transfers energy between translational and angular motion until no relative motion occurs between the surfaces in contact:

$$v_z = sv_a. \tag{4.1}$$

When $v_z \neq sv_a$, the equations of motion become

$$\begin{aligned} \frac{d}{dt} v_z &= -sign(v_z - sv_a) g\mu_{pg}/s, \\ \frac{d}{dt} v_a &= sign(v_z - sv_a) kg\mu_{pg}, \end{aligned} \tag{4.2}$$

where $sign(x)$ is the signum function with $sign(0) = 0$. For a particle moving in a groove, the Coulomb friction causes the particle to reach a steady state of rolling without sliding. If the system evolves from an initial state of ${v_y}^{(0)}$ and ${v_a}^{(0)}$ to a final steady state of ${v_y}^{(1)}$ and ${v_a}^{(1)}$, the steady state velocities (defined as the velocity of the particles that are rolling without sliding) are

$$v_z^{(1)} = \frac{ks^2}{ks^2+1} v_z^{(0)} + \frac{s}{ks^2+1} v_a^{(0)},$$
$$v_a^{(1)} = \frac{ks}{ks^2+1} v_z^{(0)} + \frac{1}{ks^2+1} v_a^{(0)}. \quad (4.3)$$

Starting at the initial velocities of $v_z^{(0)}$ and $v_a^{(0)}$, the distance (Δz) and time (Δt) required to achieve steady states are, respectively,

$$\Delta z = \frac{1}{2} \frac{s}{ks^2+1} \frac{v_z^{(0)} - s v_a^{(0)}}{g\mu_{pg}} \left(\frac{2ks^2+1}{ks^2+1} v_z^{(0)} + \frac{s}{ks^2+1} v_a^{(0)} \right)$$
$$\Delta t = \frac{s}{ks^2+1} \frac{v_z^{(0)} - s v_a^{(0)}}{g\mu_{pg}}. \quad (4.4)$$

This means that the rolling-sliding to rolling transition happens at a time scale of $\frac{s}{ks^2+1} \frac{v_z^{(0)}}{g\mu_{pg}}$, which is in the order of a few milliseconds in our system. For a more realistic model of all of the physical forces that are involved in the experimental system, we include the time constant for air friction, T, which is another empirical parameter,

$$\frac{d}{dt} v_z = -sign(v_z - s v_a) g\mu_{pg}/s - v_z/T,$$
$$\frac{d}{dt} v_a = sign(v_z - s v_a) kg\mu_{pg}. \quad (4.5)$$

Notice that we have two dependent variables (namely v_z and v_a) that should be investigated: we will retrieve the information for v_a through indirect fitting of the experimental data.

4.2. Motion of one micro-particle in a groove

We first study the motion of a single micro-particle that is rolling in a v-shaped groove (Fig. 4.1). A micro-particle is placed in the groove and excited with the laser system (see Chapter 3) to different controlled velocities between 0 to 0.1 m/s. The particle is positioned in the groove with a computer-controlled micro-manipulator, in order to achieve accurate and repeatable initial conditions. We track the motion of a micro-particle with the optical high-speed imaging system that is described in Chapter 2. In Fig. 4.2b, we show a typical measured trajectory for a micro-particle that is moving in the groove. The particle has an initial velocity of 0.025 m/s, and from the trajectory it is evident that its motion is characterized by two different regimes: i) a rolling and sliding regime; and ii) a rolling without sliding regime (which are labeled with green and red lines, respectively). The transition time between these

two different motion regimes, t_1, as well as μ_{pg}, T, and the initial velocity v_0 are found by fitting the experimental data numerically. The fitting parameters are obtained by minimizing the error function $\mathrm{Er}(\mu_{pg}, \mathrm{T}) = \sum_n (f(t_n; v_{\mathrm{z0}}, \mu_{pg}, \mathrm{T}) - x_n)^2$, where $f(t; v_{\mathrm{z0}}, \mu_{pg}, \mathrm{T})$ is the solution of Eq. (4.5),

$$f(t; \mu_{pg}, \mathrm{T}) = \begin{cases} T\left(v_{\mathrm{z0}} - \frac{gt\mu_{\mathrm{pg}}}{s} + \frac{gT\mu_{\mathrm{pg}}}{s}\right) - \mathrm{e}^{-\frac{t}{T}} T\left(v_{\mathrm{z0}} + \frac{gT\mu_{\mathrm{pg}}}{s}\right), \text{if } t < t_1 \\ \mathrm{e}^{-\frac{t}{T}}(sv_{\mathrm{z0}} + gT\mu_{\mathrm{pg}} - \mathrm{e}^{\frac{t_1}{T}} gT\mu_{\mathrm{pg}})/s, otherwise \end{cases}, \tag{4.6}$$

where it is assumed the initial angular velocity is zero and t_1 is the solution of $gkst\mu_{\mathrm{pg}} + \mathrm{e}^{-\frac{t}{T}}(-sv_{\mathrm{z0}} - gT\mu_{\mathrm{pg}} + \mathrm{e}^{t/T} gT\mu_{\mathrm{pg}})/s = 0$. In Figs. 4.2c-d, we plot the T and μ_{pg} which are obtained through numerical fitting. It can be seen in Fig. 4.2c that the empirical parameter of the time constant for air friction, T, is not a constant but instead has a linear dependency on the initial velocity. The two clouds of the measured value of T obtained from the two types of particles (stainless steel 440C and stainless steel 316) overlap to give $T = T_0 + T'v_0 = 0.052 + 1.10v_0$. For comparison, the predicted time constant caused by the Stokes' drag in air is $T = \mathrm{m}/6\pi\mu\mathrm{R} = 0.074$. The agreement between data from particles of different materials that are the same size shows that the measured time constant is a geometric effect that is only altered by the particles' shapes and dimensions. The linear behavior of T implies that the air friction should include another correcting term that is proportional to the square of velocity:

$$\frac{v_z}{T} = \frac{v_z}{T_0 + T'v_0} \sim \frac{v_z}{T_0} - \frac{T'}{T_0}\frac{{v_z}^2}{T_0} \equiv \frac{v_z}{T_0} - \frac{{v_z}^2}{L}, \tag{4.7}$$

where v_z is the particle velocity, T is the original proposed time constant for dissipation, and T_0 and L are empirical parameters that provide a more accurate representation of dissipation.

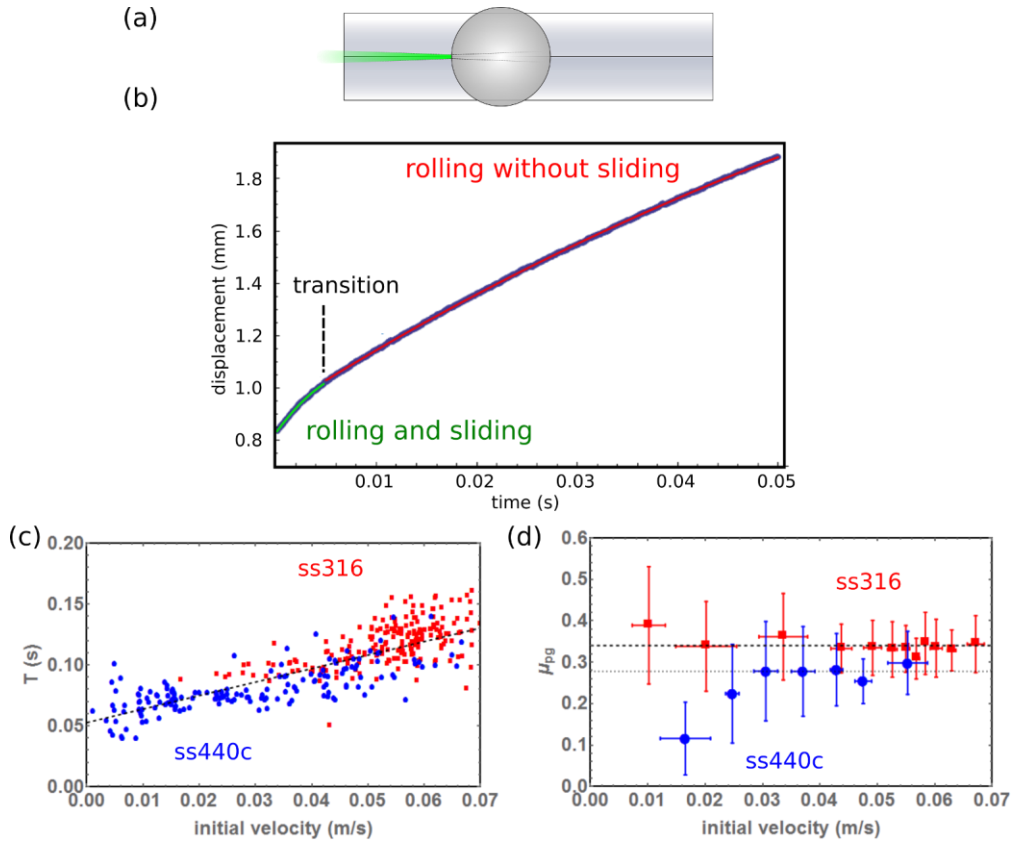

Figure 4.2: Experimental investigation of single micro-particles moving in a groove. (a) Schematic diagram of the experimental setup: a laser (green beam in the diagram) excites a particle in a groove, with a controlled pulse energy. We tested two types of micro-particles, stainless steel 316 and 440c. (b) A typical measured trajectory of an excited micro-particle. The transition from a rolling and sliding motion to rolling without sliding can be found by using an optimization algorithm to obtain the empirical parameters T and μ_{pg}, as a function of initial velocity. (c) T is found to depend linearly on the initial velocity $T = 0.052 + 1.10v_0$. (d) Stainless steel 316 particles have a mean of $\mu_{pg} = 0.337$ (dashed line) and stainless steel 440c particles have a mean of $\mu_{pg} = 0.296$ (dotted line) for $v_0 > 0.03\ m/s$. The error bars are plotted with $\pm\sigma/2$, where σ is the standard deviation of the measurement.

The average friction constant, μ_{pg}, is 0.337 for stainless steel 316 and 0.293 for stainless steel 440c particles. It can be seen that the friction coefficient for stainless steel 440c particles approaches zero at low velocity. This can result from the fact that particles made of steel 440c have much smoother surfaces and a higher quality than the steel 316 particles. The complete equations of motion for particles moving in a groove are

$$\frac{d}{dt}v_z = -\frac{sign(v_z - sv_a)g\mu_{pg}}{s} - \left(\frac{v_z}{T_0} - \frac{{v_z}^2}{L}\right),$$
$$\frac{d}{dt}v_a = sign(v_z - sv_a)kg\mu_{pg}, \tag{4.8}$$

where $T_0 = 0.052\ s$, $L = 2.5\ mm$, and $\mu = 0.337$ and 0.293 for stainless steel 316 and 440c, respectively.

4.3. Modeling the collision of two particles in a groove

With the equations obtained in the previous section, we can move on to modeling the collision of two particles in a groove. In an ideal scenario, when two particles of the same mass collide elastically, e.g., $z_2 - z_1 < 2R$, they exchange their velocity. Assuming their initial velocities are ${v_{z1}}^{(1)}$ and ${v_{z2}}^{(1)}$, after an elastic collision their velocities are expected to become ${v_{z1}}^{(2)} = {v_{z2}}^{(1)}$ and ${v_{z2}}^{(2)} = {v_{z1}}^{(1)}$. However, the real contact interaction between the particles is affected by the presence of a frictional force between their surfaces. If a relative sliding motion occurs between the surfaces of the two particles (i.e., $v_{a1} + v_{a2} \neq 0$), then the presence of a frictional force induces a torque at the contact and changes the angular momentum of both particles. Let μ_{pp} be the frictional constant between the surfaces of two particles; when $v_{a1} + v_{a2} > 0$, we have

$$-\Delta v_{z1} = \int \frac{f}{m}dt = -\int \frac{\tau_{x1}}{m\mu_{pp}R}dt = -\frac{I\Delta\omega_{x1}}{m\mu_{pp}R} = -\frac{I\Delta v_{a1}}{m\mu_{pp}R^2}. \tag{4.9}$$

Here, Δv_z and $\Delta\omega_x$ are respectively the changes in translational and angular velocity before and after the collision. In addition, f is the contact force during the impact, τ_x is the torque resulted from the frictional force, and R, m, and I are the radius, mass, and inertia of moment of the particle, respectively. We therefore have $\Delta v_{a1} = \mu_{pp}k\Delta v_{y1}$ and similarily, $\Delta v_{a2} = -\mu_{pp}k\Delta v_{y2}$, and the resulted angular ${v_{a1}}^{(2)} = R{\omega_{x1}}^{(2)}$,

$${v_{a1}}^{(2)} = {v_{a1}}^{(1)} + sign\left({v_{a1}}^{(1)} + {v_{a2}}^{(1)}\right)\mu_{pp}k\left({v_{z2}}^{(1)} - {v_{z1}}^{(1)}\right),$$
$${v_{a2}}^{(2)} = {v_{a2}}^{(1)} + sign({v_{a1}}^{(1)} + {v_{a2}}^{(1)})\mu_{pp}k({v_{z2}}^{(1)} - {v_{z1}}^{(1)}). \tag{4.10}$$

Equation (4.10) holds only when the sliding motion between the particle surfaces is not eliminated by the frictional force between the particles before the end of the impact. If the frictional force eliminates the relative motion between the surfaces during the impact, the frictional force would cease

to contribute to the change of angular velocities. In this case, we can solve the final states of angular velocities,

$$\omega_{x1}{}^{(2)} + \omega_{x2}{}^{(2)} = \frac{v_{a1}{}^{(2)}}{R} + \frac{v_{a2}{}^{(2)}}{R} = \frac{(v_{a1}{}^{(1)} + \Delta v_{a1})}{R} + \frac{(v_{a2}{}^{(1)} + \Delta v_{a2})}{R} = 0, \tag{4.11}$$

and obtain

$$\begin{aligned} v_{a1}{}^{(2)} &= (v_{a1}{}^{(1)} - v_{a2}{}^{(1)})/2, \\ v_{a2}{}^{(2)} &= (v_{a2}{}^{(1)} - v_{a1}{}^{(1)})/2. \end{aligned} \tag{4.12}$$

For the relative motion between the surfaces to be eliminated by frictional force during the impact, we require the magnitude of change in angular velocity $|\Delta v_a|$ in Eq. (4.12) to be smaller than the one in Eq. (4.10), which translates into

$$\left|v_{a1}{}^{(1)} + v_{a2}{}^{(1)}\right| < 2\mu_{pp}k(v_{z1}{}^{(1)} - v_{z2}{}^{(1)}). \tag{4.13}$$

By checking the inequality, we can determine which case applies to the collision.

Let us consider the specific collision in which the two colliding particles are rolling without sliding. The first particle, which starts with the initial velocities of $v_{z1}{}^{(0)} = u_1{}^{(0)}$ and $v_{a1}{}^{(0)} = u_1{}^{(0)}/s$, moves toward the second particle, which has velocities of $v_{z2}{}^{(0)} = u_2{}^{(0)}$ and $v_{a2}{}^{(0)} = u_2{}^{(0)}/s$. Depending on the values of $u_1{}^{(0)}$ and $u_2{}^{(0)}$, either Eq. (4.10) or (4.12) can be used to determine the resultant states after the instance of collision. If Eq. (4.13) holds, right after collisions we have

$$\begin{aligned} v_{z1}{}^{(1)} &= u_2{}^{(0)}, \\ v_{z2}{}^{(1)} &= u_1{}^{(0)}, \\ v_{a1}{}^{(1)} &= \left(\frac{1}{s} - \mu_{pp}k\right)u_1{}^{(0)} + \mu_{pp}k u_2{}^{(0)}, \\ v_{a2}{}^{(1)} &= \left(-\mu_{pp}k\right)u_1{}^{(0)} + \left(\frac{1}{s} + \mu_{pp}k\right)u_2{}^{(0)}. \end{aligned} \tag{4.14}$$

After the system evolves into steady state motions, we have

$$v_{z1}{}^{(2)} = \frac{1}{ks^2+1}\left(1 - s\mu_{pp}k\right)u_1{}^{(0)} + \frac{1}{ks^2+1}(ks^2 + s\mu_{pp}k)u_1{}^{(0)}, \tag{4.15}$$

$$v_{z2}{}^{(2)} = \frac{1}{ks^2+1}\left(ks^2 - s\mu_{pp}k\right)u_1{}^{(0)} + \frac{1}{ks^2+1}(1 + s\mu_{pp}k)u_1{}^{(0)},$$

$$v_{a1}{}^{(2)} = v_{z1}{}^{(2)}/s,$$

$$v_{a2}{}^{(2)} = v_{z2}{}^{(2)}/s.$$

If Eq. (4.9) does not hold, the relative surface motion between the particles is zero when the two particles are in contact. Right after the collision, we have

$$\begin{aligned} v_{z1}{}^{(1)} &= u_2{}^{(0)} \\ v_{z2}{}^{(1)} &= u_1{}^{(0)} \\ v_{a1}{}^{(1)} &= \frac{1}{2s}u_1{}^{(0)} - \frac{1}{2s}u_2{}^{(0)} \\ v_{a2}{}^{(1)} &= -\frac{1}{2s}u_1{}^{(0)} + \frac{1}{2s}u_2{}^{(0)} \end{aligned} \tag{4.16}$$

After the system evolves into steady state motions, we have

$$\begin{aligned} v_{z1}{}^{(2)} &= \frac{1}{ks^2+1}(1/2)u_1{}^{(0)} + \frac{1}{ks^2+1}(ks^2 - 1/2)u_1{}^{(0)} \\ v_{z2}{}^{(2)} &= \frac{1}{ks^2+1}(ks^2 - 1/2)u_1{}^{(0)} + \frac{1}{ks^2+1}(1/2)u_1{}^{(0)} \\ v_{a1}{}^{(2)} &= v_{z1}{}^{(2)}/s \\ v_{a2}{}^{(2)} &= v_{z2}{}^{(2)}/s \end{aligned} \tag{4.17}$$

The physical meaning of the above derivation is simple: during the collision, the two particles exchange momentum and apply a reciprocal torque, which changes angular momentum; after the collision, the particles accelerate if the translational and angular velocities are mismatched. In both cases, we have $v_{z1}{}^{(2)} - v_{z2}{}^{(2)} = \frac{1-ks^2}{1+ks^2}(v_{z1}{}^{(0)} - v_{z2}{}^{(0)})$, which means that the collision and reacceleration process scale the inter-particle velocity by a factor of $\frac{1-ks^2}{1+ks^2}$. If

$$0 < \frac{1-ks^2}{1+ks^2} < 1, \tag{4.18}$$

n secondary collisions after the first impact will occur (with *n* going to infinity) because ${v_{z1}}^{(2n)} - {v_{z2}}^{(2n)} > 0$. For solid spherical particles ($k = 5/2$) on a flat planar surface ($s = 1$), only one collision (i.e., the first impact), is expected to occur. For particles in a v-groove, the condition in Eq. (4.18) implies $\theta < 78.5°$, which is satisfied for the specific v-shaped groove that we experimentally fabricated.

In the beginning of the above derivation, we assumed completely elastic collisions between particles. The derivation can be easily generalized to include the case of inelastic collisions, and the prediction of multiple secondary collisions remains valid. For example, if the collision is perfectly inelastic such that both particles obtain the same translational velocity after collision, ${v_{z1}}^{(1)} = {v_{z2}}^{(1)}$, it follows that ${v_{a1}}^{(1)} > {v_{a2}}^{(1)}$ due to the torque exerted by frictional forces. After the system evolves into steady state, from Eq. (4.3) we have ${v_{z1}}^{(2)} - {v_{z2}}^{(2)} = \frac{s}{ks^2+1}({v_{a1}}^{(1)} - {v_{a2}}^{(1)}) > 0$, which guarantees another upcoming collision. We can generalize the above derivation for particle-groove systems by adding dissipation that is linearly proportional to the particle velocity. Since the dissipation only scales linearly with the velocity, with a factor of $\exp\left(-\frac{\Delta t}{T}\right)$, where Δt is the time difference and T is the time constant of the dissipation, the system results in a positive final velocity difference:

$$ {v_{z1}}^{(2)} - {v_{z2}}^{(2)} = \frac{1-ks^2}{1+ks^2}\left({v_{z1}}^{(0)} - {v_{z2}}^{(0)}\right)\exp\left(-\frac{\Delta t}{T}\right) > 0. \tag{4.19} $$

In this case, secondary collisions are also expected.

Notice that the criterion of Eq. (4.18) does not depend on the frictional constants of μ_{pp} and μ_{pb}. This means that the number of expected collisions is independent of the particles' material properties. The presence of multiple secondary collisions can occur in a very large number of systems despite the specific value of Coulomb friction. Such collisions constitute a very universal behavior among various particle-groove systems, including the micro-granular system that we fabricated. In our experimental system, $\frac{1-ks^2}{1+ks^2} = 0.09$, and after each collision and reacceleration process the velocity difference, $\left({v_{z1}}^{(2n+2)} - {v_{z2}}^{(2n+2)}\right) = 0.09\left({v_{z1}}^{(2n)} - {v_{z2}}^{(2n)}\right)$ scales to 9% of its original value. Due to the limited length of the fabricated grooves and limited spatial resolution of the imaging system, the presence of the secondary collisions cannot be resolved in our experiments. However, since the micro-particles are expected to collide multiple times, while they simultaneously lose kinetic

energy via Coulomb friction or other dissipation channels, we can argue that the two particles should end up rolling very close to each other, with $z_2 - z_1 \sim 2R$; this is indeed what we see in the next section.

4.4. Collisions between two particles in a groove

In this section, we experimentally investigate the collisions of two micro-particles in a v-shaped groove and extract the coefficient of restitution for each impact and the frictional constant between the two micro-particles from the measurements (Fig. 4.3). The first micro-particle, which acts as a striker, is positioned in the groove and excited with the laser pulse to reach a maximum velocity of 0.3 m/s before colliding with a stationary micro-particle (i.e., the target particle). Both particles are positioned by a computer-controlled micro-manipulator that has a location accuracy of ~1 μm. We studied two different types of collisions (Fig. 4.2a): (1) collisions that occurred when the striker gained enough angular velocity to roll without sliding before impacting the target particle, and (2) collisions between two micro-particles that are initially positioned in physical contact with each other. In Fig. 4.3b we show a photograph of two micro-particles in a typical experimental run for the first case study. Typical trajectories of micro-particles moving in the groove are shown for the same case in Fig. 4.3c, with the blue line representing the trajectory of the striker particle and the red line that of the target particle. It can be seen that after the collision, the striker particle accelerates due to the Coulomb frictional force. This results from a gain of angular momentum during collision and $v_z - sv_a < 0$ such that the Coulomb frictional force on the striker is in the positive z direction. The striker particle quickly catches up with the second particle after the collision, and the two particles keep a distance close to two times their radius, which is what we expected for two particles that are undergoing multiple secondary collisions (see section 4.3 above).

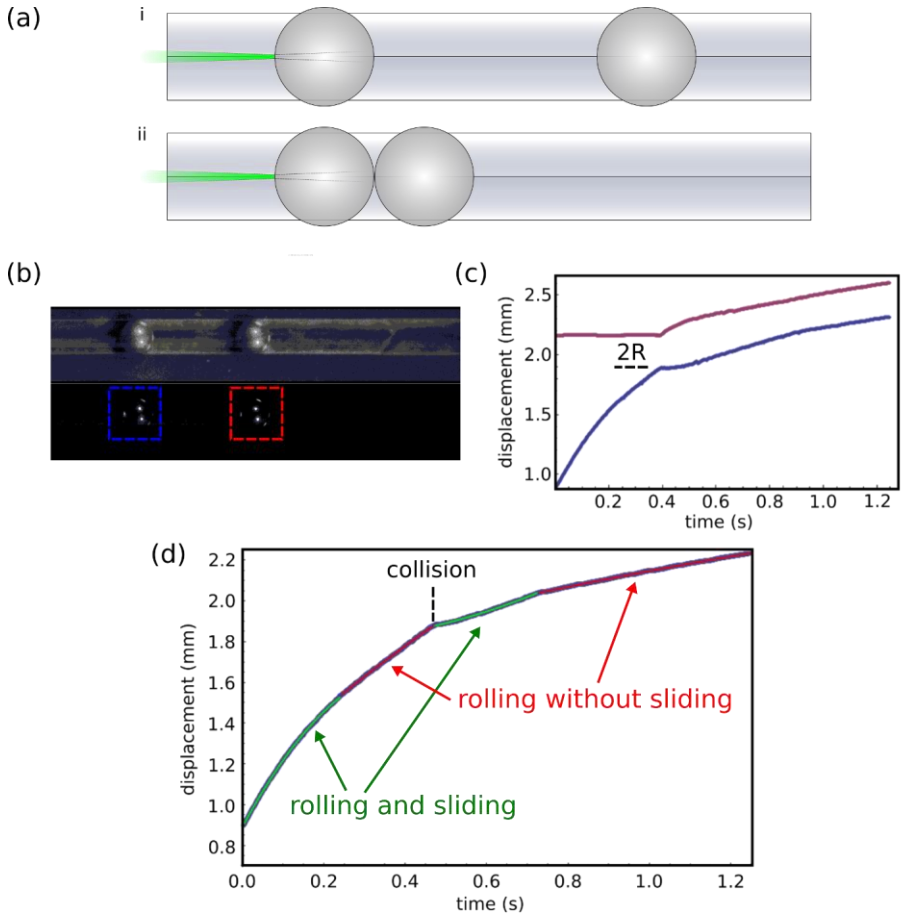

Figure 4.3: Experiments involving particle collisions in a groove. (a) Experimental schematics. Two cases of collisions are tested: a particle collides with another particle that is i) separated by 1 mm, or ii) in direct contact with it. (b) Digital image of the particles during the experiments. The blue and red dashed boxes identify the striker and the target particles, respectively. (c) Trajectories of the two colliding particles. (d) Rolling and sliding motion and rolling without sliding motion as identified for the striker particle. This trajectory reveals information on the angular motion of the particle.

In Fig. 4.3d, we plot the trajectory of the striker particle throughout the collision. The collision point can be clearly identified by the abrupt change in velocity. The particles undergo four ranges of motion, namely rolling and sliding before and after collision (green curves) and rolling without sliding before and after collision (red curves).

We examine the relation of tangential and normal forces between two particles. Throughout this chapter, we have assumed that the tangential force between two particles is well described by Coulomb friction and is linearly proportional to the inter-particle contact force. This is the foundation

of all of our derivations about particle collisions; however, is not true in general [147]. To justify whether it is valid for our system, we examine the ratio between the changes in translational and angular velocities that are caused by collisions.

In order to extract information (i.e., translational and angular velocities) about the particles' motions before and after the collision from the experimental data, we manually separate the trajectory before and after the collision and fit them with the solutions of Eq. (4.5). This allows us to obtain the initial values of v_{z} and v_{a} and to calculate the values of v_{z} and v_{a} near the collision. We plot the relation between the change of linear and angular momenta of the target particle (stainless steel 440c) in Fig. 4.4a. We can see that the change of momenta has a linear relationship. Fitting this linear relationship with Eq. (4.9), we obtain the frictional constant between two spheres, μ_{pp}, which is equal to 1.4. Despite the large variation in the resulting velocity after collision, the data indicates a linear relationship between inter-particle normal and tangential forces; from an experimental point of view, this can be used to describe our micro-particle system in general.

We are also interested in extracting the coefficient of restitution in the collisions, which is defined as

$$C = \frac{{v_{\mathrm{z2}}}^{(1)} - {v_{\mathrm{z1}}}^{(1)}}{{v_{\mathrm{z1}}}^{(1)} - {v_{\mathrm{z2}}}^{(1)}}, \tag{4.20}$$

This coefficient, which represents the ratio of relative velocities between the two particles before and after collision, is a measure of the efficiency of the collision process. The higher the coefficient of restitution, the more elastic the collision. We plot the experimental coefficients of restitution obtained for the stainless steel micro-particles as a function of the impact velocities in Fig. 4.4b-c; the red squares represent 316, the blue circles 440c. The variations in the values of the experimental coefficient of restitution obtained in our tests are large. Those obtained with stainless steel 316 particles are much larger than those obtained with stainless steel 440c particles, which can be explained by the much rougher surface of the 316 particles (see Chapter 2). Despite the big variation in the measured data, the results show that the coefficient of restitution has velocity dependence and, for both particle types, the coefficient of restitution approaches unity at lower speeds, which means that lower speed collisions are less lossy.

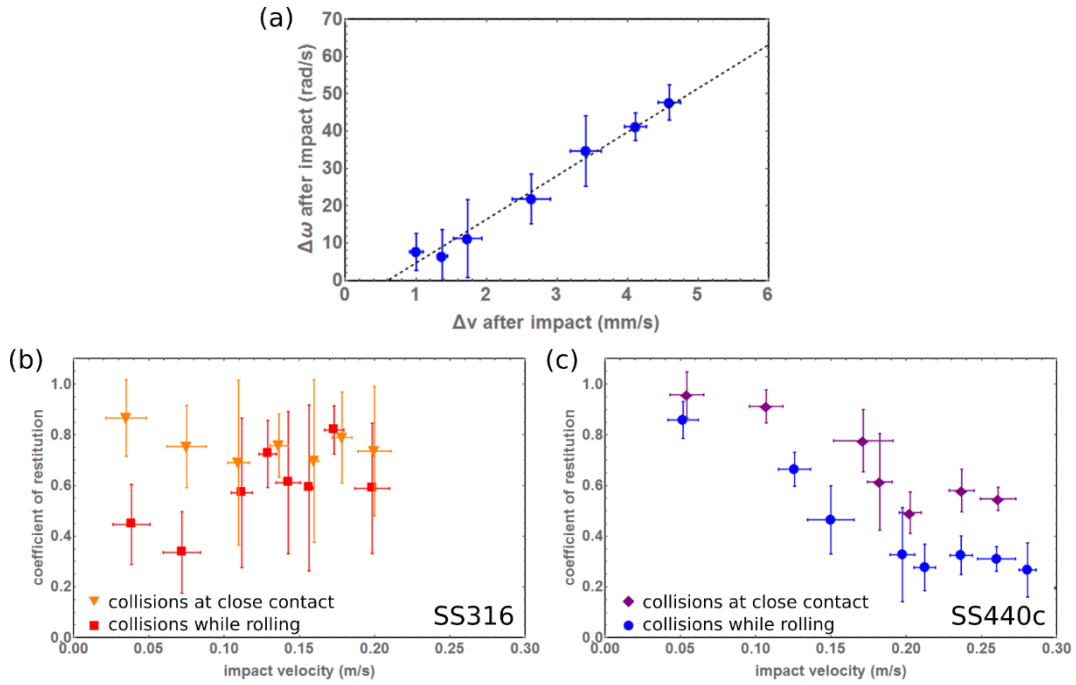

Figure 4.4: Experimental results for the collisions of two particles. (a) A linear correlation between the change of translational and angular velocities during collisions of two 440c particles is observed. The error bars are plotted with $\pm\sigma/2$, where σ is the standard deviation of the measurement. Fitting shows the normal force and tangential force can be described with Coulomb friction with a frictional constant of 1.4 (b) The coefficient of restitution between two stainless steel 316 particles when they are rolling (red squares) or initially in contact (orange triangles). (c) The coefficient of restitution between two stainless steel 440c particles when they are rolling (blue circles) or initially in contact (purple diamonds)

We perform measurements to extract the coefficient of restitution for collisions between two particles that are initially in direct contact as well. To create contacting pairs of micro-particles, the computer-controlled micro-manipulator is used to push the two particles together to where the laser beam is focused. The striker particles are excited with varying laser energy and the trajectory of the second particle is measured. Since the striker particle has no trajectory before collision, the initial velocities of the particles are estimated from the calibration of momentum gain at different laser power, as described in Chapter 3. We plot the coefficients of restitution at different impact velocities for both stainless steel 316 (orange triangles) and 440c (purple diamonds) in Fig. 4.4b-c.

The first observations demonstrate that the coefficients of restitution in these measurements are higher than the one measured in the collisions between separated particles, which implies that collisions

result in less loss when the rotational motion of particles is reduced. The coefficient of restitution approaches unity for stainless steel 440c particles, which is again a higher value than the one obtained for the rougher 316 particles. From the calibration results shown in Chapter 3, we know that the momentum gained by the striker has a 15% standard deviation, which should contribute to the error of measurement of the coefficient of restitution. From the data we can see that the standard deviation of the coefficient of restitution for the 440c particles is approximately the same as the contribution of the system; as such we can argue that the resultant velocity after collision should be highly reproducible with uncertainty that is much less than 15%.

These results are fundamentally important to our goal of studying the wave propagation in micro-granular particles, because they imply that neighboring particles in contact can transfer energy with little dissipation within certain ranges of initial velocities. Without this result, the dissipation of the mechanical energy would prevent the propagation of nonlinear waves in a micro-granular chain.

4.5. Summary

In this chapter, we studied the motion and collision of dry micro-particles in a groove and experimentally investigated the fundamental principles that govern their behavior. We modeled the particles in a groove (Eq. (4.8)) with empirical parameters obtained directly from experiments.

$$\frac{d}{dt}v_z = -sign(v_z - sv_a)g\mu_{pg}/\mathrm{s} - (\frac{v_z}{T} - \frac{{v_z}^2}{L}),$$

$$\frac{d}{dt}v_a = sign(v_z - sv_a)kg\mu_{pg},$$

where, $T = 0.052\,s$, $L = 2.5\,mm$, and $\mu = 0.337$ and 0.293 for stainless steel 316 and 440c, respectively. The empirical model obtained in this chapter was used as the foundation for modeling wave propagation in multi- particle micro-granular systems.

By using proper fitting techniques, we can resolve the angular motion of the particles that are governed by the above equations. After studying the relation between the normal force and tangential force during impact, we found that it can be described with Coulomb friction with $\mu_{pp} = 1.4$. We also measured the coefficient of restitution during impact for both separated and neighboring particles. The results show that at low impact velocities, little momentum loss is observed when two micro-particles that are initially in contact collide. This implies the possibility of observing traveling pulses in micro-granular systems that are composed of larger numbers of particles in contact.

Chapter 5

The Dynamics of Dry, Microscopic Granular Chains

In the previous chapter, we established a set of empirical equations of motion for the particles in a groove. In this chapter, we describe the dynamic response of one-dimensional chains of particles in contact in response to a mechanical impulse excitation. The particles tested for this analysis are made of stainless steel 316 and stainless steel 440c (see Table 2.1); all particles have a diameter of 300 micrometers. The rest of this chapter is organized as follows: in section 5.1, we discuss the modeling approach that is used in the analysis and the results that are obtained with it, predicting the propagation of solitary waves. In section 5.2, we present the measured properties of the stress waves that are propagating through these systems (including their group velocity) and amplitude decay. In section 5.3, we discuss the dynamic response of non-ideal particle chains and study the influence of defects (i.e., the presence of inter-particle gaps) in the measured response of micro-granular chains. In section 5.4, we summarize the findings.

5.1. Modeling solitary waves in micro-granular chains

We model the system of micro-particles assuming Hertzian contact interactions and free boundary conditions, using the empirical equations of motion of a free-moving particle that were obtained in the previous chapter. Accordingly, we can describe the motion of the i[th] particle in the chain as:

$$\begin{aligned} & m\,\ddot{z}_i = -sign\left(\dot{z}_i - sR\dot{\theta}_i\right)mg\mu_{pg}/\mathrm{s} - \mathrm{m}(\dot{z}_i/T_0 - \dot{z}_i{}^2/\mathrm{L}) + f_{i-1,i}(z_{i-1}, z_i) - \\ & f_{i,i+1}(z_i, z_{i+1}), \\ & I\ddot{\theta}_i = \mathrm{R}(sign\left(\dot{z}_i - sR\dot{\theta}_i\right)mg\mu_{pg} - sign\left(\dot{\theta_{i-1}} + \dot{\theta}_i\right)f_{i-1,i}(z_{i-1}, z_i)\mu_{pp} \pm \\ & sign\left(\dot{\theta}_i + \dot{\theta_{i+1}}\right)f_{i,i+1}(z_i, z_{i+1})\mu_{pp}), \end{aligned} \tag{5.1}$$

where z_i is the coordinate of the i[th] particles, and $f_{i-1,i}(z_{i-1}, z_i)$ is the Hertzian contact force between the (i-1)[th] and i[th] particles. In Eq. (5.1), $T = 0.052\ s$, $L = 2.5\ mm$, $\mu_{pg} = 0.293$, and $\mu_{pp} = 1.4$ are the empirical parameters obtained in Chapter 4. By using a fourth-order Runge–Kutta solver with a 1 ns time step to solve this equation of motion numerically, we simulate the dynamics of granular chains composed of 15 stainless steel 440c particles with a radius of 150 μm that are resting on a v-

groove (i.e., the micro-granular chain we constructed experimentally; see the next section). The particles are in a close-packed condition with zero pre-compression. We are interested in finding the relationship between the striker velocity and the propagating wave group velocity, to compare the numerical results with the continuum theory derived for highly nonlinear systems [3] (as described in Chapter 1). The solution of the system of equations of motion shows that for a perfectly packed system, the stress waves propagate through the chain forming a solitary wave; this is similar to what has been reported for macroscopic granular systems [36]. An example of the evolution of the particle velocity in time for all 15 particles in the chain as computed numerically is shown in Fig. 5.1a. For these results, the micro-granular chain was excited with an initial striker velocity of 0.1 m/s. It can be seen that when the particles are in close contact, the maximum velocity reached by the particles is about 2/3 of the striker velocity. We perform further numerical simulations to examine the dependency between the maximum particle velocity and the initial striker velocity; the results are shown in Fig. 5.1b. We find a linear relationship between the maximum particle velocity and the striker velocity, $v_{max} = 0.64 v_{striker}$. In Fig. 5.1c, we show the calculated group velocities (red dots) for the propagating stress wave at different initial striker velocities. For comparison, in this figure we also plot the solution of Eq. (1.4), which is the analytical solution derived by Nesterenko for a granular chain that is interacting with only Hertzian force (no rotational degrees of freedom) [2]. By substituting $v_{max} = 0.64 v_{striker}$ from fitting the data in Fig. 5.1b, we have $v_g = \sqrt[5]{\frac{16}{25}} c^{4/5} {v_{max}}^{1/5} = \sqrt[5]{\frac{16}{25}} c^{4/5} (0.64 v_{striker})^{1/5}$. The corresponding (blue) curve in Fig. 5.1c matches the simulation results very well, despite the absence of rotational degrees of freedom in the Nesterenko theory. These results are in line with the analysis of macroscopic granular chains as described in Chapter 1 and in [2].

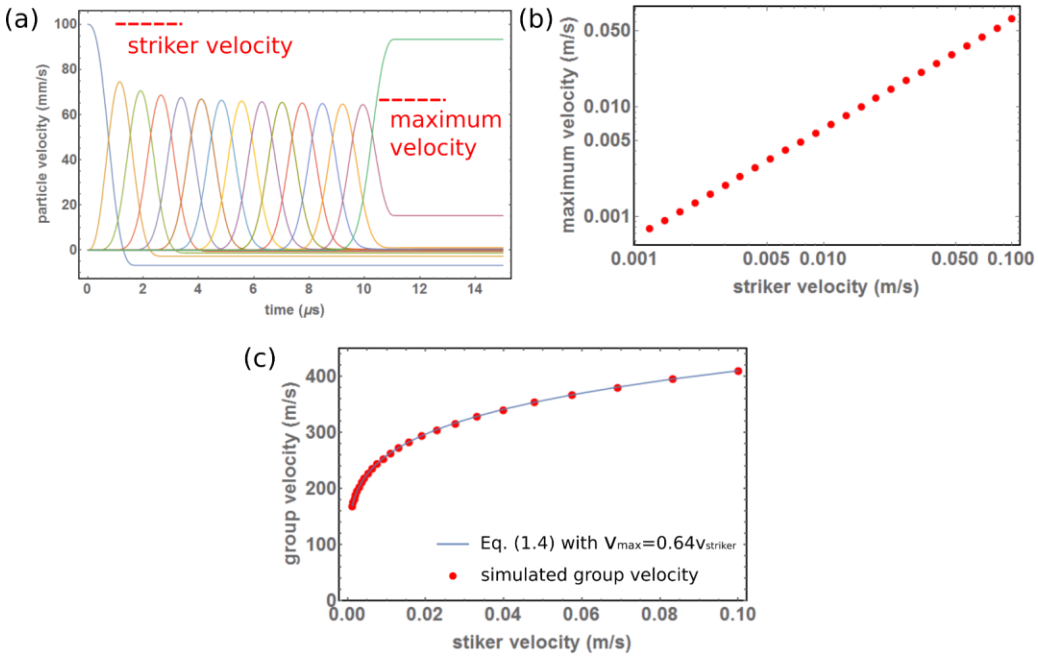

Figure 5.1: Numerically computed nonlinear waves traveling in an uncompressed, micro-granular chain that consists of 15 stainless steel particles (440c) with a radius of 150 μm. The first particle (the striker) has an initial velocity of 0.1 m/s. (a) Velocities of micro-particles along the chain. The solitary wave is seen to evolve to a stable shape after traveling through the first few particles. (b) Calculated maximum particle velocity at different initial striker velocities. The results can be fitted with a linear relation, $v_{max}\sim 0.64 v_s$. (c) Calculated group velocities (red dots) at different initial striker velocities. The results match with the analytical solution for a granular chain (Eq. (1.4) if the $v_{max}\sim 0.64 v_s$ obtained in (c) is assumed.

The agreement between the two models (Eq. 1.4 and Eq. 5.1) might be surprising at first, but it can be understood by estimating the energy transfer to the rotational degrees of freedom (due to the presence of Coulomb friction in our model) and the energy loss that results from dissipation (due to air friction). The ratio between the energy transfer/loss can be estimated with

$$\Delta E^{(Coulomb)}/E \sim -mg\mu_{pg}\Delta x/\frac{1}{2}m{v_{striker}}^2 \sim 2g\mu_{pg}\Delta x/{v_{striker}}^2, \tag{5.2}$$

and

$$\Delta E^{(air\ friction)}/E \sim \frac{1}{2}m{v_{striker}}^2\left(\exp\left(-\frac{2\Delta t}{T}\right)-1\right)/\frac{1}{2}m{v_{striker}}^2 \sim -\frac{2\Delta t}{T}, \tag{5.3}$$

where Δx is the total traveling distance of all particles and Δt is the total interaction time. In the case presented in Fig. 5.1a, we have $\Delta x \sim 2\,\mu m$, $\Delta t \sim 10\,\mu s$, and $\frac{\Delta E^{(Coulomb)}}{E} \sim$ 0.1%, $\frac{\Delta E^{(air\ friction)}}{E} \sim$0.05%. These ratios are both very small compared to the total kinetic energy of the system. From an experimental point of view, a difference of 0.1% or 0.05% is well below the accuracy of the measurements and cannot be directly observed.

The solitary waves observed in the simulations have a temporal width of about 2 μs, which is challenging from an experimental point of view. To correctly resolve the pulse profile experimentally, we need a sampling bandwidth that is greater than 5 MHz. This requirement exceeds the bandwidth of our laser vibrometers (which are limited to operating up to 2.5 MHz). As a consequence, we expect the shape of the measured waveform to be distorted. However, in order to extract useful information from experiments and compare the experimental data with the theoretical models available, we measure the time evolution of the maximum particle velocity, which is not expected to be affected by the limited bandwidth. In the experiments, we measure the velocities of the 2nd and 13th particles in the chain and define their maximum velocities as $v_{max,1} \equiv v_{max,2\mathrm{nd}}$, $v_{max,2} \equiv v_{max,13\mathrm{th}}$. We compare these with the corresponding values obtained in numerical simulations. From our numerical simulations we obtain:

$$v_{max,2}{}^{(simulation)} = 0.72 v_{max,1}{}^{(simulation)},$$

$$v_{max,1}{}^{(simulation)} = 0.89 v_{striker}{}^{(simulation)},$$

$$v_{max,2}{}^{(simulation)} = 0.64 v_{striker}{}^{(simulation)}.$$

In the next section, we compare these numerical results with the corresponding values obtained experimentally.

5.2. Wave propagation in micro-granular chains

To perform experimental measurements of wave propagation in micro-granular chains, we excite the first particle of an assembled micro-granular chain with the laser ablation system, which provides a controlled initial momentum. We measure the propagation of waves along the chain at selected particle locations using two laser vibrometers. To ensure precise excitations, the laser focus needs to be aimed very accurately on the striker. Poor laser excitation alignment results in particles gaining

velocity components in unwanted direction and results in the scattering or buckling of the constructed micro-granular chains.

We measure the time-dependent velocity profiles of the 2nd and 13th particles in the chain, as described in Chapter 2. A typical measurement obtained by the two vibrometers is shown in Fig. 5.2a.

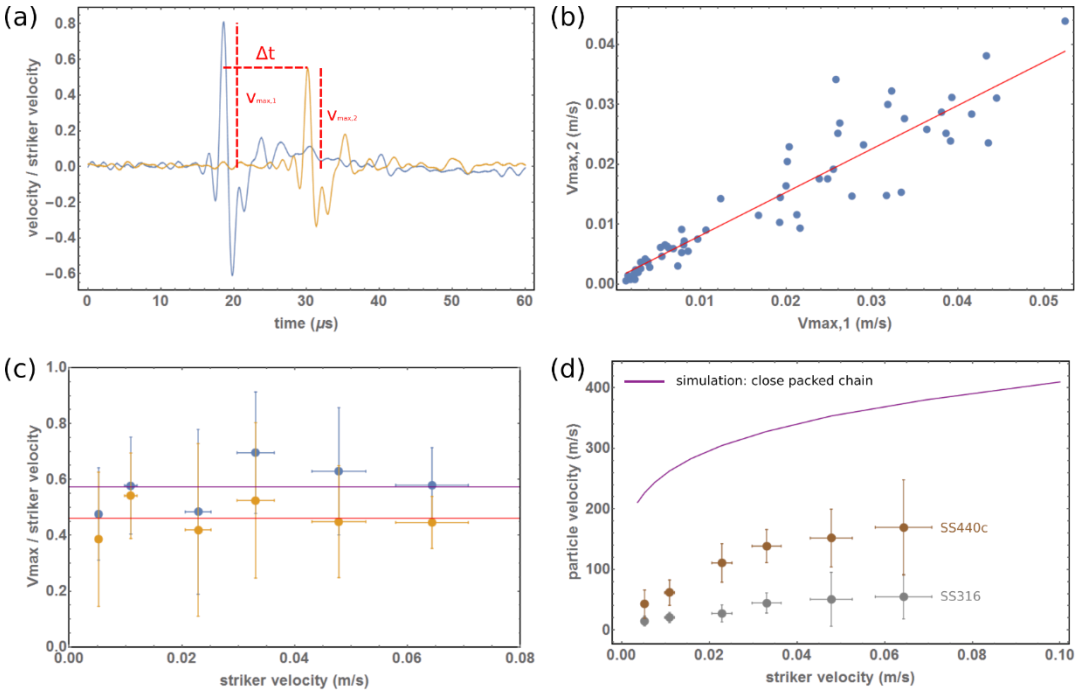

Figure 5.2: Measured particle velocities in a micro-granular chain of 15 stainless steel 440c particles (a) Measured particle velocities (rescaled with the calibration Eq. 2.1 and normalized by the striker velocities) for the 2nd and 13th particles in the chain. From these data we obtain the maximum particle velocities, $v_{max,1}$ and $v_{max,2}$, and the time delay Δt. (b) Measured maximum velocities (red dots) of the two monitored particles. The red fitting line has a slope of 0.80 ± 0.08 (95% confidence interval). (c) Measured maximum velocities (normalized to the striker velocity). An averaging gives $v_{max,1}/v_{striker} = 0.57 \pm 0.09$ and $v_{max,2}/v_{striker} = 0.46 \pm 0.07$ (95% confidence interval). (d) Measured group velocities at different striker velocities.

A typical measurement obtained by the two vibrometers is shown in Fig. 5.2a. The measured vibration is a filtered pulse response function (which is not representative of the real pulse shape because of the bandwidth limits). From this data, a reconstruction of the original waveform shape is difficult. To overcome this issue, as mentioned in the previous section we extract from the vibrometer data only the maximum values of the wave velocities and make no analysis or consideration of the shape and/or

frequency content of the propagating waves. We measure the maximum amplitudes, $v_{max,1}$ and $v_{max,2}$, of the two velocities output by the 2nd and 13th particles and time delays between the maximum amplitudes Δt. We plot the measured $v_{max,1}$ and $v_{max,2}$ in Fig. 5.2b. Despite the large variation of the measured velocities, $v_{max,1}$ and $v_{max,2}$ show a linear dependency and are fitted to obtain their experimental ratio of $v_{max,2}/v_{max,1} = 0.80 \pm 0.08$ (95% confidence interval). This result has a good agreement to the simulation results, ${v_{max,2}}^{(simulation)}/{v_{max,1}}^{(simulation)} = 0.72$. It might seem counter-intuitive that the experimentally obtained ratio between $v_{max,2}$ and $v_{max,1}$ is bigger than the one obtained through simulation, as we know for a perfect Nesterenko granular chain, the maximum velocities decay slightly as the wave propagates (see Fig. 5.1a). We also expect that any energy loss due to imperfection of the experimental system should only contribute to further decreasing the value of $v_{max,2}$. This interesting observation is explained in the next section, where the presence of gaps between particles is considered.

In Fig. 5.2c, we plot the measured $v_{max,1}$, $v_{max,2}$ at different striker velocities; the $v_{max,1}$, $v_{max,2}$ shown are normalized to $v_{striker}$. We have averaged the values of $v_{max,1} = (0.57 \pm 0.09)v_{striker}$ and $v_{max,2} = (0.46 \pm 0.07)v_{striker}$. The predicted values obtained in numerical simulations are ${v_{max,1}}^{(simulation)} = 0.89{v_{striker}}^{(simulation)}$ and ${v_{max,2}}^{(simulation)} = 0.64{v_{striker}}^{(simulation)}$. It seems that the measured values are about 40% smaller than the simulation, which might be a result of extra-loss on the striker due to imperfections in the construction of the chain.

Next we plot the measured group velocity $v_g = (13 - 2)2R/\Delta t$ at varying striker velocities in Fig. 5.2d for both 316 and 440c stainless steel particles. We first see the (striker) velocity. The measured pulse shown in Fig. 5.4a is a filtered response function that is not representative of the real traveling pulse shape, because of the bandwidth limits of our laser acquisition system (as discussed above). From these experimental data, a reconstruction of the original waveform shape is difficult. To overcome this issue, we extract from the vibrometer data only the maximum values of the particle velocities and the time delays between them, Δt, as these values are not affected by the bandwidth limit. We do not analyze the shape and/or frequency content of the propagating waves. We plot the measured $v_{max,1}$ and $v_{max,2}$ in Fig. 5.2b. Despite the large variation of the measured velocities $v_{max,1}$ and $v_{max,2}$ it is possible to fit the data with a linear dependence. The experimental ratio is $v_{max,2}/v_{max,1} = 0.80 \pm 0.08$ (95% confidence interval). This result has a good agreement to the simulation results, ${v_{max,2}}^{(simulation)}/{v_{max,1}}^{(simulation)} = 0.72$. It might seem counter-intuitive

that the experimentally obtained ratio between $v_{max,2}$ and $v_{max,1}$ is bigger than the one obtained through simulation, as we know for a perfect Nesterenko granular chain, the maximum velocities decay slightly as the wave propagates (see Fig. 5.1a). We also expect that any energy loss due to imperfections in the experimental system should only contribute to further decreasing the value of $v_{max,2}$. This interesting observation is explained in the next section, where the presence of gaps between particles is considered.

Finally, we plot the measured group velocity $v_g = (13-2)2R/\Delta t$ at varying striker velocities in Fig. 5.2d for both 316 and 440c stainless steel particles. Remarkably, the propagating wave group velocity varies as a function of the striker velocity for both particles tested. This is a clear indication of the nonlinear interaction between the particles. From the data, however, we note a significant deviation of the group velocities from their predicted values to much lower values. This is again puzzling, since in previous plots we have observed a good agreement between the maximum velocities of the 2nd and 13th particles in the chains. It is surprising that the group velocities can deviate significantly, while the model accurately captures the maximum velocities. In order to explain this phenomenon, we analyze the effects of defects (i.e., gaps) in the chain and discuss the results in the next section.

5.3. Gaps in micro-granular chains

In order to explain the large deviation of the measured group velocity from the group velocity that was calculated with our numerical model for an ideal chain of particles that are perfectly in contact, we must consider the role of defects and gaps between particles in wave propagation. To compute these effects numerically, we include the presence of gaps between the micro-particles in our simulation (Fig. 5.3a). We perform numerical simulations of the wave propagation in a granular chain with randomly distributed gaps between neighboring particles. As seen in Fig. 5.3b, when an average gap of 20 nm is included between each contact, the maximum particle velocity along the chain begins to oscillate (the particle velocity no longer decreases uniformly along the chain), and the oscillation amplitude has a variation of about 20%. This can explain the variations of $v_{max,1}$ and $v_{max,2}$ in the experimental data shown in previous section.

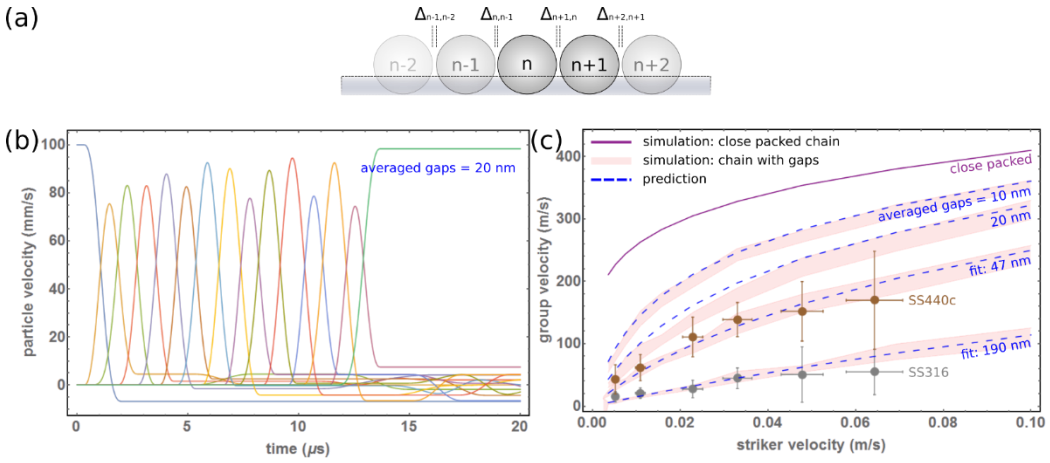

Figure 5.3: Wave propagation in micro-granular chains with gaps. (a) Schematic diagram of the setup obtained by assigning a random gap between neighboring particles. (b) Numerical simulations for waves propagating in a granular chain with gaps. The initial velocity is 0.1 m/s and the average gap size is 20 nm (c) Group velocity as a function of the striker velocity, at various gap sizes. Purple line: simulation of an ideal chain (gap=0). Pink bands: simulation results with randomly generated gap distributions, at a fixed average gap size ranging from 10 to 190 nm. Dashed lines: theoretical predictions obtained with Eq. (26), based on the group velocity of a close-packed chain. The measured group velocity is fitted with the simulation results (dashed lines) of systems with averaged gap = 190 and 47 nm for stainless steel 316 and 440c, respectively.

We then calculate the value of the average group velocity as a function of the striker velocity and compare the results with the experimental data obtained for the two types of particles. The average group velocity is now defined as $v_g = 11(2R + \bar{\Delta})/\Delta t$, where $\bar{\Delta}$ is the average gap size per contact along the chain. The randomly sampled group velocities, at different values of $\bar{\Delta}$, are shown as the pink bands in Fig. 5.3c. We use a simple equation to estimate the measured group velocity:

$$\frac{2R+\bar{\Delta}}{v_g(measurement,with\ gaps)} = \frac{2R}{v_g(simulation,no\ gaps)} + \frac{\bar{\Delta}}{v_{striker}}, \tag{5.4}$$

This formula assumes that the total time of flight is equal to the sum of the time required for a wave to travel through the particles and the time required for the free-moving particles to travel the distance of a gap to reach the neighboring particles. The estimated curves obtained from Eq. (5.4) for different gap sizes are plotted by the blue dashed lines in Fig. 5.3c. We can see that the blue dashed lines lie above the corresponding randomly sampled chains, which is because $v_{striker}$ is not the exact velocity of the free-moving particle, but the highest possible velocity of any particle within the system. The

resulting group velocity therefore defines the upper bound for a chain with randomly distributed gaps, in which the real velocity is lower than $v_{striker}$. These results show that even the presence of very little gaps can significantly alter wave propagation through micro-granular chains. For example, even gaps of only 20 nm (a value that is smaller than 0.1% of the diameter of the particles) can reduce the group velocity of the system by about 1/3. This results from the three order of magnitudes of difference between the group and striker velocities.

We further analyze the experimental data obtained with the close-packed stainless steel 316 and 440c particles. By fitting the experimental points in Fig. 5.3c with different average gap sizes, we show that numerical predictions estimate an average gap size of 190.4 nm in a chain of stainless steel 316 spheres and an average gap size of 47 nm for the chain of 440c particles. Note that the fitting curve lies above the experimental data because we fit it as an upper bound to the data points.

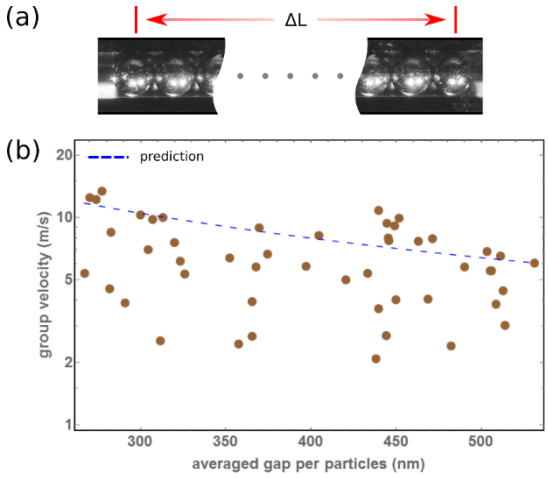

Figure 5.4: Experimental data of group velocity at different gap sizes. The chains are excited with an initial velocity of 0.01m/s and group velocities are measured on a loosely packed chain. (a) Measurement of the total length of the chain. (b) Experimental data for the group velocity (brown dots) and predictions (dashed line). The data are scattered but remain below the upper bound of the dashed line.

Experimentally, no direct way is available for resolving and measuring nanometer-size gaps in a given chain. To further analyze the effect of the gaps in experiments, we intentionally create micro-granular chains with a controlled length (defining an upper bound for the gaps). We create "loosely packed" chains, with a total length that is equal to the length of the ideally packed chain plus 4 to 8 μm. The total length L of each chain is measured with the microscope system. We use $(\Delta L - 11 \times 2R)/11$ to

estimate the average gap size within each chain. We then excite the chains with the striker particle with a fixed striker velocity of 0.1 m/s and measure the resulting group velocities. The results are shown in Fig. 5.4. The numerically predicted curve for the corresponding group velocity is plotted with a dashed line, while the experimental data of the measured group velocities are indicated by brown dots. The measured group velocity appears to be scattered but is generally below the predicted upper bound of the dashed line, which is expected from Eq. (5.4).

5.4. Summary

In this chapter, we experimentally investigated the wave propagation within a one-dimensional chain of micro-particles. We constructed the micro-granular chain with a carefully engineered micro-manipulator system and measured the traveling wave within the chain at different initial striker velocities. We obtained good agreement of propagation amplitude with simulation, but we observed a disagreement in the measured group velocities. This deviation is later explained with the presence of gaps within the non-compressed chain. Further simulation and experiments are then performed to quantify the influence of the gaps on the group velocity.

Chapter 6

Wave Propagation in a Two-dimensional Colloidal System

In the previous chapter, we analyzed wave propagation through dry, one-dimensional micro-granular chains in air. The generalization of the results to two-dimensional, micro-granular lattices is an interesting fundamental question. Earlier experimental investigations of wave propagation in macroscopic two-dimensional granular lattices have shown that lattice configuration plays a crucial role in determining the possible traveling wave that is supported by the granular system [85, 128]. For example, in contrast to the one-dimensional system, no genuine traveling wave excitations with constant velocity have been found to persist in a hexagonal configuration [148]. The new dimensionality not only introduces more interaction between particles and more possible direction for wave propagation, but it also changes the behavior of mechanical wave transport within the system.

However, the dynamics of two- or three-dimensional ordered granular systems are relatively poorly understood. While it is suggested that a squared lattice granular system should behave similarly to a one-dimensional granular chain when the solitary wave is propagating along the lattice vectors, direct generalization of solitary wave solution to two- or three-dimensional systems has not yet been derived. Early experimental efforts by Shukla et al. use photoelasticity techniques (including cubic and hexagonal packing) to image wave propagation in various two-dimensional granular crystals [47, 79-84]. These researchers' experiments show that within higher dimensional granular crystals, the force load path is influenced by the contact angle between lattice elements and wave propagation is altered by the vectors connecting the centers of mass of the neighboring particles. The new dimensionality not only introduces more interaction between particles, but also brings new degrees of freedom for designing and engineering the lattice to achieve desired wave propagating properties. Leonard et al. studied the wave propagation in two-dimensional square lattice of spherical particles [85] and showed that by inserting cylindered intruders into square lattices of spherical particles, alternating both the wave direction and energy flux is possible [86].

The testing of two-dimensional granular systems has also been shown to be sensitive to the presence of defects and imperfections in the lattice packing. Experimental results of different two-dimensional arrangements of particles all showed that variations due to inter-particle gaps, surface defects, particle size variations, and the flatness of the supporting structure all affect the repeatability of the measured dynamic response. As the scale of the particles is reduced, these effects are expected to become more dominant, particularly in a dry environment where the physical contact between particles is not altered by surrounding media.

To overcome these limitations, we explore wave propagation in two-dimensional micro-granular systems that are immersed in a fluid environment. For this we test colloidal systems that are composed of SiO2 particles in a water glycerol solution. In these systems, hexagonal lattices of SiO_2 particles with a radius of 3.69 μm can be constructed using self-assembling techniques. We investigate these colloidal systems' dynamics by delivering controlled kinetic energy that is several orders of magnitude higher than the background kinetic energy to specific particles within them. With higher kinetic energy, we are able to observe the inter-particle interaction at a much higher velocity and consequently much smaller inter-particle distance. This allows us to characterize the particle-particle interactions and their roles in particle wave propagation within the colloidal systems.

6.1. Modeling the two-dimensional colloidal systems

The colloidal system of SiO_2 particles studied in this chapter differs from the dry particle system in the previous chapter not only due to the much smaller particles size, but also because of the presence of the background fluid. In this system, hydro-dynamic interactions between particles are a dominating factor in the dynamic response of the colloidal system. In the inertia regime, other types of forces such as lubrication hydrodynamic forces [122, 149], elastic contact forces [150], and even elatohydrodyamic forces [151, 152] might become significant in addition to the elastic inter-particle interactions. In this section, we detail the model that we developed for the colloidal systems. In this model, the inter-particle interactions between neighboring particles include contact forces, electrostatic forces, Stokes' drag forces, and hydrodynamic forces.

For particle i interacting with another particle j, the total force on particle i is

$$\vec{f_i} = \overrightarrow{f_{\text{stoke,ij}}} + \overrightarrow{f_{\text{electrostatic,ij}}} + \overrightarrow{f_{\text{hydro,ij}}} + \overrightarrow{f_{\text{contact,ij}}}, \tag{6.1}$$

where $\overrightarrow{f_{\text{electrostatic,ij}}}$ is the electrostatic force due to the surface charges on the particles, $\overrightarrow{f_{\text{stoke,i}}}$ is the Stokes' drag on particle i moving in the fluid, $\overrightarrow{f_{\text{electrostatic,ij}}}$, $\overrightarrow{f_{\text{hydro,ij}}}$, and $\overrightarrow{f_{\text{contact,ij}}}$ are respectively the electrostatic, hydrodynamic, and contact interactions between the two particles.

The electrostatic force, $\overrightarrow{f_{\text{electrostatic,ij}}}$, is formulated [153] as

$$\overrightarrow{f_{\text{electrostatic,ij}}} = \frac{1}{4\pi\varepsilon}\left(\frac{Z}{1+\kappa R}\right)^2 \left(\kappa \frac{e^{-\kappa D_{ij}}}{|\overrightarrow{X_i}-\overrightarrow{X_j}|} + e^{-\kappa D_{ij}} \frac{1}{|\overrightarrow{X_i}-\overrightarrow{X_j}|^2}\right), \tag{6.2}$$

where ε is the permittivity of the background medium, κ is the screening coefficient of the electrostatic force, Z is the surface charges, R is the radius of the particles, and $D_{ij} \equiv R_i + R_j - |\overrightarrow{X_i} - \overrightarrow{X_j}|$ is the distance between the surfaces of the two particles that are located at $\overrightarrow{X_i}$ and $\overrightarrow{X_j}$. Following the derivation in [149], the hydrodynamic force caused by the existence of the background fluid contributes to the dynamics with a velocity-dependent force that resists the relative motion in the normal direction, as well as with a tangential force between the two particles (when tangential motion exists):

$$\overrightarrow{f_{hydro,ij}} = \begin{pmatrix} f_{(hydro)n} \\ f_{(hydro)t} \end{pmatrix} = \begin{pmatrix} -6\pi\mu R^2/D_{ij} & \frac{12}{5}\pi\mu R\sqrt{2R/D_{ij}} \\ 0 & -2\pi\mu R\sqrt{2R/D_{ij}} \end{pmatrix} \begin{pmatrix} v_{n,ij} \\ v_{t,ij} \end{pmatrix}, \tag{6.3}$$

where μ is the dynamic viscosity of the background fluid. In reality, because of the surface roughness of the particles, two particles approaching each other would have contact before D_{ij} reaches zero. We define this distance as the cutoff distance D_{cut}, and Eq. (28) only holds when $D_{ij} > D_{cut}$. Once the two particles are in contact ($D_{ij} < D_{cut}$), the tangential force becomes zero, $f_{(hydro)t} = 0$, and the normal force is modified to:

$$f_{(hydro)n} = -6\pi\mu R^2 \frac{v_{n,ij}}{D_{ij}} \left(1 - \frac{\delta_{ij}}{D_{ij}}\right). \tag{6.4}$$

Here, $\delta_{ij} \equiv R_i + R_j + D_{cut} - |\overrightarrow{X_i} - \overrightarrow{X_j}|$ is the real deformation of the particles with the cut-off distance, D_{cut}, included. Correspondingly, the contact force, $\overrightarrow{f_{\text{contact,ij}}}$, is a modified version of Eq. (1) with D_{cut} included [154]:

$$f_{ij}(x_i, x_j) = \frac{4}{3}\frac{E_i E_j}{E_i(1-\nu_j^2)+E_j(1-\nu_i^2)}\sqrt{\frac{2R_iR_j}{R_i+R_j}}\left(R_i + R_j + D_{cut} - |x_i - x_j|\right)_+^{\frac{3}{2}}. \quad (6.5)$$

In this model, D_{cut} is an artificial cut-off distance between the hydrodynamic and contact interactions, which we estimated based on the experimentally measured roughness of the particles' surface. The parameters used in the model are listed in Table 6.1. With this model, we can simulate the wave propagation behavior at different initial velocities through a two-dimensional hexagonal lattice of particles.

Material properties	Values
D_{cut} (nm)	24
κ (1/nm)	1/300
Z (G)	600
E (GPa)	73.1
υ	0.17

Table 6.1: The parameters for numerical simulation with Eq. (6.1).

6.2. Excitation of mechanical waves in colloidal systems

In experiments, we begin by testing the dynamic response of the hexagonal lattice to a controlled energy input. The experimental setup has been described in Chapter 2. At first we create a hexagonal lattice within the micro-fluidic cell using the self-assembling techniques. In order to excite the transparent SiO_2 particles, we deposit a metal layer of SiO_2 particles and mix it with the uncoated one at a ratio of 1 to 500. Using the laser ablation technique, we excite the particles around the coated particle and observe the displacement of the surrounding particles with our high-speed imaging system at a rate of 311111 frames per second.

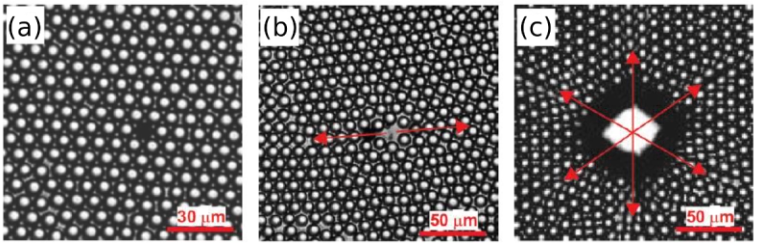

Figure 6.1: Images of laser excitation of micro-particles in a hexagonal lattice. (a) Photograph of a lattice prepared for laser excitation. The dark particle in the center is a micro-particle coated with 50 nm of Au that is targeted by the laser. (b) Excitation of the system with a weak laser pulse with energy of 0.1 μJ. The target particle obtains an initial

velocity in the direction of the red arrows. (c) Excitation of the system with a strong laser pulse of 0.25 μJ. Isotropic wave propagation in all directions is observed.

Fig. 6.1 shows the high-speed images of a typical response of the system to laser excitation. A coated particle originally at rest in a hexagonal lattice (Fig. 6.1a) is shot by weak (Fig. 6.1b) or strong (Fig. 6.1c) laser pulse. In the weak case, the laser energy projected onto the particle is 0.1 μJ and results in a linear motion of the excited particles along the red arrows. At higher power, a more isotropical displacement of particles occurs along the six preferred directions in the hexagonal lattice (which are labeled by the six red arrows in Fig. 6.1c). The difference between linear particle motion and isotropic excitation may be due to the initial disorder of the hexagonal lattice or the inhomogeneity of the coated surface.

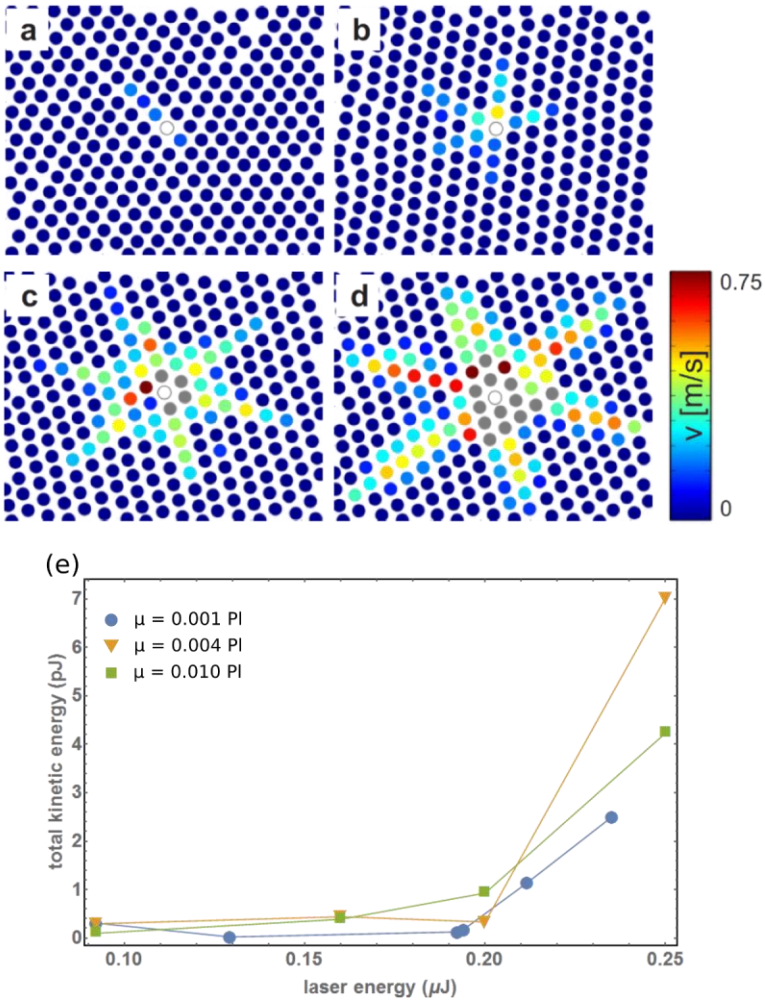

Figure 6.2: The velocity and kinetic energy transfers to the colloidal system by laser excitation. The velocity map of the system excited at (a) 0.13, (b) 0.19, (c) 0.21, and (d) 0.23 μJ shows that at lower energy (less than 0.15 μJ in our system), the laser can only excite the linear motion of the coated particles. At higher power the laser is capable of exciting mechanical impulses in all six hexagonal directions. The higher the laser energy, the farther the wave can reach out from the center. (e) The total kinetic energy of micro-particles in the lattice at different laser powers and background fluid viscosities. The energy transfer efficiency is about 0.001%, which is close to the efficiency when exciting one particle (see Chapter 3).

Using imaging processing techniques, we obtain the averaged velocities of the colloids in the lattice. An averaged velocity is defined as $\bar{v} \equiv \Delta x/\Delta t_c$, where Δx is the displacement observed in one frame and Δt_c is the sample interval of the high-speed camera (which is $1/311111$ in our system). We analyze the data of the colloidal system excited at different laser energy and plot the velocity map in Fig. 6.2. We can see decay of particle velocity over the distance from the center of laser impact. The

laser energy of the excitation is 0.13, 0.19, 0.21, and 0.23 μJ for Fig. 6.2a-d, respectively. At the low power excitation of 0.13 μJ, the linear excitation is observed again; while the laser energy increases, a more uniform displacement in all directions can be seen and the observed averaged velocity reaches out farther from the center of laser impact. While the exact mechanism of the laser excitation of the lattice is unclear given that the event happens much faster than the acquisition rate of our high-speed imaging system, the phenomenon is shown to be very reproducible and can be used as an experimental technique for exciting wave propagation in hexagonal lattices.

From the calibration of particle velocity at fixed laser energy and dynamic viscosity of the background fluid (Chapter 3), we know that the hydrodynamic properties of the background fluid are major factors influencing the laser excitation process. To gain more insight into the laser excitation, we vary the viscosity of the background fluid and calculate the total kinetic energy of all particles of the resulted measurement; the result is shown in Fig. 6.2e. Here we define the total kinetic energy of the system with the average velocity that we obtained from the experiment, $E_k = \sum m\bar{v}^2/2$, where m is the mass of the colloids. The efficiency of energy transfer is about 0.001%, which is very close to what we have seen in Chapter 3. Since the kinetic energy carried by the background fluid is not measurable using the imaging system, the results imply that the kinetic energies of the lattices excited by laser are mostly carried by the colloids that are visible experimentally. If this is true, our modeling of the colloids with particle-particle interaction (as opposed to a full hydrodynamic system that includes the fluid) should be sufficient for capturing most of the system's dynamics.

It is also interesting to see that the sample with viscosity equals to 0.004 Pl obtains more kinetic energy than the other two cases. When the laser excites the system, two competing factors influence the measured total energy: one is the higher efficiency of the PLA in fluid with higher viscosity, the other is the higher loss of kinetic energy due to higher viscosity. The first factor has already been discussed in Chapter 3; let us now consider the second one. If the colloids have a viscosity of μ, the Stokes' drag force ($f = -6\pi\mu Rv$) has a time constant of $2R^2\rho/9\mu$, which is 5.6, 1.4, and 0.56 μs for our SiO_2 particles when μ equals 0.001, 0.004 and 0.01, respectively. Considering our acquisition time of 3.3 μs, we expect very strong deceleration of the particles in the system with $\mu = 0.01\ Pl$, which explains the suppressed total kinetic energy. In the following work, we consider the laser excitation as a means to excite the six centermost particles simultaneously to the six hexagonal directions, with a controlled velocity that is determined by the laser energy and viscosity. Based on

this observation, we simulate wave propagation excited by laser in our colloidal system in the next section.

6.3. Mechanical wave propagation in colloidal systems

Until now we have been discussing the displacement and averaged velocities that are obtained experimentally. In order to gain more insight into the roles of different interactions between the particles in the system, in this section we perform numerical simulation of wave propagation. We start with the simulation of wave propagation behavior along the six branches of colloids in the hexagonal direction from the center (Fig. 6.3). In Fig. 6.3a, the coated particle is illustrated as the black particle in the center. After the laser excitation, the six neighboring particles obtain initial velocities and produce propagating waves in each hexagonal direction. We simulate the two-dimensional wave propagation with an initial velocity, v_{ini}, of 13 m/s, a viscosity of 0.004 Pl, and an initial distance between neighboring particles of 250nm. We choose a branch of particles from the six hexagonal directions and label those particles from 1 to 7. We plot the velocity of each particle in Fig. 6.3b and the inter-particle distance in Fig. 6.3d.

In Fig. 6.3d, we first notice that most of the evolution of the particles' velocities occurs within the first 200 ns and is quickly stabilized after 1 μs from the initial excitation. Since this is shorter than the minimal exposure time of our high-speed imaging system (2.7 μs), the details of the collision will not be resolved in the high-speed images; the measured displacement of the particle is the time-integration of velocity during the camera's acquisition time. In the first 200 ns, the particles collide with each other and pass on velocities along the chain. During this process, the velocities decay much faster than they do during the later period. The differences in velocity between particles are also being eliminated, and after the particles obtain similar velocities, their velocities decay exponentially. The fast elimination of velocity difference is the effect of the hydrodynamic force, $\overrightarrow{f_{hydro,ij}} \sim -\frac{6\pi\mu R^2}{D_{ij}} v_{ij} = -6\pi\mu \mathrm{R} \frac{R}{D_{ij}} v_{ij}$, which causes the relative velocities between neighboring particles, v_{ij}, to decrease. Notice that the hydrodynamic force differs with the Stokes' drag by a factor of $\frac{R}{D_{ij}}$. This is because in a close-packed lattice, $D_{ij} \ll R$, the hydrodynamic force is the dominant interaction that contributes to the decay of velocities before the velocity difference is eliminated. A closer look at the velocity of the first particle reveals a short period of acceleration after it collides with the second particle, which is again due to the hydrodynamic force resisting the separation of two particles.

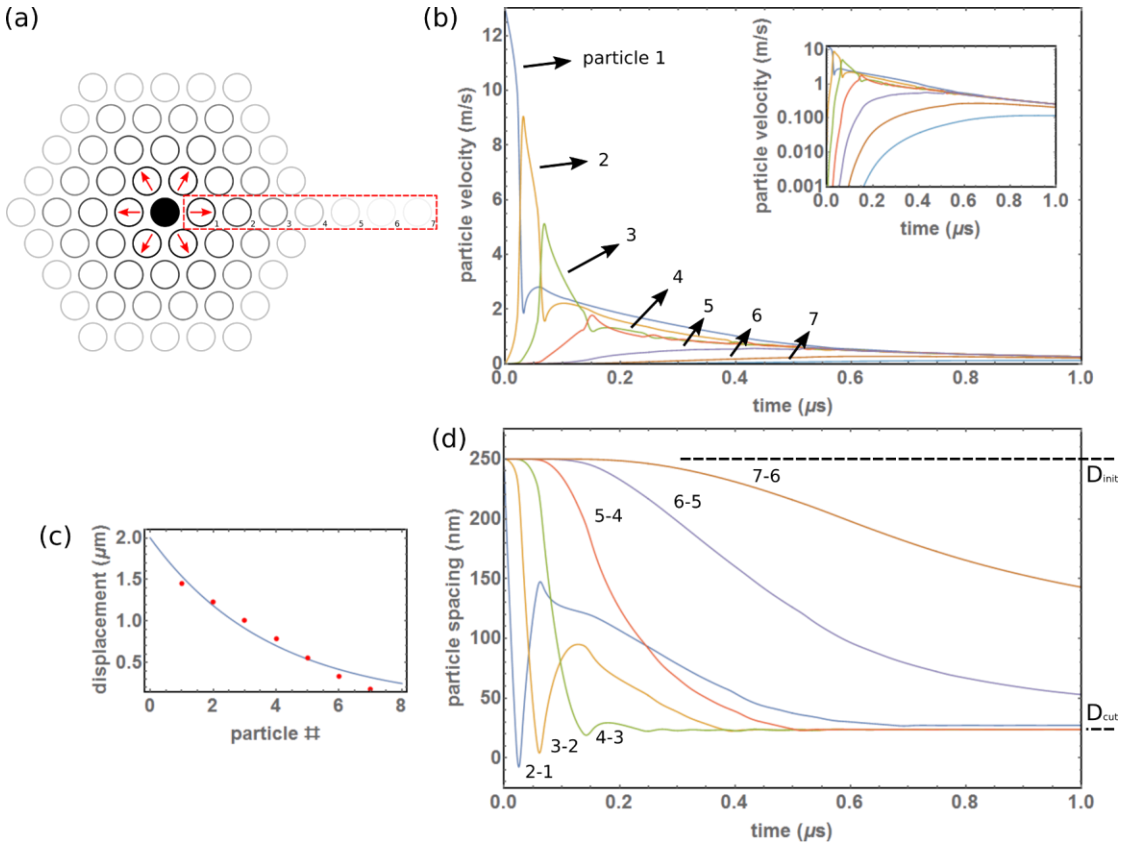

Figure 6.3: Numerical study of wave propagation along a chain within the hexagonal lattice. (a) Schematic diagram of the excitation and geometry of the lattice (b) The velocities of particles along the chain. (c) The total displacement (red dots) after the excitation obtained through simulation. It is fitted with an exponential decay formula and gives the decay length of 2.7. (d) The inter-particle distance during wave propagation.

In Fig. 6.3b, we also plot the same velocity result in log scale. It becomes clear that the final velocities of the particles approach the same value and results in the broadening of mechanical pulse. Due to the presence of the factor of $\frac{R}{D_{ij}}$ in hydrodynamic force, the broadening effects of hydrodynamic force on the traveling wave are more significant in a system where two particles can approach each other more closely. In our system this means when we have a higher initial velocity on the six centermost particles, the measured distance along the chain should decrease less since the particles obtain the same velocities more quickly than they do in the case of lower initial velocities.

It is noticeable that the velocity behavior of the first four particles is different from the behavior of later particles along the chain. The distinct behavior is due to the first four particles having reached

the regime of particle deformation. This deformation can be confirmed from Fig. 6.3d, in which the inter-particle distances between the first five particles have reach the cut-off distance, along with a faster bounce back. During the contact time, the particles transfer velocities via contact force, which is much more efficient than via hydrodynamic force. Whether a particle can reach the deformation regime is determined by whether its initial velocity is large enough to bring two particles into contact. In this case, the velocity barrier seems to be approximately 1 m/s.

To compare the simulation results with the experimental data of displacement, in Fig. 6.3c we plot each particle's final displacement, which decreases along the chain. To obtain a quantitative description of the decay, we fit the results with an exponential law of decay and obtain a decay constant of 28.2 μm.

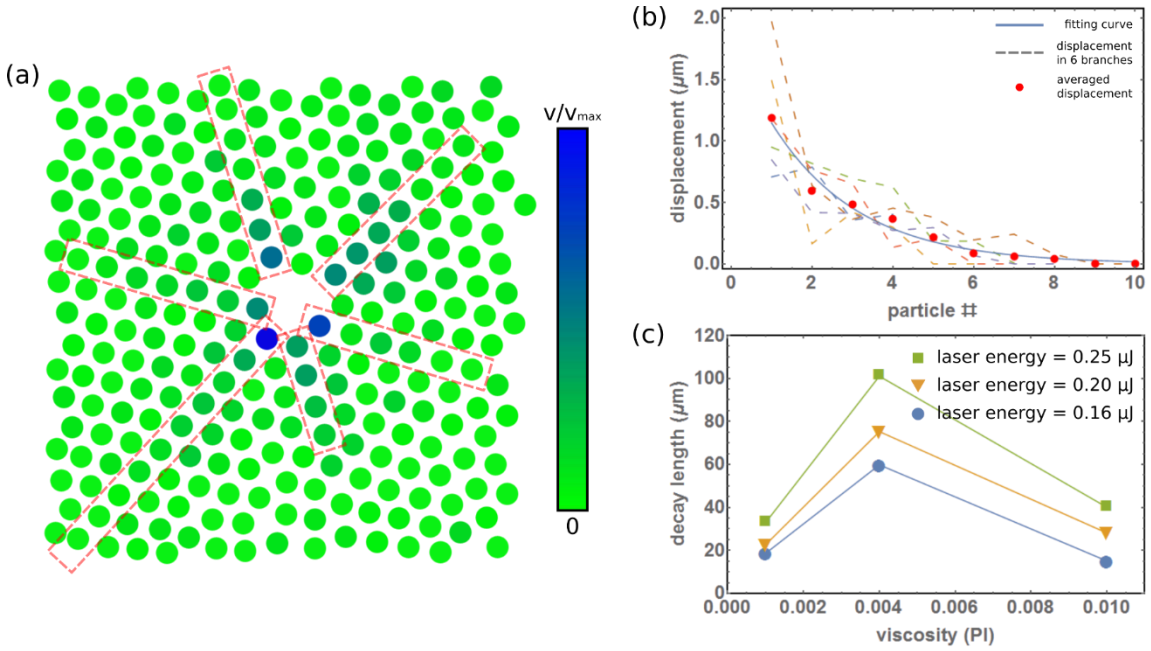

Figure 6.4: Experimental data of a wave propagation in the colloidal system with a viscosity of 0.01 Pl is excited by pulse energy of 0.16 μJ. (a) The measured velocity map of the system. The red boxes show the geometry of chains in the six hexagonal directions from the center particle. (b) The displacement of the particles that are shown in the red boxes in (a). (c) The decay length measured at different combinations of laser energy and viscosity.

In Fig. 6.4, we show experimental results of a velocity map of a system with a viscosity of 0.01 Pl as excited by pulse energy of 0.16 μJ. The six directions, which are marked by red boxes along the

lattice, and the displacement of particles within these boxes are shown by the dashed line in Fig. 6.2b. The decay can be seen from this dashed line. The averaged values (red dots) of the displacement at each distance are used to fit the exponential decay of the displacement along the chain. We obtain a decay length at varying laser energy and viscosity, as shown in Fig. 6.4c. The results show that for the same viscosity, the higher the laser energy (and initial velocities) are, the longer the decay length of the wave propagation. This agrees with the simulation, which indicates that a system with higher initial velocities will reach steady states (i.e., particles moving at the same velocities) faster and that the differences between the measured displacements along the chain will be smaller. With regard to the decay length obtained at the same laser energy, we expect it to be shorter given that at lower viscosity, the initial velocity excited by lasers will be less than in the case of higher viscosity. On the other hand, another competing factor is at play, namely the higher dissipation (and shorter decay length) due to higher viscosity. As a result we observe a shorter decay length of the same laser power at both low viscosity 0.001 (due to lower initial velocity) and high viscosity 0.01 (due to the higher dissipation).

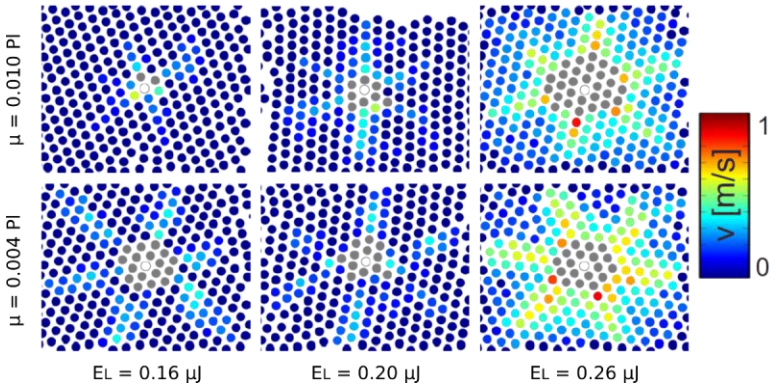

Figure 6.5: Velocity maps of the system tested at different laser energy and background fluid viscosity. The system is tested under a combination of viscosity equaling 0.001 Pl and 0.004 Pl and laser energy equaling 0.16, 0.20, and 0.25 μJ.

In Fig. 6.5, we show the experimental results of the velocity maps of systems of different viscosity as excited by different laser energy. Let us first compare images in the same column, which represents the system response at the same laser energy and different viscosity. The images with higher viscosity show shorter mechanical wave spans, which result from the high dissipation from higher viscosity. If we consider the fact that the laser transfers a higher initial velocity at higher viscosity, the effect of higher viscosity stopping the wave from reaching a farther distance from the center is even more

evident. Looking at the images in one row, we can see that at higher laser energy, the velocity distribution in the lattice becomes more isotropic. This can be explained by the tangential component of the hydrodynamic force, which is proportional to the tangential component of relative velocity between particles. Furthermore, at higher velocity, the particles in the chain in the six hexagonal directions could exert higher tangential force on the particles that are next to the chain. Since the hydrodynamic force is the main source for redistributing energy to the neighboring particles (other than the very small component of normal force that occurs when particles in the chain dislocate from their positions in an ideal lattice), a comparison of two systems dominated by the contact or hydrodynamic force will help to clarify the origin of isotropicity.

We simulate the behavior of two cases in which μ and v_{ini} are (a) 0.001 Pl, 8 m/s and (b) 0.004 Pl, 24 m/s. The higher initial velocity in the second case is included to account for the higher initial velocity that is obtained from the same laser energy acting on a system with higher viscosity. We obtain the evolution of the system at different time steps and plot the resultant velocity map in Fig. 6.6ab. In the fluid with a viscosity of 0.001 Pl, the wave propagates with little loss and redistribution to the other particles. In the fluid with a viscosity of 0.004 Pl, the wave decays faster and shows more isotropic propagation due to the strong hydrodynamic forces. The anisotropicity in the less viscous fluid comes from the fact that the deformation regime can easily be reached between the spheres in the branches due to lower hydrodynamic barriers. This allows more efficient momentum transfers between spheres in the branches, and as a result the hydrodynamic regime becomes less dominant in the evolution of the system and less energy is distributed onto the neighboring particles. These results indicate that the hydrodynamic force is the main contributing factor to the system's isotropicity.

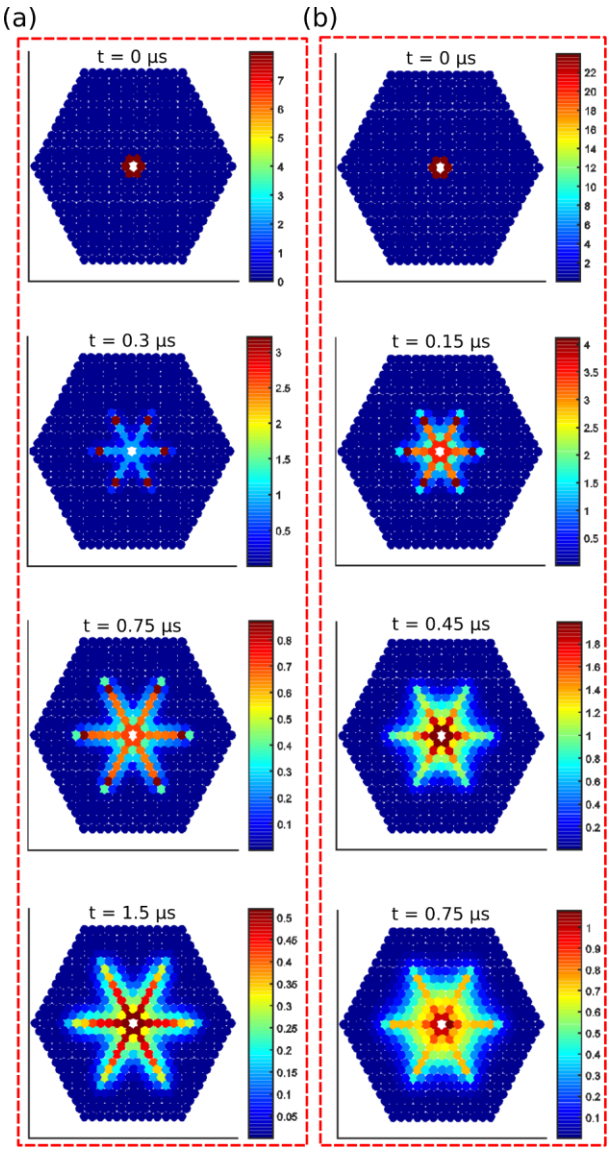

Figure 6.6 Numerical simulation of wave propagation generated with different initial velocities and fluid viscosities; μ and v_{ini} are (a) 0.001 Pl, 8 m/s and (b) 0.004 Pl, 24 m/s. The higher initial velocity in the second case is included to account for the higher initial velocity obtained from the same laser energy acting on a system with higher viscosity.

6.4. Summary

In this chapter we discussed the experimental and numerical examination of a two-dimensional micro-granular system that consists of a hexagonal lattice of SiO_2 particles with a radius of 3.69 μm. We performed the experimental examination by sending laser energy into the system to excite the initial velocity of one of the six centermost particles in the lattice. With the resultant velocity that is

high in comparison to traditional means, we are allowed to explore the system while the particles have enough velocity to break through the hydrodynamic barriers and to study wave propagation in systems of different viscosities. To capture the behavior of the system, we constructed a model that included the contact force, hydrodynamic force, electrostatic force, and Stokes' drag force and performed numerical simulation to study wave propagation at a time resolution higher than the one we used in our experimental system. The resultant simulation characterizes the roles of the hydrodynamic force and contact within wave propagation as well as explains the origins of isotropic wave propagation within the system.

Chapter 7

Conclusion & Future Work

7.1. Conclusion

In this thesis, we design an innovative experimental platform that allows us to assemble, excite, and characterize ordered micro-granular systems. In Chapter 2 and 3, we detail the design of a new experimental platform that employs both a laser system to deliver impulses with controlled momentum and non-contact measurements (including high-speed optical microscopy and laser interferometry) to detect particle displacement and velocity. We fabricate micro-structures to guide and confine the one-dimensional micro-granular system that is assembled using a computer-controlled micro-manipulator. In addition, we employ self-assembling techniques to create two-dimensional hexagonal lattices in micro-fluidic cells. We test and demonstrate the capability of the laser excitation system to deliver controlled momenta to the above systems of dry (stainless steel particles of radius 150 μm) and wet (SiO_2 particles of radius 3.69 μm, immersed in fluid) micro-particles.

In Chapter 4, we study the dynamics of particles in a one-dimensional micro-structure support. We first derive the governing equations of motion that describe the dynamic response of dry and wet particles on a substrate. To investigate how a micro-structure support influences the dynamics of micro-particles that are loaded onto it, we study the loss in our micro-particle configuration both analytically and experimentally. We measure the Stokes' and Coulomb friction of the micro-particles by tracking their trajectories at varying initial momenta. We study the collisions of rolling micro-particles in a groove to investigate the exchange of translational and angular momenta during collisions. Through observing inelastic collisions of rolling particles and nearly elastic collisions of particles that are initially in contact, we discover a linear dependency between the contact force and the tangential frictional force between the colliding particles. We obtain empirical equations of motions that describes the dynamics of the micro-granular system.

In Chapter 5, we investigate the mechanical wave propagation properties as well as the influence of defects in one-dimensional, dry chains of micro-particles. We measure the attenuation of the

mechanical wave along the chain at different initial striker velocities and show that it agrees with the theoretical prediction. We measure the delay time of wave propagation inside the chain and show that measured group velocity depends on the initial velocity. We compare the deviation of the measured group velocity with the case of a Hertzian system, and we numerically show that the deviation can result from the presence of defects (which here are gaps between micro-particles). To prove this we use the microscopic system to perform time of fly measurements for systems with a known maximum gap. We show that the measured group velocity agrees the numerical simulation.

In Chapter 6, we study wave propagation in two-dimensional colloidal systems that are immersed in fluid. We produce controlled mechanical wave impulses within the system, study the total energy transfer at varying laser energy, and observe the system's response displacement. We experimentally characterize the wave-attenuation and its relation to the viscosity of the surrounding fluid and perform computer simulations to establish a model that captures the observed response.

In this thesis we describe the first systematic experimental and numerical analysis of wave propagation in ordered systems of micro-particles. This work provides a foundation for advancing fundamental research of granular and colloidal systems and offers basic insights into the miniaturization of applications based on highly nonlinear granular systems.

7.2. Future work

In this thesis we present a new experimental framework and study micro-granular systems constructed on supporting structures that are fabricated with photolithography technology. Modern micro-fabrication technology provides us with well-studied fabrication processes that enable more sophisticated micro-structures for constructing micro-granular systems. The fabrication technology provides great experimental freedom for future studies related to micro-granular systems with different geometries, improving micro-granular system assembling, and the mechanical response of a hybrid system of a micro-granular and elastic materials.

The local, instantaneous delivery of momentum to micro-particles that is used in these experiments have several advantages. In the wet particle experiments, we demonstrate that with the high initial velocity that is generated by laser ablation, the particles have enough energy to overcome the hydrodynamic boundary and to interact with other particles with contact force (which is a regime that is difficult to access using traditional experimental tools for colloidal dynamics). This allows us to explore experimentally the interplay between hydrodynamic interaction and contact interaction, and

influence of these interactions on the collective behavior of the lattice. Using chemical growing techniques, colloidal particles can be fabricated to carry desired softness, surface roughness, and attractive or repulsive inter-particle electrostatic forces. The laser-based excitation system can be used to examine the dynamics of the customized fabricated colloidal systems.

This flexibility of laser excitation can also be applied to one- or three-dimensional colloidal systems. Since the laser only interacts with non-transparent particles that are near its focal point, a laser excitation can be delivered to the target particles within three-dimensional systems with negligible influence on other particles. This provides us with new ways to excite mechanical waves at specific locations within the colloidal systems, which will be useful for researching new categories of mechanical waves (which are difficult to generate using traditional means).

Non-contact laser-based excitation has a great advantage over traditional contact-based excitation, which is the ease of producing excitation at multiple locations by splitting and redirecting the laser beam. While we only use the laser to excite a single particle within the system in this study, the capability of exciting the system at multiple locations allows us to investigate the interaction between mechanical waves that are generated at different locations within the granular system. Future studies of the collision and interference of mechanical waves within micro-granular systems can advance the fundamentally understanding of the micro-granular system as a medium of wave propagation.

The mechanical response of the laser ablation has significant space for improvement. The stainless steel particles used in this work were not chosen for their good material response, and the complicated material composition of stainless steel is a possible cause of the 15% variation on output velocities. Future systematic searches for a better ablation material for mechanical wave generation would benefit the accuracy and repeatability of these laser-based experiments. An ideal ablation should possess efficient material response, high repeatability, low material consumption per ablation, and little influence on the sample. While materials with these properties might not be available, we expect that a great improvement in ablation performance could be achieved through switching to material that is better than stainless steel. Our experimental capacity would benefit from a material that is ideally suitable for mechanical wave generation, as it would enable accurate, repeatable, continuous operation of mechanical wave generation.

Finally, other than the material response of the laser ablation, more work can be done to improve particle manipulation mechanisms via the sophisticated control of laser beam profiles and positions.

Modern optics have a variety of tools to shape the laser pulse in time and spatial domains. For example, a spatial light modulator can alter the beam profile and direction by modulating the phase of the laser profile using liquid crystals. This device can be used to create multiple focus points as well as to shift the focus point in real time. Together with the image acquisition and processing system, future work to explore the manipulation of non-transparent colloids in micro-fluid systems with an optical griper that consists of laser focal points would benefit our fundamental ability to manipulate micro-particles. This advance could in turn be applied to studying complex two- and three-dimensional structures in colloidal systems or to manipulating objects in bio-mechanical systems. Unlike the optical tweezer (which can only be applied to transparent targets), laser ablation can be applied to non-transparent targets; as a result it can provide control over entirely different categories of micro-objects.

.

Bibliography

1. Garcia-Rojo, R. and H.H. J, *Powders and Grains 2005, Two Volume Set: Proceedings of the International Conference on Powders & Grains 2005, Stuttgart, Germany, 18-22 July 2005*. 2005: TAYLOR & FRANCIS.
2. Nesterenko, V.F., *Propagation of nonlinear compression pulses in granular media.* Journal of Applied Mechanics and Technical Physics, 1983. **24**(5): p. 733-743.
3. Nesterenko, V.F., *Dynamics of Heterogeneous Materials*. 2001: Springer.
4. Nedderman, R.M., *Statics and kinematics of granular materials*. 2005: Cambridge University Press.
5. Sen, S., F.S. Manciu, and M. Manciu, *Thermalizing an impulse.* Physica A: Statistical Mechanics and its Applications, 2001. **299**(3–4): p. 551-558.
6. Daraio, C., et al., *Energy Trapping and Shock Disintegration in a Composite Granular Medium.* Physical Review Letters, 2006. **96**(5): p. 058002.
7. Fraternali, F., M.A. Porter, and C. Daraio, *Optimal Design of Composite Granular Protectors.* Mechanics of Advanced Materials and Structures, 2009. **17**(1): p. 1-19.
8. Boechler, N., G. Theocharis, and C. Daraio, *Bifurcation-based acoustic switching and rectification.* Nature materials, 2011. **10**(9): p. 665-668.
9. Daraio, C., et al., *Strongly nonlinear waves in a chain of Teflon beads.* Physical Review E, 2005. **72**(1): p. 016603.
10. Khatri, D., C. Daraio, and P. Rizzo. *Coupling of highly nonlinear waves with linear elastic media.* in *SPIE Smart Structures and Materials+ Nondestructive Evaluation and Health Monitoring*. 2009. International Society for Optics and Photonics.
11. Spadoni, A. and C. Daraio, *Generation and control of sound bullets with a nonlinear acoustic lens.* Proceedings of the National Academy of Sciences, 2010. **107**(16): p. 7230-7234.
12. Donahue, C.M., et al., *Experimental realization of a nonlinear acoustic lens with a tunable focus.* Applied Physics Letters, 2014. **104**(1): p. 014103.
13. Campbell, C.S., *Rapid Granular Flows.* Annual Review of Fluid Mechanics, 1990. **22**(1): p. 57-90.
14. Bagnold, R.A., *The Shearing and Dilatation of Dry Sand and the 'Singing' Mechanism*. Vol. 295. 1966. 219-232.
15. Behringer, R., H. Jaeger, and S. Nagel, *Introduction to the focus issue on granular materials.* Chaos: An Interdisciplinary Journal of Nonlinear Science, 1999. **9**(3): p. 509-510.
16. Lydon, J., M. Serra-Garcia, and C. Daraio, *Local to Extended Transitions of Resonant Defect Modes.* Physical Review Letters, 2014. **113**(18): p. 185503.
17. Tkachenko, A.V. and T.A. Witten, *Stress propagation through frictionless granular material.* Physical Review E, 1999. **60**(1): p. 687.
18. Sadd, M.H., G. Adhikari, and F. Cardoso, *DEM simulation of wave propagation in granular materials.* Powder Technology, 2000. **109**(1): p. 222-233.
19. Jia, X., C. Caroli, and B. Velicky, *Ultrasound propagation in externally stressed granular media.* Physical Review Letters, 1999. **82**(9): p. 1863.
20. Wensrich, C., *Dissipation, dispersion, and shocks in granular media.* Powder technology, 2002. **126**(1): p. 1-12.

21. Schwager, T. and T. Pöschel, *Coefficient of normal restitution of viscous particles and cooling rate of granular gases.* Physical Review E, 1998. **57**(1): p. 650-654.
22. Jaeger, H.M., S.R. Nagel, and R.P. Behringer, *Granular solids, liquids, and gases.* Reviews of Modern Physics, 1996. **68**(4): p. 1259-1273.
23. Brilliantov, N.V., et al., *Model for collisions in granular gases.* Physical Review E, 1996. **53**(5): p. 5382-5392.
24. de Gennes, P.G., *Granular matter: a tentative view.* Reviews of Modern Physics, 1999. **71**(2): p. S374-S382.
25. Metcalfe, G., et al., *Measurement of particle motions within tumbling granular flows.* Chaos: An Interdisciplinary Journal of Nonlinear Science, 1999. **9**(3): p. 581-593.
26. Ding, J. and D. Gidaspow, *A bubbling fluidization model using kinetic theory of granular flow.* AIChE Journal, 1990. **36**(4): p. 523-538.
27. Chepurniy, N., *Kinetic theories for granular flow: inelastic particles in Couette flow and slightly inelastic particles in a general flow field.* Journal of fluid mechanics, 1984. **140**(223-222): p. 256.
28. Jop, P., Y. Forterre, and O. Pouliquen, *A constitutive law for dense granular flows.* Nature, 2006. **441**(7094): p. 727-730.
29. Huerta, D. and J. Ruiz-Suárez, *Vibration-induced granular segregation: a phenomenon driven by three mechanisms.* Physical Review Letters, 2004. **92**(11): p. 114301.
30. Choo, K., T. Molteno, and S.W. Morris, *Traveling granular segregation patterns in a long drum mixer.* Physical review letters, 1997. **79**(16): p. 2975.
31. Rapaport, D., *Simulational studies of axial granular segregation in a rotating cylinder.* Physical Review E, 2002. **65**(6): p. 061306.
32. Lee, J. and H.J. Herrmann, *Angle of repose and angle of marginal stability: molecular dynamics of granular particles.* Journal of Physics A: Mathematical and General, 1993. **26**(2): p. 373.
33. Daerr, A. and S. Douady, *Two types of avalanche behaviour in granular media.* Nature, 1999. **399**(6733): p. 241-243.
34. Jaeger, H.M. and S.R. Nagel, *Physics of the granular state.* Science, 1992. **255**(5051): p. 1523-1531.
35. Tournat, V. and V. Gusev, *Acoustics of unconsolidated "model" granular media: an overview of recent results and several open problems.* Acta Acustica United with Acustica, 2010. **96**(2): p. 208-224.
36. Lazaridi, A.N. and V.F. Nesterenko, *Observation of a new type of solitary waves in a one-dimensional granular medium.* Journal of Applied Mechanics and Technical Physics, 1985. **26**(3): p. 405-408.
37. Chatterjee, A., *Asymptotic solution for solitary waves in a chain of elastic spheres.* Physical Review E, 1999. **59**(5): p. 5912-5919.
38. Hinch, E.J. and S. Saint–Jean, *The fragmentation of a line of balls by an impact.* Proceedings of the Royal Society of London. Series A: Mathematical, Physical and Engineering Sciences, 1999. **455**(1989): p. 3201-3220.
39. Sun, D. and S. Sen, *Nonlinear grain–grain forces and the width of the solitary wave in granular chains: a numerical study.* Granular Matter, 2013. **15**(2): p. 157-161.
40. Coste, C., E. Falcon, and S. Fauve, *Solitary waves in a chain of beads under Hertz contact.* Physical Review E, 1997. **56**(5): p. 6104-6117.
41. Coste, C. and B. Gilles, *On the validity of Hertz contact law for granular material acoustics.* The European Physical Journal B - Condensed Matter and Complex Systems, 1999. **7**(1): p. 155-168.

42. Daraio, C., et al., *Tunability of solitary wave properties in one-dimensional strongly nonlinear phononic crystals.* Physical Review E, 2006. **73**(2): p. 026610.
43. Nesterenko, V.F., A.N. Lazaridi, and E.B. Sibiryakov, *The decay of soliton at the contact of two "acoustic vacuums".* Journal of Applied Mechanics and Technical Physics, 1995. **36**(2): p. 166-168.
44. MacKay, R.S., *Solitary waves in a chain of beads under Hertz contact.* Physics Letters A, 1999. **251**(3): p. 191-192.
45. Friesecke, G. and J.D. Wattis, *Existence theorem for solitary waves on lattices.* Communications in Mathematical Physics, 1994. **161**(2): p. 391-418.
46. Ji, J.-Y. and J. Hong, *Existence criterion of solitary waves in a chain of grains.* Physics Letters A, 1999. **260**(1–2): p. 60-61.
47. Shukla, A., et al., *Role of particle shape and contact profile on the dynamic response of particulate materials.* Optics and Lasers in Engineering, 1993. **19**(1–3): p. 99-119.
48. Ngo, D., D. Khatri, and C. Daraio, *Highly nonlinear solitary waves in chains of ellipsoidal particles.* Physical Review E, 2011. **84**(2): p. 026610.
49. Khatri, D., D. Ngo, and C. Daraio, *Highly nonlinear solitary waves in chains of cylindrical particles.* Granular Matter, 2012. **14**(1): p. 63-69.
50. Ngo, D., et al., *Highly nonlinear solitary waves in chains of hollow spherical particles.* Granular Matter, 2013. **15**(2): p. 149-155.
51. Porter, M.A., et al., *Highly nonlinear solitary waves in periodic dimer granular chains.* Physical Review E, 2008. **77**(1): p. 015601.
52. Porter, M.A., et al., *Highly nonlinear solitary waves in heterogeneous periodic granular media.* Physica D: Nonlinear Phenomena, 2009. **238**(6): p. 666-676.
53. Jayaprakash, K.R., Y. Starosvetsky, and A.F. Vakakis, *New family of solitary waves in granular dimer chains with no precompression.* Physical Review E, 2011. **83**(3): p. 036606.
54. Carretero-González, R., et al., *Dissipative Solitary Waves in Granular Crystals.* Physical Review Letters, 2009. **102**(2): p. 024102.
55. Daraio, C. and V.F. Nesterenko, *Strongly nonlinear wave dynamics in a chain of polymer coated beads.* Physical Review E, 2006. **73**(2): p. 026612.
56. Manciu, M., S. Sen, and A.J. Hurd, *Crossing of identical solitary waves in a chain of elastic beads.* Physical Review E, 2000. **63**(1): p. 016614.
57. Manciu, F.S. and S. Sen, *Secondary solitary wave formation in systems with generalized Hertz interactions.* Physical Review E, 2002. **66**(1): p. 016616.
58. Wen, Z.-Y., et al., *Solitary Wave Interactions in Granular Media.* Chinese Physics Letters, 2007. **24**(10): p. 2887.
59. Ávalos, E. and S. Sen, *How solitary waves collide in discrete granular alignments.* Physical Review E, 2009. **79**(4): p. 046607.
60. Santibanez, F., et al., *Experimental evidence of solitary wave interaction in Hertzian chains.* Physical Review E, 2011. **84**(2): p. 026604.
61. Job, S., et al., *How Hertzian Solitary Waves Interact with Boundaries in a 1D Granular Medium.* Physical Review Letters, 2005. **94**(17): p. 178002.
62. Singh, R., A. Shukla, and H. Zervas, *Explosively generated pulse propagation through particles containing natural cracks.* Mechanics of Materials, 1996. **23**(4): p. 255-270.
63. Job, S., et al., *Wave localization in strongly nonlinear Hertzian chains with mass defect.* Physical Review E, 2009. **80**(2): p. 025602.

64. Nesterenko, V.F., et al., *Anomalous Wave Reflection at the Interface of Two Strongly Nonlinear Granular Media.* Physical Review Letters, 2005. **95**(15): p. 158702.
65. Yang, J., et al., *Site-Specific Quantification of Bone Quality Using Highly Nonlinear Solitary Waves.* Journal of Biomechanical Engineering, 2012. **134**(10): p. 101001-101001.
66. Lydon, J., et al., *Frequency bands of strongly nonlinear homogeneous granular systems.* Physical Review E, 2013. **88**(1): p. 012206.
67. Herbold, E.B., et al., *Pulse propagation in a linear and nonlinear diatomic periodic chain: effects of acoustic frequency band-gap.* Acta Mechanica, 2009. **205**(1-4): p. 85-103.
68. Hladky-Hennion, A.-C. and M. de Billy, *Experimental validation of band gaps and localization in a one-dimensional diatomic phononic crystal.* The Journal of the Acoustical Society of America, 2007. **122**(5): p. 2594-2600.
69. Hladky-Hennion, A.-C., et al., *Sonic band gaps in one-dimensional phononic crystals with a symmetric stub.* Physical Review B, 2008. **77**(10): p. 104304.
70. Boechler, N. and C. Daraio. *An experimental investigation of acoustic band gaps and localization in granular elastic chains.* in *ASME 2009 International Design Engineering Technical Conferences and Computers and Information in Engineering Conference.* 2009. American Society of Mechanical Engineers.
71. Boechler, N., et al., *Tunable vibrational band gaps in one-dimensional diatomic granular crystals with three-particle unit cells.* Journal of Applied Physics, 2011. **109**(7): p. 074906.
72. Boechler, N., et al., *Discrete Breathers in One-Dimensional Diatomic Granular Crystals.* Physical Review Letters, 2010. **104**(24): p. 244302.
73. Theocharis, G., et al., *Localized breathing modes in granular crystals with defects.* Physical Review E, 2009. **80**(6): p. 066601.
74. Boechler, N., G. Theocharis, and C. Daraio, *Bifurcation-based acoustic switching and rectification.* Nat Mater, 2011. **10**(9): p. 665-668.
75. Daraio, C., et al., *Highly nonlinear pulse splitting and recombination in a two-dimensional granular network.* Physical Review E, 2010. **82**(3): p. 036603.
76. Ngo, D., F. Fraternali, and C. Daraio, *Highly nonlinear solitary wave propagation in Y-shaped granular crystals with variable branch angles.* Physical Review E, 2012. **85**(3): p. 036602.
77. Ngo, D., F. Fraternali, and C. Daraio. *Angular Dependence of Highly Nonlinear Pulse Splitting in a Two Dimensional Granular Network.* in *Proceedings of the ASME 2010 International Mechanical Engineering Congress & Exposition, IMECE2010-39699, Vancouver Canada.* 2010.
78. Leonard, A., L. Ponson, and C. Daraio, *Exponential stress mitigation in structured granular composites.* Extreme Mechanics Letters, 2014. **1**(0): p. 23-28.
79. Rossmanith, H.P. and A. Shukla, *Photoelastic investigation of dynamic load transfer in granular media.* Acta Mechanica, 1982. **42**(3-4): p. 211-225.
80. Shukla, A. and C. Damania, *Experimental investigation of wave velocity and dynamic contact stresses in an assembly of disks.* Experimental Mechanics, 1987. **27**(3): p. 268-281.
81. Shukla, A., *Dynamic photoelastic studies of wave propagation in granular media.* Optics and Lasers in Engineering, 1991. **14**(3): p. 165-184.
82. Sadd, M.H., Q. Tai, and A. Shukla, *Contact law effects on wave propagation in particulate materials using distinct element modeling.* International Journal of Non-Linear Mechanics, 1993. **28**(2): p. 251-265.
83. Zhu, Y., A. Shukla, and M.H. Sadd, *The effect of microstructural fabric on dynamic load transfer in two dimensional assemblies of elliptical particles.* Journal of the Mechanics and Physics of Solids, 1996. **44**(8): p. 1283-1303.

84. Singh, R., A. Shukla, and H. Zervas, *Effect of flaws on the stress wave propagation in particulate aggregates: Near and far field observations.* International Journal of Solids and Structures, 1995. **32**(17–18): p. 2523-2546.
85. Leonard, A., F. Fraternali, and C. Daraio, *Directional wave propagation in a highly nonlinear square packing of spheres.* Experimental Mechanics, 2013. **53**(3): p. 327-337.
86. Szelengowicz, I., P.G. Kevrekidis, and C. Daraio, *Wave propagation in square granular crystals with spherical interstitial intruders.* Physical Review E, 2012. **86**(6): p. 061306.
87. Goddard, J., *Nonlinear elasticity and pressure-dependent wave speeds in granular media.* Proceedings of the Royal Society of London. Series A: Mathematical and Physical Sciences, 1990. **430**(1878): p. 105-131.
88. Vergara, L., *Scattering of solitary waves from interfaces in granular media.* Physical review letters, 2005. **95**(10): p. 108002.
89. Mueggenburg, N.W., H.M. Jaeger, and S.R. Nagel, *Stress transmission through three-dimensional ordered granular arrays.* Physical Review E, 2002. **66**(3): p. 031304.
90. Ponson, L., et al., *Nonlinear waves in disordered diatomic granular chains.* Physical Review E, 2010. **82**(2): p. 021301.
91. Geng, J., et al., *Footprints in Sand: The Response of a Granular Material to Local Perturbations.* Physical Review Letters, 2001. **87**(3): p. 035506.
92. Breton, L., et al., *Stress response function of a two-dimensional ordered packing of frictional beads.* EPL (Europhysics Letters), 2002. **60**(6): p. 813.
93. Geng, J., et al., *Green's function measurements of force transmission in 2D granular materials.* Physica D: Nonlinear Phenomena, 2003. **182**(3): p. 274-303.
94. Manjunath, M., A.P. Awasthi, and P.H. Geubelle, *Wave propagation in random granular chains.* Physical Review E, 2012. **85**(3): p. 031308.
95. Gilles, B. and C. Coste, *Low-frequency behavior of beads constrained on a lattice.* Physical review letters, 2003. **90**(17): p. 174302.
96. Anfosso, J. and V. Gibiat, *Elastic wave propagation in a three-dimensional periodic granular medium.* EPL (Europhysics Letters), 2004. **67**(3): p. 376.
97. Coste, C. and B. Gilles, *Sound propagation in a constrained lattice of beads: High-frequency behavior and dispersion relation.* Physical Review E, 2008. **77**(2): p. 021302.
98. Mouraille, O. and S. Luding, *Sound wave propagation in weakly polydisperse granular materials.* Ultrasonics, 2008. **48**(6): p. 498-505.
99. Sen, S. and R.S. Sinkovits, *Sound propagation in impure granular columns.* Physical Review E, 1996. **54**(6): p. 6857.
100. Nishida, M., K. Tanaka, and T. Ishida, *DEM simulation of wave propagation in two-dimensional ordered array of particles*, in *Shock Waves*. 2009, Springer. p. 815-820.
101. Nishida, M. and Y. Tanaka, *DEM simulations and experiments for projectile impacting two-dimensional particle packings including dissimilar material layers.* Granular Matter, 2010. **12**(4): p. 357-368.
102. Hascoët, E. and H.J. Herrmann, *Shocks in non-loaded bead chains with impurities.* The European Physical Journal B-Condensed Matter and Complex Systems, 2000. **14**(1): p. 183-190.
103. Maugis, D., *Adhesion of spheres: The JKR-DMT transition using a dugdale model.* Journal of Colloid and Interface Science, 1992. **150**(1): p. 243-269.

104. Johnson, K.L., K. Kendall, and A.D. Roberts, *Surface Energy and the Contact of Elastic Solids*. Proceedings of the Royal Society of London. A. Mathematical and Physical Sciences, 1971. **324**(1558): p. 301-313.
105. Derjaguin, B.V., V.M. Muller, and Y.P. Toporov, *Effect of contact deformations on the adhesion of particles*. Journal of Colloid and Interface Science, 1975. **53**(2): p. 314-326.
106. Peri, M.D.M. and C. Cetinkaya *, *Rolling resistance moment of microspheres on surfaces*. Philosophical Magazine, 2005. **85**(13): p. 1347-1357.
107. Cundall, P.A. *A computer model for simulating progressive large scale movements in blocky rock systems*. in *Proc. Symp. Rock Fracture (ISRM), Nancy*. 2013.
108. Cundall, P.A. and O.D. Strack, *A discrete numerical model for granular assemblies*. Geotechnique, 1979. **29**(1): p. 47-65.
109. Radjai, F., S. Roux, and J.J. Moreau, *Contact forces in a granular packing*. Chaos: An Interdisciplinary Journal of Nonlinear Science, 1999. **9**(3): p. 544-550.
110. Goldenberg, C. and I. Goldhirsch, *Force Chains, Microelasticity, and Macroelasticity*. Physical Review Letters, 2002. **89**(8): p. 084302.
111. *Rolling Resistance at Contacts in Simulation of Shear Band Development by DEM*. Journal of Engineering Mechanics, 1998. **124**(3): p. 285-292.
112. Hurd, A.J., et al., *Lattice dynamics of colloidal crystals*. Physical Review A, 1982. **26**(5): p. 2869.
113. Cheng, Z., et al., *Phonons in an entropic crystal*. Physical review letters, 2000. **85**(7): p. 1460.
114. Hoppenbrouwers, M. and W. van de Water, *Modes of motion of a colloidal crystal*. Physical review letters, 1998. **80**(17): p. 3871.
115. Chen, K., et al., *Phonons in two-dimensional soft colloidal crystals*. Physical Review E, 2013. **88**(2): p. 022315.
116. Keim, P., et al., *Harmonic lattice behavior of two-dimensional colloidal crystals*. Physical review letters, 2004. **92**(21): p. 215504.
117. Polin, M., D.G. Grier, and S.R. Quake, *Anomalous vibrational dispersion in holographically trapped colloidal arrays*. Physical review letters, 2006. **96**(8): p. 088101.
118. Baumgartl, J., M. Zvyagolskaya, and C. Bechinger, *Tailoring of phononic band structures in colloidal crystals*. Physical review letters, 2007. **99**(20): p. 205503.
119. Pertsinidis, A. and X.S. Ling, *Statics and dynamics of 2D colloidal crystals in a random pinning potential*. Physical review letters, 2008. **100**(2): p. 028303.
120. Baumgartl, J., et al., *Phonon dispersion curves of two-dimensional colloidal crystals: the wavelength-dependence of friction*. Soft Matter, 2008. **4**(11): p. 2199-2206.
121. von Grünberg, H. and J. Baumgartl, *Lattice dynamics of two-dimensional colloidal crystals subject to external light potentials*. Physical Review E, 2007. **75**(5): p. 051406.
122. Russel, W.B., D.A. Saville, and W.R. Schowalter, *Colloidal Dispersions*. 1992: Cambridge University Press.
123. Brady, J.F., et al., *Dynamic simulation of hydrodynamically interacting suspensions*. Journal of Fluid Mechanics, 1988. **195**: p. 257-280.
124. Foss, D.R. and J.F. Brady, *Structure, diffusion and rheology of Brownian suspensions by Stokesian dynamics simulation*. Journal of Fluid Mechanics, 2000. **407**: p. 167-200.
125. Job, S., et al., *Solitary wave trains in granular chains: experiments, theory and simulations*. Granular Matter, 2007. **10**(1): p. 13-20.
126. Leonard, A. and C. Daraio, *Stress Wave Anisotropy in Centered Square Highly Nonlinear Granular Systems*. Physical Review Letters, 2012. **108**(21): p. 214301.

127. Lydon, J., G. Theocharis, and C. Daraio, *Nonlinear resonances and energy transfer in finite granular chains*. Physical Review E, 2015. **91**(2): p. 023208.
128. Leonard, A., et al., *Effects of weak disorder on stress-wave anisotropy in centered square nonlinear granular crystals*. Physical Review E, 2012. **86**(3): p. 031305.
129. Davis, J.R. and A.S.M.I.H. Committee, *Stainless Steels*. 1994: ASM International.
130. 2015; Available from: www.nemb.com.
131. Sato, K., et al., *Roughening of single-crystal silicon surface etched by KOH water solution*. Sensors and Actuators A: Physical, 1999. **73**(1–2): p. 122-130.
132. Yang, J., et al., *Interaction of highly nonlinear solitary waves with linear elastic media*. Physical Review E, 2011. **83**(4): p. 046606.
133. Ni, X., P. Rizzo, and C. Daraio, *Actuators for the generation of highly nonlinear solitary waves*. Review of Scientific Instruments, 2011. **82**(3): p. 034902.
134. Bäuerle, D., *Laser Processing and Chemistry*. 2011: Springer.
135. Ni, X., P. Rizzo, and C. Daraio, *Laser-based excitation of nonlinear solitary waves in a chain of particles*. Physical Review E, 2011. **84**(2): p. 026601.
136. Chichkov, B.N., et al., *Femtosecond, picosecond and nanosecond laser ablation of solids*. Applied Physics A, 1996. **63**(2): p. 109-115.
137. Fogarassy, E. and D. Geohegan, *Laser Ablation*. 2012: Elsevier Science.
138. DuPont, A., et al., *Enhancement of material ablation using 248, 308, 532, 1064 nm laser pulse with a water film on the treated surface*. Journal of Applied Physics, 1995. **78**(3): p. 2022-2028.
139. Cheng, N.-S., *Formula for the Viscosity of a Glycerol−Water Mixture*. Industrial & Engineering Chemistry Research, 2008. **47**(9): p. 3285-3288.
140. Association, G.P., *Physical Properties of Glycerine and Its Solutions*. 1963: Glycerine Producers' Association.
141. Ashkin, A. and J. Dziedzic, *Optical trapping and manipulation of viruses and bacteria*. Science, 1987. **235**(4795): p. 1517-1520.
142. Grier, D.G., *Optical tweezers in colloid and interface science*. Current opinion in colloid & interface science, 1997. **2**(3): p. 264-270.
143. Bachman, R.A., *Sphere rolling down a grooved track*. American Journal of Physics, 1985. **53**(8): p. 765-767.
144. Halsey, T.C. and D. Ertaş, *A Ball in a Groove*. Physical Review Letters, 1999. **83**(24): p. 5007-5010.
145. Tabor, D., *The Mechanism of Rolling Friction. II. The Elastic Range*. Proceedings of the Royal Society of London. Series A. Mathematical and Physical Sciences, 1955. **229**(1177): p. 198-220.
146. Israelachvili, J.N., *Intermolecular and Surface Forces: Revised Third Edition*. 2011: Elsevier Science.
147. Becker, V., T. Schwager, and T. Pöschel, *Coefficient of tangential restitution for the linear dashpot model*. Physical Review E, 2008. **77**(1): p. 011304.
148. Leonard, A., et al., *Traveling waves in 2D hexagonal granular crystal lattices*. Granular Matter, 2014. **16**(4): p. 531-542.
149. Fernandez, N., et al., *Microscopic mechanism for shear thickening of non-Brownian suspensions*. Physical review letters, 2013. **111**(10): p. 108301.
150. Johnson, K.L. and K.L. Johnson, *Contact Mechanics*. 1987: Cambridge University Press.
151. Davis, R.H., J.-M. Serayssol, and E. Hinch, *The elastohydrodynamic collision of two spheres*. Journal of Fluid Mechanics, 1986. **163**: p. 479-497.

152. Lian, G., M. Adams, and C. Thornton, *Elastohydrodynamic collisions of solid spheres*. Journal of Fluid Mechanics, 1996. **311**: p. 141-152.
153. Xue, W. and G.S. Grest, *Brownian dynamics simulations for interacting colloids in the presence of a shear flow*. Physical Review A, 1989. **40**(3): p. 1709-1712.
154. Marshall, J.S., *Viscous damping force during head-on collision of two spherical particles*. Physics of Fluids, 2011. **23**(1): p. 013305.